IMT School for Advanced Studies, Lucca

Lucca, Italy

Cancer tissue classification from DCE-MRI data using pattern recognition techniques

PhD Program in Image Analysis

XXX Cycle

By

Maria Venianaki

2018

The dissertation of Maria Venianaki is currently under approval by:

Program Coordinator: Prof. Rocco de Nicola, IMT School for Advanced Studies Lucca

Supervisor: Prof. Rocco De Nicola, IMT School for Advanced Studies Lucca

Supervisor: Dr. Ovidio Salvetti, National Research Council of Italy

Supervisor: Prof. Kostas Marias, Technological Educational Institute of Crete & Foundation for Research and Technology – Hellas

The dissertation of Maria Venianaki is under review by:

Nikolaos Papanikolaou, Champalimaud Foundation

Prof. Leontios Hadjileontiadis, Aristotle University of Thessaloniki & Khalifa University

IMT School for Advanced Studies, Lucca

2018

Contents

List of Figures

List of Tables

Acknowledgements

This thesis would not have been possible without the support and guidance of a number of wonderful people. I am using this opportunity to express my gratitude to everyone who supported me throughout the course of this thesis.

Firstly, I would like to express my sincere gratitude to my advisor, Prof. De Nicola for trusting and supporting me during all these years and for giving me the opportunity to participate in many conferences and meeting other researchers. I owe my deepest gratefulness to my co-advisor Dr. Ovidio Salvetti for his continuous support during the PhD, for his encouragement, for his valuable suggestions and advice. I would also like to profoundly thank my co-advisor Prof. Kostas Marias for hosting me as a visiting researcher at the Computational BioMedicine laboratory at ICS/FORTH and for giving me the opportunity to work in such an inspiring and multidisciplinary environment and to collaborate with many great researchers and clinicians. His patience, motivation, support and scientific advice helped me during the course of all my research period in Greece as well as the writing of this thesis.

I owe a debt of gratitude to the following staff of the University General Hospital of Heraklion: Prof. Apostolos Karantanas, Prof. Thomas Maris, Prof. Eelco de Bree and Dr. Eleni Lagoudaki. I am deeply grateful to each one of them for their support, guidance, clinical insights and most importantly for making it possible to carry out this work by giving me their approval to use MR imaging and histopathology data of the University General Hospital of Heraklion. This thesis would

not have been possible without their continuous support and assistance.

I am also greatly thankful to the reviewers: Nikolaos Papanikolaou and Prof. Leontios Hadjileontiadis for their valuable comments and suggestions. I really appreciate the time they spent for reading my thesis and for their great suggestions that helped improving it.

I am also very thankful to my colleagues of the CBML group at FORTH for the fruitful discussions, suggestions, support and for all the funny moments spent together. Special thanks go to Lefteris for the great help and guidance since the beginning of my visiting period at FORTH and to Katerina for the collaboration and suggestions during the last year of my PhD.

I would like to thank all my friends for their encouragement, support and understanding. Thank you Eleni and Emmanouela for always being there in the happy and the difficult moments even though being far away. Thank you Giorgos, Natasa, Mary, Haris, Katerina and Anna for all the nice moments we have spent together and for your patience and understanding when times were difficult! I am also very grateful to my cousin, Manolis who has helped me a lot when moving to Heraklion and has been a great friend whenever I needed him.

Last but not least, I would like to dedicate this work to my family for their love and encouragement. To my mother, who has always been a great example of inspiration, trust and strength and has supported me during all my achievements, including this work. To my father, for his support and his guidance in critical decisions. And of course to my sister, Eva who has always been of great support and motivation to me and has helped me many times with her beautiful and strong character and her wise advice.

Most of the material in this thesis has been published. In particular: part of Chapter 3 and part of Chapter 4 are based on (VKN$^+$16; VSdB$^+$18) coauthored with Kontopodis E., Nikiforaki K., de Bree E., Maris T., Karantanas A., Salvetti O. and Marias K. The second case study from Chapter 4 was adapted based on (VKdB$^+$18), coauthored with the same authors as in (VKN$^+$16; VSdB$^+$18) while the third case study from Chapter 4 was adapted based on (NMV$^+$18) coauthored with Nikiforaki K., Manikis G., Kontopodis E., Lagoudaki E., Maris T., Marias K., de Bree E. and Karantanas A. Finally, one adapted case study (Case study V) from Chapter 4 is based on (KVM$^+$on), coauthored with Kontopodis E., Manikis G., Nikiforaki K., Salvetii O., Papadaki E., Papadakis G., Karantanas A. and Marias K.

Vita

Mach 22, 1986	Born, Chania, Greece
2003-2009	MEng Electrical & Computer Engineering Faculty of Engineering Aristotle University of Thessaloniki, Greece
2009-2010	MSc Biomedical Engineering Imperial College London, United Kingdom
2011-2012	International e-health tenders and R&D projects Tesan Spa, Vicenza, Italy
2012-2014	Telecare & Telemedicine Business Development and R&D TBS Group, Trieste, Italy
2014-2018	Ph.D in Image Analysis IMT School for Advanced studies Lucca, Italy
2016-2018	Visiting Research Student Computational BioMedicine Laboratory Institute of Computer Science Foundation for Research and Technology – Hellas Heraklion, Greece

Publications

1. M. Venianaki, E. Kontopodis, K. Nikiforaki, E. de Bree, O. Salvetti, K. Marias, "A model-free approach for imaging tumor hypoxia from DCE-MRI data," in *CGI'16 - 33rd Computer Graphics International*, pp. 105-108, 2016.
2. **M. Venianaki***, E. Kontopodis*, K. Nikiforaki, E. de Bree, T. Maris, A. Karantanas, O. Salvetti, K. Marias, "Improving hypoxia map estimation by using model-free classification techniques in DCE-MRI images," *2016 IEEE International Conference on Imaging Systems and Techniques (IST)*, pp. 183-188, 2016.
3. **M. Venianaki**, O. Salvetti, E. de Bree, T. Maris, A. Karantanas, E. Kontopodis, K. Nikiforaki, K. Marias, "Pattern recognition and pharmacokinetic methods on DCE-MRI data for tumor hypoxia mapping in sarcoma," *Multimedia Tools and Applications*, vol. 77, no. 8, pp. 9417-9439, 2018.
4. **M. Venianaki**, A. Karantanas, E. de Bree, T. Maris, E. Kontopodis, K. Nikiforaki, O. Salvetti, K. Marias, "Assessment of soft-tissue sarcomas perfusion using data-driven techniques," *2018 IEEE EMBS International Conference on Biomedical & Health Informatics (BHI)*, pp. 353-356, 2018.
5. E. Kontopodis, G. C. Manikis, K. Nikiforaki, **M. Venianaki**, K. Marias, T. Maris, A. Karantanas, E. Papadaki, "Incremental diagnostic information obtained via novel Dynamic Contrast Enhanced (DCE) Magnetic Resonance Imaging (MRI) framework applied on Multiple Sclerosis (MS) patients," *2018 IEEE EMBS International Conference on Biomedical & Health Informatics (BHI)*, pp. 46-49, 2018.
6. K. Nikiforaki, G. C. Manikis, **M. Venianaki**, E. Kontopodis, E. Lagoudaki, T. Maris, K. Marias, E. de Bree, A. Karantanas, "Perfusion and Oxygenation Changes after Isolated Limb Perfusion with TNF - α in Lower Limb Sarcoma: A Case Report," *Biomedical Research and Reviews*, vol. 1, no. 1, p. 101, 2018.
7. K. Nikiforaki, G. C. Manikis, **M. Venianaki**, E. Kontopodis, E. Lagoudaki, E. de Bree, T. Maris, K. Marias, A. Karantanas, "[OA022] T2 and T* relaxometry of benign and malignant lipomatous tumors," *Physica Medica: European Journal of Medical Physics*, vol. 52, no. 1, pp. 9-10, 2018.
8. E. Kontopodis*, **M. Venianaki***, G. C. Manikis, K. Nikiforaki, O. Salvetti, E. Papadaki, G. Z. Papadakis, A. Karantanas, K. Marias, "Investigating the role of model-based and model-free imaging biomarkers as early predictors of neoadjuvant breast cancer therapy outcome," *IEEE Journal of Biomedical and Health Informatics*, submitted for publication.

Presentations

1. M. Venianaki, "A model-free approach for imaging tumor hypoxia from DCE-MRI data," at *CGI'16 - 33rd Computer Graphics International*, Heraklion, Greece, 2016.
2. M. Venianaki, "Improving hypoxia map estimation by using model-free classification techniques in DCE-MRI images," at *2016 IEEE International Conference on Imaging Systems and Techniques (IST)*, Chania, Greece, 2016.
3. M. Venianaki, "Assessment of soft-tissue sarcomas perfusion using data-driven techniques," at *2018 IEEE EMBS International Conference on Biomedical & Health Informatics (BHI)*, Las Vegas, NV, USA, 2018.
4. M. Venianaki, "Incremental diagnostic information obtained via novel Dynamic Contrast Enhanced (DCE) Magnetic Resonance Imaging (MRI) framework applied on Multiple Sclerosis (MS) patients," at *2018 IEEE EMBS International Conference on Biomedical & Health Informatics (BHI)*, Las Vegas, NV, USA, 2018.

Abstract

Cancer research has significantly advanced in recent years mainly through developments in medical genomics and bioinformatics. It is expected that such approaches will result in more durable tumor control and fewer side effects compared with conventional treatments such as radiotherapy or chemotherapy. From the imaging standpoint, non-invasive imaging biomarkers (IBs) that assess angiogenic response and tumor environment at an early stage of therapy are of utmost importance since they could provide useful insights into therapy planning. However, the extraction of IBs is still an open problem since there are no standardized imaging protocols yet or established methods for the robust extraction of IBs. DCE-MRI is amongst the most promising non-invasive functional imaging modalities while compartmental pharmacokinetic (PK) modeling is the most common technique used for DCE-MRI data analysis. However, PK models suffer from a number of limitations such as modeling complexity, which often leads to variability in the computed biomarkers. To address these problems, alternative DCE-MRI biomarker extraction strategies coupled with a profound understanding of the physiological meaning of IBs is a sine qua non condition. To this end, a more recent model-free approach has been suggested in literature for the analysis of DCE-MRI data, which relies on the shape classification of the time-signal uptake curves of image pixels in a selected tumor region of interest. This thesis is centered on this new approach and the clinical question whether model-free DCE-MRI data analysis has the potential to provide robust, clinically significant biomarkers using pattern recognition and image analysis techniques.

Chapter 1

Introduction

Imaging cancer physiology is a great challenge since cancer exhibits a very heterogeneous behavior depending on the organ, the person, the grade. Malignant cells are biologically and morphologically different even within the same tumor. This thesis investigates the link between tumor pathophysiology and significant physiological imaging characteristics acquired from dynamic contrast-enhanced magnetic resonance imaging (DCE-MRI).

There is a large number of candidate MR imaging biomarkers (IBs) that we are able to measure today, yet we still need to prove the exact correlation of these biomarkers with the underlying tumor biology before they can be used in the clinical setting. There are also diverse ways of obtaining MR measurements in many different organs of the body using advanced MR imaging techniques, such as Diffusion-weighted magnetic resonance imaging (DWI or DW-MRI) and DCE-MRI, as well as innovative multiparametric protocols which improve the MR imaging overall diagnostic accuracy. As cancer research progresses, new biomarkers are discovered and we have better understanding of how to measure them properly. However, we need to gain further insight into the meaning of these MR biomarkers and find out how they relate to the biological changes that take place in cancer disease. To understand the biological meaning and significance of MR IBs is of great importance; it forms a

novel study area, which goes beyond data acquisition skills and image analysis skills requiring close collaboration by skilled biologists, radiologists, engineers and histologists. In the recently published IB roadmap (OAA$^+$17), there are key recommendations for the clinical translation of cancer IBs aiming to accelerate their use as decision-making tools. This review emphasizes the complex procedures and the various prerequisites required for IBs so that their clinical validity is accepted and they can ultimately be integrated into routine patient management.

To this end, in this thesis sophisticated pattern recognition techniques were employed for the extraction of meaningful pathophysiological biomarkers from DCE-MRI data. In particular, tumor tissue was classified into physiologically meaningful regions with high, medium and low perfusion, i.e. well-perfused, hypoxic and necrotic regions respectively. The primary goal of this work is the development of an image analysis algorithm for the automatic recognition of certain enhancement patterns that are associated with specific tumor physiology characteristics such as hypoxia. The importance of uncovering the specific features of tumor environment as well as the potential of segmenting tumor areas directly from DCE-MRI imaging data are discussed in the following sections.

1.1 Motivation

This section includes the main motivation behind this thesis. Firstly, we discuss the complex nature of the tumor environment focusing particularly on hypoxia, which is a major cancer hallmark. Subsequently, we explore the role of imaging techniques as an approach of describing the specific tumor characteristics.

1.1.1 Importance of understanding tumor environment in oncology

Tumors are biologically and morphologically heterogeneous, similarly to organs, exhibiting considerable variation in vasculature and function (CJ00). They have unique physiology making drug delivery very chal-

lenging in some cases. In particular, the vascular microenvironment is one of the major determinants of the tumor's pathophysiological state. In this thesis, we sought to identify certain features of the tumor vasculature, such as hypoxia, which play a key role in the tumor's response to therapy.

Hypoxia is a pathological condition emanating from poor oxygen to tissue and it was first evidenced in 1955 in a lung tumor study that it could be associated with negative impact on the effectiveness of radiotherapy (TG55). Hypoxia is present in most malignant solid tumors yet it is hard to define the hypoxic condition of a tumor only through its anatomy since hypoxia exhibits a heterogeneous profile and is not dependent on the size, stage or type of a tumor. Tumors are associated with abnormal rapid formation of new blood vessels, in an aim to overcome the increased oxygen and other nutrient demands during tumor growth. However, tumor newly-formed vessels are typically dysfunctional impeding proper vessel-to-tissue delivery of both oxygen and chemotherapy drugs. Eventually, the augmented interstitial fluid pressure is followed by a subsequent decrease of tumor perfusion, further favoring tumor hypoxia (FJ07). Hypoxia-inducible factor 1-alpha (HIF-1α) is an oxygen-regulated transcription factor, which is the major transcriptional regulator of hypoxia. Its overexpression has been associated with reduced survival rates in colorectal cancer (BNS$^+$10) and it has also been linked to poor prognosis in breast, head and neck, cervix and brain tumors (BSO$^+$00; KGS$^+$02; SSS$^+$02; ZZS$^+$00). HIF-1α induces the transcription of the vascular endothelial growth factor (VEGF) among other genes. VEGF holds an important role in angiogenesis and it is usually overexpressed in human tumors.

As shown in Figure 1, three different areas of interest are usually identified in the tumor (JMG$^+$14); the necrotic core, the hypoxic penumbra and the active tumor, sometimes called normoxia. This might be an ideal shape for the approximation of tumor areas however, it generally applies that tumor grows from the core towards the outside of the tissue. It has been reported in several studies that hypoxia is linked with more disease aggressiveness, recurrence and resistance to chemotherapy and radio-

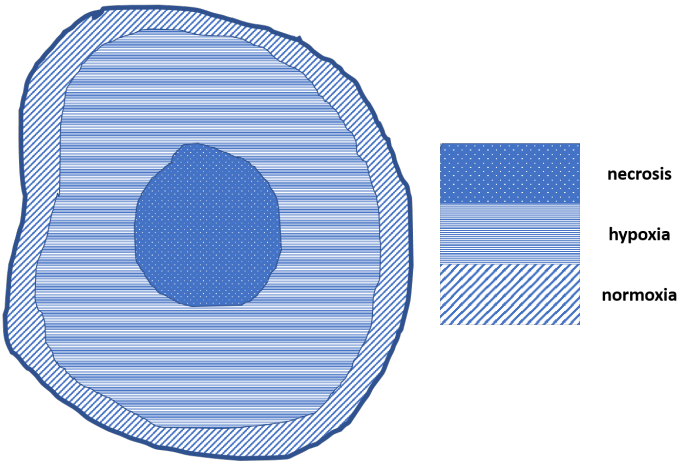

Figure 1: An illustration of the three distinct tumor areas that are commonly present in tumors: in the center there is the necrotic core which is surrounded by the hypoxic penumbra and finally the active tumor, called normoxia.

therapy (DFHM15; HSM$^+$96; MF05). What is more, hypoxia has been proven to be a strong prognostic indicator for poor patient outcome. In particular, hypoxia has been associated with low overall survival and disease-free survival rates in a large study of head and neck cancer patients (NBR$^+$05).

In light of the above, defining the presence as well as the extent of hypoxia in a tumor is of utmost importance since it can play a key role in tumor characterization and lead to more accurate and effective treatment strategies which will eventually improve patient outcomes. Among the different approaches used to identify hypoxia, the polarographic electrodes have been traditionally used especially in older studies for assessing the oxygenation status of solid tumors (VHM07). However, this invasive method is not suitable for large clinical trials thus new imaging techniques and computational methods have been developed in order to extract information about hypoxia and assess non-invasively its prognostic ability.

1.1.2 Role of imaging

Imaging technologies are the backbone of oncology and are an essential tool for locating, measuring, monitoring and staging tumors. The ability to image the tumor heterogeneity can provide useful prognostic and diagnostic information including a variety of factors that influence tumor growth and response to treatment.

The direct measurement of tumor physiological properties usually involves invasive procedures such as the use of polarographic electrodes for the direct measurement of tissue oxygen concentration. More specifically, for the assessment of tumor hypoxia several techniques have been used (WLA+14), including pO2 electrode measurements and immunohistochemistry of exogenous markers e.g. pimonidazole (PIMO). However, they are both invasive and of limited ability to globally assess hypoxia since they target restricted areas of the tumor. On the contrary, non-invasive imaging offers several advantages, including high resolution, repeatability of measurements on the same subject, assessment of difficult to reach tumors, and potential application to image-guided therapy.

Most of the major imaging modalities have been used in the investigation of tumor microvasculature, including MRI, positron emission tomography (PET), ultrasound, computed tomography (CT), as well as single photon emission computed tomography (SPECT). MRI provides exceptional functional and structural information on tumor vasculature and physiology at high spatial resolution. PET on the other hand can measure sensitively and quantitatively local concentrations of radioactive molecular targets of interest, such as 18F-fluoromisonidazole (18F-Fmiso). 18F-Fmiso PET is currently investigated at a great extent as a method of imaging tumor oxygenation (KRE+92; LS07). However, its spatial resolution is coarse while it is also a more expensive technique compared to MRI. DCE-CT is a contrast enhanced imaging technique, which can estimate blood volume and blood flow in tumors. Previous studies (LMS+05; MLJ+08) have shown correlation between CT perfusion findings and tumor angiogenesis and microvessel density. CT per-

fusion is not so widespread though, as it is associated with high radiation exposure. Contrast-enhanced ultrasound has the ability to depict vessels and assess tumor angiogenesis (BOM$^+$09; KCG$^+$07) yet it has certain limitations such as low spatial resolution and restricted field of view. In some cases, multi-modality imaging has been used such as PET/MRI (CAC$^+$09) and PET/CT (MSB$^+$11).

In our work, we focus on MRI techniques since they are widely used in hospitals and can provide both structural and functional information regarding tumor physiology at fine spatial resolution. MRI methods, including DCE-MRI (KMK$^+$99; Tof97), blood-oxygen-level dependent (BOLD) MRI (OLKT90) and magnetic resonance spectroscopy (MRS) (PCB$^+$07), are some examples of the different techniques used providing high-spatial resolution functional information.

In particular, DCE-MRI is the technique we will be concerned with in our research. This non-invasive imaging technique offers high spatial resolution, can be performed on clinical MRI scanners with standard specifications and can yield information concerning tissue oxygenation and vascularization. Its basic principle is that a paramagnetic contrast agent (CA) is injected into the tissue and changes the MR signal intensity depending on the local tissue concentration. When tumors grow, their vascular network is growing as well in order to support the tissue's increased needs for nutrients and oxygen. However, the vascular network created during tumor growth is quite abnormal and heterogeneous compared to the vascular network of normal tissue. Therefore, the DCE-MRI technique with its contrast enhancement ability is appropriate for high resolution measurements of the perfusion heterogeneity in tumors.

1.2 DCE-MRI correlation with tumor heterogeneity and hypoxia

DCE-MRI is a perfusion imaging technique that has the advantage to provide both anatomical and functional information. There have been various encouraging theoretical and experimental findings in many different clinical applications suggesting that DCE-MRI can play an impor-

tant clinical role in the early detection of diseases in different organs, such as breast, brain and prostate cancer, multiple sclerosis, rheumatoid arthritis and liver tumors (KKM+15; OS01; BEJ+99; HTG+94).

DCE-MRI is of great interest to oncologists and has an increasing number of clinical post-processing applications, which have given promising results not only in cancer diagnosis but also in the staging of tumor, in assessing treatment response (choice of therapy and therapy monitoring) as well as in describing tumor heterogeneity (OS01; OJP+12; PGM+00). An interesting study (MdAGB+15) has shown that DCE-MRI was capable of classifying BI-RADS category 4 breast lesions similarly to mammography and ultrasound. Furthermore, the technique has shown promising results in predicting response to therapy and differentiating between benign and malignant lesions (FJM+16; SAM+16).

Regarding hypoxia, DCE-MRI in combination with powerful computational analysis techniques seems to be an attractive choice for evaluating hypoxia without using radioactive tracers such as in the case of PET. In previous studies, DCE-MRI has been directly correlated with tumor oxygenation measured by polarographic electrodes (CCL+00) while its ability to quantify tumor vessel leakage renders it the modality of choice for quantifying tumor environment in well-perfused, hypoxic or necrotic image areas through pattern recognition techniques (CAT+17).

DCE-MRI has also been associated with histopathology in previous studies for the detection of hypoxia or for treatment prediction. In (SMG+17), histopathological parameters (tumor proliferation index and microvessel density parameters) from patients with head and neck squamous cell carcinoma (HNSCC) have been correlated with DCE pharmacokinetic (PK) parameters (k_{ep}, k^{trans}, v_e). In (KWS+99), the DCE parameter k_{ep} was proven to be closely correlated with VEGF expression in breast tumors. Correlations have been also found between DCE-MRI parameters and PIMO and CA9 staining in head and neck cancer patients (NCCE+09), suggesting that DCE parameters could potentially be used as reliable estimators of tumor hypoxia. In (ZLG+15), important correlations were also found between semi-quantitative DCE-MRI parameters and histopathological parameters, such as hematoxylin and eosin

(H&E), PIMO and VEGF in a maxillofacial VX2 rabbit model. In light of the above, DCE-MRI parameters are an attractive choice to be used as surrogate hypoxia markers.

In (LWS$^+$15), DCE-MRI data from 124 breast cancer patients were obtained and pharmacokinetic parameters were evaluated against histological parameters in order to assess if they can be useful in prediction of patient prognosis. It was shown that there was a positive correlation between the mean k^{trans} or k_{ep} values and the CD105 expression level. On the other hand, there was no correlation of the pharmacokinetic parameters with CD31, indicating that CD105 in combination with k^{trans} and/or k_{ep} might be a better marker for breast cancer diagnosis.

In this thesis, we first investigate the principles of DCE-MRI and the various related data-analysis approaches. Although several DCE-MRI analysis methods have already been clinically applied, a number of issues concerning the imaging protocols and the analytical methods hampers their optimized utilization and standardization. Quantitative analysis through pharmacokinetic modeling, empirical parametric models and model-free analysis based on DCE time-intensity curve analysis are the three main methods that are considered in this thesis. The focus is on the latter one since it uses fewer assumptions and can be combined with pattern recognition techniques in order to reveal IBs about tumor physiology such as its vasculature, oxygenation or heterogeneity. Specifically, a block update non-negative matrix factorization (BU-NMF) algorithm was used on DCE-MRI data from sarcoma and breast cancer patients.

Similar PR techniques have also been used in previous studies (HAS$^+$13; SHS$^+$12) on prostate cancer data for the clustering of tumor area in regions with different perfusion trends (well-perfused, hypoxic, and necrotic). In these studies, PR results were validated against PET and ex vivo immunohistochemistry (PIMO) findings for hypoxic areas, against H&E findings for necrotic areas and against a pharmacokinetic model for well-perfused areas in a limited number of pre-clinical studies. In (SHS$^+$12) NMF has been applied for the segmentation of rat prostate cancer DCE data. However, in our work we used an improved BU-NMF algorithm with a robust initialization method. This is discussed in detail

in Section 3.1. What is more important, herein the algorithm was used on human patient data whereas previous works (HAS+13; SHS+12) were performed on pre-clinical studies with limited number of data.

1.3 Problem statement

As discussed in the previous section, computational, PR techniques for understanding DCE-MRI tissue pathophysiology based on extracted IBs are of utmost clinical importance. The main reasons lie in the non-invasive nature of DCE-MRI as well as its wide clinical use in several applications in oncology.

This thesis aims to contribute with novel work in defining image-based quantitative measures able to discriminate/segment the main tumor-environment image components namely well-perfused, hypoxic and necrotic areas. It is important to clarify that the main intended contribution is focused on correlating the automatically segmented image areas with the actual tumor microenvironment and in particular hypoxia, which plays a critical role in predicting therapy outcome as early as possible.

To achieve these goals, in this thesis we use pattern recognition (PR) for the quantitative pathophysiological analysis of DCE-MRI data. Specifically, the focus is on the automatic analysis of time intensity curves in order to extract underlying patterns, which can potentially be associated to tumor physiological properties such as vasculature, oxygenation and permeability. In particular, our efforts aimed at:

1. Building of a suitable system for the analysis of time intensity curves: after having selected a suitable PR method, the BU-NMF algorithm, we implemented a fast, computationally efficient and accurate system, which automatically segments tumor areas according to their perfusion characteristics and extracts model-free IBs.

2. Comparison of our model-free results to pharmacokinetic model analysis results and correlation to physiological properties: the most

challenging part of our research is to quantify our results and relate them with physiological parameters. We applied state of the art model-based methods on DCE-MRI sarcoma patient data and compared the model-based biomarkers with the model-free ones. Correlation to physiological properties was performed by qualitative interpretation of obtained results with respect to previous literature findings and by comparison to histopathological findings even though these were limited.

3. Finally, all proposed methods and novel analysis frameworks were validated on longitudinal patient data (breast cancer) in order to retrospectively determine their predictive efficiency of the outcome (response vs non-response).

One of the key challenges in our research is the development of an efficient statistical classifier which will be tested on many different cancer representative cases with the purpose of validating the efficacy and accuracy of our methods. To this end, we tested our methods on different types of cancer of the same or different organs, including sarcoma and breast cancer data as previously explained.

A flowchart of the proposed methodology is presented in Figure 2 including the main implementation steps.

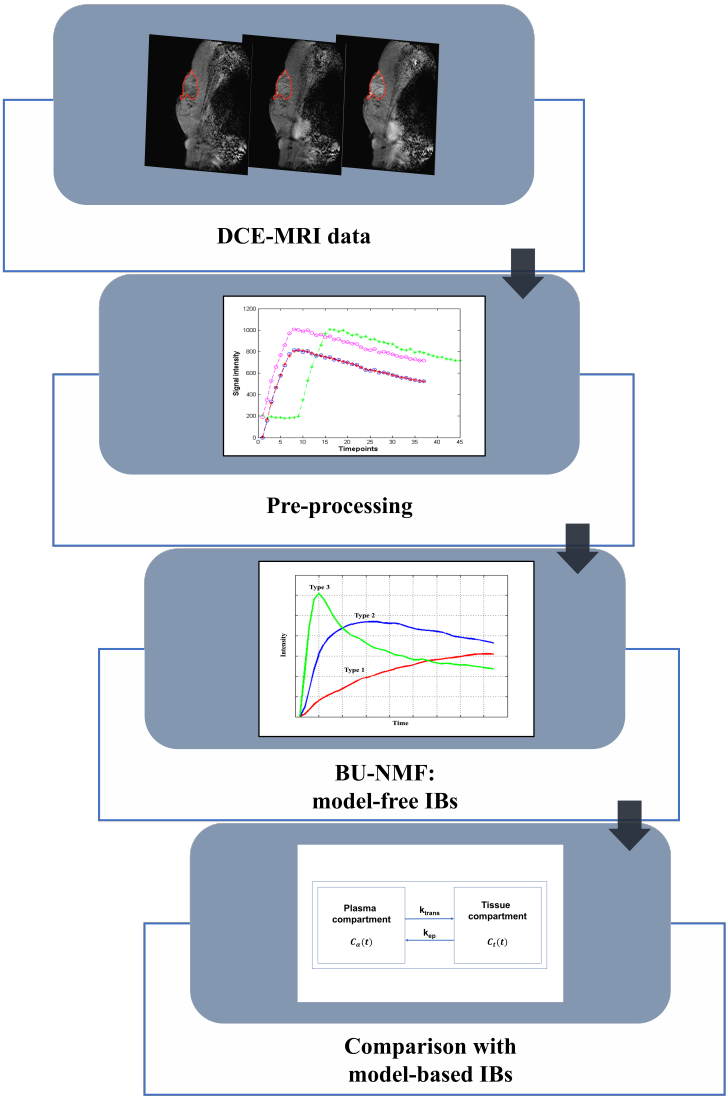

Figure 2: An overview of the image analysis framework used in this thesis.

1.4 Structure of the thesis

Chapter 1 includes the introduction to the problem of this thesis and the motivation behind it. The clinical problem of describing the tumor environment as well as the role of imaging in solving it are described. We also state the research objectives of this research. At the end of the chapter, we present the outline of the thesis.

In Chapter 2 we discuss the state of the art in the areas of our interest. These areas include our selected technique for imaging tumor physiology, i.e. the DCE-MRI technique, its principles, advantages and limitations in comparison to other imaging techniques. We then present the background of the pattern recognition techniques that have been used for the analysis of DCE-MRI data in the past years and mention the results obtained by them.

We then continue with Chapter 3 in which we describe the methods utilized in this thesis. The main subjects explained in this Chapter include the description of the NMF problem as well as the algorithms that have been proposed in previous studies for solving it. We then present in detail the algorithm selected for our experiments, i.e. the BU-NMF algorithm and the initialization methods used for increasing its robustness. Finally, the methods used for the data pre-processing and for the statistical analysis of our results are presented.

Chapter 4 begins with the data acquisition procedure followed for both the sarcoma and the breast cancer datasets. Subsequently, the findings from five different case studies are demonstrated, four concerning the sarcoma dataset and one the breast cancer dataset. In each case study, the clinical questions and the obtained results from our methods are presented.

The thesis concludes with Chapter 5 which contains a summary of the main findings obtained during the course of the PhD thesis. Results are discussed in terms of their advantages compared to previous works. Possible limitations regarding both methods and results are also explored which is then used as directions for future work.

Chapter 2

DCE-MRI fundamentals and analysis methods

This chapter includes an overview of the principles of the DCE-MRI technique. We start with a description of the fundamentals of DCE-MRI and afterwards, the most common analysis methods of DCE-MRI data are introduced. Finally, we present a summary about currently available pattern recognition techniques that are used for DCE-MRI data analysis and we discuss the advantages of this analysis method.

2.1 Overview of DCE-MRI

DCE-MRI is a widely used imaging technique and in particular in the field of radiology it can be an important additional tool in the assessment of tumors. The main asset of this technique is its safety since it does not involve ionizing radiation. What is more, it is repeatable, offers high spatial resolution and it can be performed on clinical MRI scanners with standard specifications. Most importantly, it also represents an earlier marker of tumor response since it has the ability to show physiologic alterations which occur before changes in morphology thus it outperforms conventional static MR imaging.

DCE-MRI is essentially the acquisition of serial T1-weighted MRI se-

quences before, during, and after the intravenous injection of an MR contrast medium, which is usually a low-molecular-weight gadolinium chelate. The scans are acquired for approximately 3 to 10 minutes while the CA is injected. In Figure 3 we see an example of four consecutive MRI scans, two acquired before and the other two after CA injection, from a patient with liposarcoma on the left foot. As the CA moves from the blood into the tissue, there is a change in the signal intensity of the T1-weighted image during and after the injection that depends on the vascularization and on the permeability of the tissue. This time-dependent signal intensity, or as it is commonly called time intensity curve (TIC), in the tissues is recorded from the MRI and is further analyzed so that it can provide parameters that are useful for diagnosis. More specifically, after CA administration there is a fast initial enhancement, which is then followed by wash-out. Even though this enhancement is typically higher in case of tumors with respect to normal tissue, there is significant heterogeneity in different types of tumors as well as in areas within the same tumor due to the different CA uptake. Therefore, DCE-MRI comprises a more realistic approach in describing the complex tumor biology compared to conventional MRI (Tof10). It also provides higher image contrast since T1 relaxation time increases while the CA diffuses from the arteries to the extravascular extracellular space (EES), eventually leading to increased signal enhancement (Atl09).

As for the DCE-MRI protocol, multi-slice or three-dimensional sequences are usually employed which can be acquired rapidly. Images are typically acquired using the spoiled gradient echo (SPGR) technique allowing for short repetition times. Some commonly used scanner specifications are: repetition time of 3-10ms, various flip angles, echo time¡5ms, and acquisition matrix between 128x128 and 256x256 (JPM$^+$05; MTD$^+$03). Spatial resolution is usually of a few millimeters in order to have a satisfactory signal-to-noise ratio. This affects also the temporal resolution as well as the number of slices that can be acquired, which is usually no more than 25. Consequently, there is always a trade-off between all these factors in order to achieve the best sampling at fine spatial resolution (Jac04).

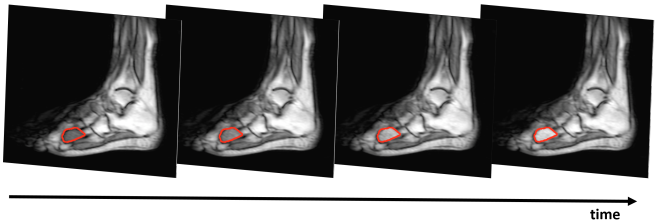

Figure 3: An example of a DCE-MRI sequence obtained from a patient with a high-grade liposarcoma.

2.2 DCE-MRI analysis methods

There are several DCE-MRI data analytic approaches, including both model-free and model-based methods (YG09). Comparison of the various published results on DCE-MRI data analysis, is a quite challenging process, due to various factors: diverse DCE-MRI acquisition protocols; large variety of post-processing approaches; different disease types, treatment settings and numbers of subjects. In light of the above, there is no standardized method for the analysis of DCE-MRI data yet, and existing methods can roughly be categorized into the following groups: a) model-based analysis using pharmacokinetic models and b) model-free analysis based on features extracted from the DCE time intensity curves. The fundamentals of these approaches are described in the following sections.

2.2.1 Model-based analysis methods

As highlighted in the previous section, the CA used for DCE-MR imaging leads to a rapid initial signal enhancement in tumor lesions in the first few seconds after being administered to the patient. This happens in the case of tumor lesions, either benign or malignant, however in normal tissue signal enhancement is not expected to increase the same as in tumor lesions. The signal enhancement and the CA concentration are closely linked, however their correlation is not straightforward since it can be influenced by various components, including tissue physiological prop-

erties or experimental factors. In general, the distribution of CA consists of three principal phases: a) the uptake phase, where the concentration in the plasma initially rises above baseline and there is a net leakage of contrast from the blood vessels into the EES, b) the plateau/equilibrium phase, where there is maximum signal enhancement with an equilibrium of the CA concentration between the vascular space and EES, and c) the wash-out phase, where the CA decreases since it starts leaving the tissue and gets out of the body through the kidneys. As for the tissue concentration, it is more complex to know when it increases or decreases since it depends on tissue physiological properties.

The first physiological models developed for DCE-MRI data analysis relied on the principles of tracer kinetics (Ket51; PB85) and considered both the CA uptake and wash-out phase as described in the previous paragraph. Pharmacokinetic models also rely on similar considerations and by using certain assumptions they attempt to mathematically describe the relation of CA concentration with the tissue physiological parameters (TGL$^+$99).

The main four steps describing the pharmacokinetic DCE-MRI data analysis (OJP$^+$12) are presented below and are also depicted in Figure 4:

1. Acquisition of a sequence of T1-weighted MR images before, during and after the intravenous injection of the CA.

2. Definition of the tumor's region of interest (ROI) and estimation of the concentration in the arterial blood known as arterial input function (AIF).

3. Conversion of MR signal intensity into concentration values.

4. Extraction of quantitative pharmacokinetic parameters through application of a pharmacokinetic model on each pixel.

In order to perform quantification of CA kinetics from signal intensities, the CA concentration should be computed at each time point of the dynamic scan. However, this is quite complex since the relationship between CA concentration and signal intensity which can generally be considered as linear, it becomes non-linear when CA concentration is high.

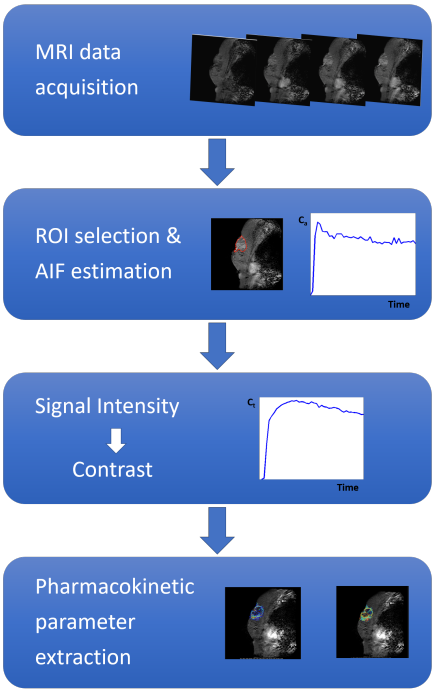

Figure 4: DCE-MRI data acquisition and analysis for a breast cancer patient: 1) image acquisition over time, 2) definition of the tumor's region of interest (ROI) and calculation of the feeding vessel arterial input function (AIF), 3) conversion of signal intensity to concentration, and 4) derivation of physiological parameters by applying pharmacokinetic modeling.

DCE-MRI pharmacokinetic analysis models are most often bi-compartmental, consisting of the blood plasma and the EES compartments, and rely on tracer kinetics as explained previously (Tof97). Multi-compartmental models have also been proposed in literature (PKH+99), however the bi-compartmental model is the most widely accepted model, since it can provide a quite good fitting of DCE-MRI data.

The bi-compartmental model does not include the intracellular space compartment, since the CA does not go into the intracellular space. This

compartmental scheme is shown in Figure 5. It is worth to say that a bi-compartmental model does not take into account the complex tumor biology.

The Tofts pharmacokinetic model (TK91; TBS95) is the most commonly used model in literature, and is described by Equation 2.1. It is considered a single-compartment model since it excludes the contribution from vascular plasma.

$$\frac{\partial C_t(t)}{\partial t} = k^{trans}\left(C_a(t) - \frac{C_t(t)}{v_e}\right) \tag{2.1}$$

where $C_t(t)$ is the CA concentration in the EES, $C_a(t)$ is the CA concentration in the arterial blood (AIF: Arterial Input Function), v_e is the volume of EES and k^{trans} represents the transfer constant from the plasma space into the EES. The solution of the above equation reduces to Equation 2.2:

$$C_t(t) = [k^{trans}e^{-k_{ep}t}] \circledast C_a(t) \tag{2.2}$$

where $k_{ep} = k^{trans}/v_e$ is the transfer constant from EES to the plasma space. Both k^{trans} and k_{ep} are measured in $[min^{-1}]$.

The extended or modified Tofts model (ETM) (Tof97) considers the additional contribution in the vasculature of the blood plasma fraction $v_pC_p(t)$. Based on this consideration, the unknown parameters are k^{trans}, v_e, and v_p. Using the convolution theorem, the solution is given by Equation 2.3:

$$C_t(t) = [k^{trans}e^{-k_{ep}t} + v_p] \circledast C_a(t) \tag{2.3}$$

The extended Tofts model produces reliable results for highly vascularized tumors in contrast to the Tofts model which is only applied for weakly vascularized tissues (SB11). Nevertheless, both models can yield to erroneous parameter calculation in cases of high vascularization while making correct data fitting. In addition, both models mistakenly assume that that the CA enters the tissue artery immediately after injection and that the CA immediately reaches the tissue (SB12).

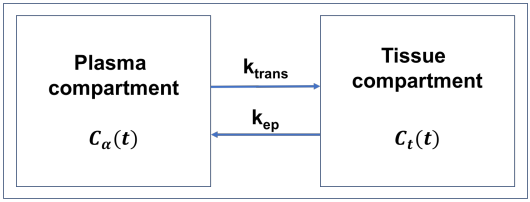

Figure 5: Two-compartment model showing one compartment representing the plasma space while the other compartment is the tissue space. The contrast agent leaves the plasma space at a rate represented by k^{trans} and returns by $k_{ep} = k^{trans}/v_e$.

The Hoffmann model (HBK+95) stems from the Brix model (BSP+91) for fast bolus injection, and relies on the assumption that the CA moves slowly from the blood plasma to the EES. The model includes a direct association between signal intensity and CA exchange rates and does not require either estimation of AIF or MR quantification. The basic equation describing the Hoffmann model is given by Equation 2.4:

$$\frac{S(t)}{S_0} = 1 + A^H k_{ep} \left(\frac{e^{-k_{ep}t} - e^{-k_{el}t}}{k_{el} - k_{ep}} \right) \tag{2.4}$$

where $S(t)$ is the MR signal course from tissue and S_0 is the MR signal before CA injection. The fitting parameters are: k_{ep} ; A^H, which approximately corresponds to the size of the EES; and k_{el}, the renal elimination constant.

The Gamma Capillary Transit Time model (GCTT) (Sch12) combines four different PK models: Tofts model, ETM, Adiabatic Tissue Homogeneity Model (ATH), and Two Compartment Exchange Model (2CX). The GCTT model introduces a new parameter (a^{-1}), which is the width of the distribution of the capillary transit times within a tissue voxel, and it has been shown that it represents the heterogeneity of tissue microcirculation and microvasculature (Sch12; BSRZ+12).

The pharmacokinetic-based analysis is quantitative since it measures intrinsic properties of the tissue. However, these models suffer from a

number of limitations, such as the complex mathematical formulations. Additionally, measurement of the blood AIF is also required for the model fitting, which is prone to errors (HM04). What is more, the conversion from signal intensity into CA concentration is quite complex as it is affected by the pre-contrast T1 relaxation rate, the CA relaxivity and the specific tissue properties. The fitting algorithms used for the calculation of model parameters are also time-consuming and they often do not lead to local minima convergence or even no convergence at all (RIS$^+$06). Another important issue is that it is difficult to achieve both high temporal and spatial resolution so there is always a trade-off between them in order to keep an acceptable signal to noise ratio (FHGKD01; HRL98). Furthermore, pharmacokinetic models often simplify the tissue perfusion process, resulting in weak correlation between the derived DCE-MRI parameters and the actual stage of the tumor (EHL$^+$03). Last but not least, these methods may have limited reproducibility in different implementations since they include many assumptions and depend on the specific tissue properties as explained previously.

In order to overcome the aforementioned limitations of PK models, data-driven methods relying on classification of the signal-time curves have been proposed in literature, as it will be discussed in the next section.

2.2.2 Model-free analysis methods

(a) **Parametric analysis of time intensity curves**

An alternative approach for obtaining useful information from DCE-MRI is by analyzing the pattern of dynamic T1-weighted intensity curves by extracting empirical parameters. Various empirical parameters are reported to have the potential to be used in cancer diagnosis. Several studies reported early wash-in and faster wash-out rates of contrast agent in prostatic carcinoma (KHC$^+$05; PODG$^+$03; RRE$^+$03). Padhani et al. showed significant differences in signal intensity variables, i.e. mean gradient and maximum signal intensity (PGM$^+$00). Maximum intensity time ratio (MITR) has

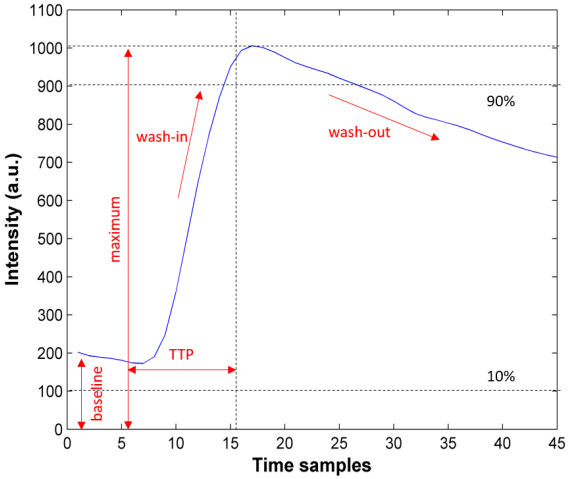

Figure 6: Example of a time intensity curve with annotated some extracted empirical parameters including wash-in, wash-out, TTP, baseline and maximum.

been proposed to distinguish the benign from malignant breast masses (FASW93; GLL+04). The definitions of these parameters are based on four landmarks on the time intensity curve: the baseline signal intensity, the maximum signal intensity, 10% of the maximum signal enhancement and 90% of maximum signal enhancement, as shown in Figure 6.

Several of these parameters are implemented in parametric analysis software (PST+98) and have been correlated with cancer tissue properties and response to treatment (PGM+00; PMG+01). The advantage of this approach is that the definitions and computation of these parameters are simple. It does not require converting the MR signal intensities into contrast agent concentrations. However, it is difficult to derive physiologic information such as permeability from these parameters.

(b) **Classification of time intensity curves**

The uptake curve of a dynamic scan is an indicator of the tissue

permeability to the CA. In particular, areas with lower permeability and perfusion tend to present a slower enhancement and the signal decreases only after the completion of the DCE-MRI scan. There has been a lot of interest in identifying specific types of the TIC shapes in the analyzed tissues and using them as a potential diagnostic tool in cancer disease (vdWVH$^+$98; vRHTB01; VL00). TIC shapes can vary across a wide range of patterns but the most common ones are three (Figure 7): Type 1: Signal intensity continues to increase persistently over time, Type 2: Signal intensity initially increases but then it reaches a plateau and Type 3: Signal intensity has a fast initial increase and then decreases after reaching the highest point. Type 3 is considered as indication for malignancy but type 1 and 2 curves can be found in cancer as well. Although this approach is sometimes described as heuristic it has been widely investigated in the last few years for the assessment of DCE-MRI.

In the last decade, a new approach has given added value to the pure TIC shape analysis. It involves the analysis of curves in a pixel-by-pixel fashion, in every single pixel acquired by the DCE-MRI scan sequence instead of the typical ROI dependent evaluation of averaged TICs (KBB$^+$07; LdJvdS$^+$07; YCYK12). Compared to the heuristic shape analysis method, this approach gives results that are more robust and less user and MRI protocol dependent. In the ROI based analysis, signal averaging in the ROI results in failing to consider important characteristics of the lesion. On the other hand, the pixel-by pixel analysis has been suggested in order to take into account the cancer spatial heterogeneity which is very important especially in the case of large heterogeneous lesions. Tissue heterogeneity can be assessed more efficiently using the pixel-by-pixel analysis as it offers higher sensitivity to spatial changes in TIC shapes.

Many recent studies use the pixel-wise analysis to perform TIC shape analysis (LM08; KBCB10) as an alternative of the quantitative pharmacokinetic models. The basic limitation of this approach

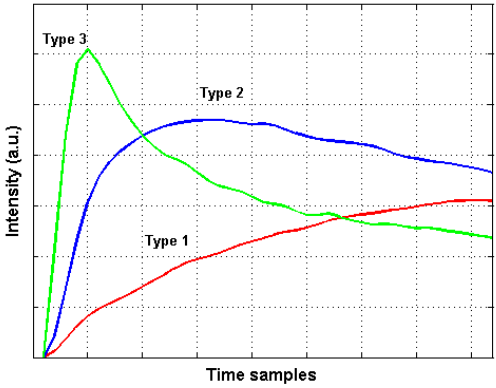

Figure 7: The three most common time intensity curve enhancement types, where Type 1 (red) is characterized by persistent slow enhancement of the SI, Type 2 (blue) by initial enhancement followed by some wash-out and Type 3 (green) by fast enhancement and fast wash-out.

is the definition of the number of required classes and yet there is no standard procedure for estimating it. In some studies they have attempted towards the automatic detection of the number of classes for example by using principal component analysis (PCA) in (EBR$^+$10) or by using statistical tests (CAT$^+$17) however it still remains an open issue that needs further investigation.

2.3 Pattern Recognition techniques for automatic TIC shape classification

Several image analysis techniques have been used in the literature in order to solve the TIC shape analysis problem. In particular, in the last few years, a number of studies have used PR techniques in order to achieve classification of the DCE-MRI data. The basic concept of PR techniques relies on the use of statistical classifiers for the automatic detection of classes that are naturally present in the DCE-MRI datasets and which are then associated with certain enhancement patterns. The main scope of

this thesis is to utilize PR techniques for the automatic extraction of patterns that can be translated into tumor physiologic characteristics and to this end we present an overview of state of the art literature where PR methods which have been applied on DCE-MRI data.

Many types of classifiers exist, including both supervised and unsupervised ones, and we will describe below the use of them for the analysis of DCE-MRI data. A comprehensive review of the model-free methods and their application to breast DCE-MRI data analysis has been published by Eyal et al. (ED09).

The most commonly used unsupervised method is PCA. In (TSG+04) Twellmann et al. used PCA to analyze breast DCE images of six patients. The PCA decomposition resulted in three significant eigenvectors and the receiver operating characteristics (ROC) curve analysis of the projection coefficients of the three eigenvectors indicated that in particular the second eigenvector gave high area under the curve (AUC) value, Az=0.996.

Another commonly used unsupervised method is independent component analysis (ICA) and its difference from PCA is the fact that it assumes that the signal we want to decompose is a linear combination of statistically independent non-Gaussian signals. Yoo et al. (YGCHHK02) used ICA to analyze breast DCE-MRI data from a six patient dataset. The ICA decomposition resulted in seven components and qualitative evaluation of the curves in each component was performed. In malignant tumors there were identified two types of enhancement patterns whereas in benign lesions there was present only one enhancement pattern. No quantitative measures were used in this work to assess its accuracy.

Artificial neural networks (ANNs) have been used in many studies (KCK+08; LKB01; TLN05) for breast DCE-MRI data analysis. Lucht et al. (LKB01) attempted the classification of TICs in a dataset of 264 patients by using eight different ANN configurations consisting of three layers. The best obtained classification results showed 84% sensitivity and 81% specificity. Twellmann et al. (TLN05) implemented an ANN-based classifier called adaptive tissue characterization network (ATCN) that combines both supervised and unsupervised methods in order to classify the

tissue as normal, benign or malignant. ROC curve analysis for each case gave a mean Az =0.988 for malignant versus both normal and benign tissue and Az=0.987 for benign versus both normal and malignant tissue.

Support vector machines have been used by Levman et al. (LLC+08) for discriminating malignant and benign breast lesions. They tested three different kernels (linear, polynomial, and radial basis function) and they also examined the effects of variations in four temporal feature vectors. The highest area under the ROC curve achieved was 0.74 and it was obtained when using a radial basis function kernel on the 4th feature vector.

Studies have also been conducted to include morphological and kinetic features in CAD schemes. Szabo et al. (SWBA04) analyzed 105 breast lesions by using six ANN models with different kinetic and morphological parameters. Poor performance was obtained when all features were used, however when selecting a specific subset of morphological and kinetic features, a high performance of Az=0.849 was achieved.

Meinel et al. (MSB+07) used backpropagation neural network to classify a combined set of shape and kinetic features from the segmented breast tumor region. Zheng et al. (ZEB+09) applied discrete Fourier transformation (DFT) to kinetic curves and extracted Hu's moment invariants from the DFT coefficients of selected two-dimensional images.

In (HKJ+15) Haq et al. used data-driven empirical parameters as well as features from PCA in combination with the least absolute shrinkage and selection operator (LASSO) for prostate cancer detection in 16 patients. They built a predictive model using the aforementioned extracted features and the support vector machine classifier with leave-one-patient-out cross validation achieving area under the ROC curve of 86%.

In (WGCL16), texture analysis was applied on DCE-MRI sub-regions derived from k-means clustering analysis. Results from 35 breast cancer patients showed that the longitudinal change of four Haralick texture features extracted from the sub-region associated with fast washout, was predictive of response to neoadjuvant chemotherapy (NAC) with AUCs varying between 75 and 80%. This is a similar approach with previous work from our group, (KKM+15) in which classification was achieved,

by utilizing glioblastoma tumor sub-regions segmented according to vascular heterogeneity derived from PK modeling.

In (HAS$^+$13; SHS$^+$12), DCE-MRI prostate cancer data have been analyzed using two different PR methods, leading to a three-area classification of the tumor in well-perfused, necrotic and hypoxic regions. In (HAS$^+$13) DCE-MRI data from a rat prostate tumor model were analyzed with a Gaussian Mixture Model (GMM)-based classification of the time intensity curves, which is an unsupervised learning method. In order to test their classification results, they investigated the spatial overlap between the three perfusion tumor areas detected by the GMM-based classification and the equivalent areas determined from 'standard' histopathological or PK methods, i.e. with hypoxic areas identified by the hypoxia marker PIMO, necrotic areas identified by hematoxylin-eosin (H&E) and well-perfused areas derived from the Hoffmann pharmacokinetic model (HBK$^+$95). They obtained 0.84 ± 0.09 overlap for the perfused area, 0.64 ± 0.15 overlap for the necrotic area and 0.72 ± 0.17 overlap for the hypoxic region.

Stoyanova et al. (SHS$^+$12) have localized hypoxic regions inside tumor areas using PCA along with constrained NMF (cNMF) (SDB$^+$04) on DCE-MRI data. They analyzed four rat prostate cancer tumors of different size, identified three significant principal components using PCA and then cNMF was applied to the data resulting in three basic signal versus time curves carrying different weights for each pixel. These weights are represented as composite color maps which refer to necrotic (blue/black), well-perfused (red) and hypoxic (green) tissue areas. This method has managed to classify the CA uptake of tumor tissue into well-perfused, hypoxic and necrotic compartments. The results have also been compared to corresponding areas identified previously in (CAC$^+$09) where multimodality imaging data was used.

In (CAT$^+$17) a statistical method was applied on principal components derived from DCE-MRI data for the automatic detection of the number of tumor areas that have dissimilar perfusion (well-perfused, hypoxic and necrotic). Afterwards, this number was used in constrained NMF in order to automatically identify the classes of tumor tissue based

on their enhancement profile. This results in tumor tissue mapping based on the identified classes. This method is applied on synthetic data, 2 pre-clinical models and 2 clinical data (sarcoma and prostate). Results were compared to histopathological information only for the clinical prostate cancer case.

To summarize, several DCE-MRI model-free analysis methods have been proposed in previous studies for cancer diagnosis or monitoring of treatment response. All these methods have their advantages and drawbacks. For example, ANNs have the capability of learning and modeling complex and non-linear problems however they usually require long computational times which is problematic in the case of large datasets and are strongly dependent on the MRI protocol. PCA on the other hand is a very simple and fast algorithm however it lacks in physical interpretation compared to NMF. To this end, we have decided to use the block-update non-negative matrix factorization algorithm (BU-NMF) for the experiments performed in this thesis. BU-NMF is an advanced NMF algorithm and its principles are described in detail in Section 3.1. We opted for using NMF instead of PCA also because NMF was demonstrated to be more pertinent to parts-based representations (LS99) due to its non-negativity constraints. In addition, NMF has been applied for the segmentation of rat prostate cancer DCE data (SHS$^+$12) as explained previously. Since such studies strongly indicate that DCE-MRI parameters convey hypoxia information, it is important to try to define automatic methods to extract hypoxia maps from DCE-MRI functional images. Design of a rapid and accurate image analysis algorithm for DCE-MRI data may have great impact on the evaluation of drug delivery as well as the development of specific treatments with antiangiogenic agents. To this end, herein we present a machine learning, model-free method that automatically decomposes the image in three dominant components corresponding to necrotic, hypoxic and well-perfused areas. What is more, in our study we use an improved BU-NMF algorithm with a robust initialization method. More importantly, herein the algorithm is used on human patient data whereas previous similar works (HAS$^+$13; SHS$^+$12) were performed on pre-clinical studies with limited number of data.

Chapter 3

Methods

The main scope of this thesis, as described previously, is to obtain a clinically useful categorization of the tumor environment in an automatic, non-invasive fashion based on information extracted from DCE-MRI data. Images often contain redundant information since adjacent pixels in an image are highly correlated. To this end, dimensionality reduction algorithms are typically used to extract the important information from the image, while incurring very little error. Matrix factorization and principal component analysis are among the most popular methods for data representation in a lower-rank space. NMF, due to its non-negativity constraints, is distinguished from other matrix factorization methods such as PCA. NMF results have more obvious visual interpretation and since it allows only additive combinations, it is suitable for uniting parts to generate a whole, leading to parts-based representations (LS99). In our work, we want to identify certain patterns associated with cancer physiology and NMF learns to represent our MRI data as a linear combination of basis images, called patterns, each of them carrying a different weight. In this way, we can identify the pattern followed by each pixel as well as the contribution of the other patterns to each pixel of the image. This allows for a visual representation, which qualitatively resembles the nature of cancer behavior. As a result, NMF consists in a relatively simple, fast and efficient method for segmenting the tumor

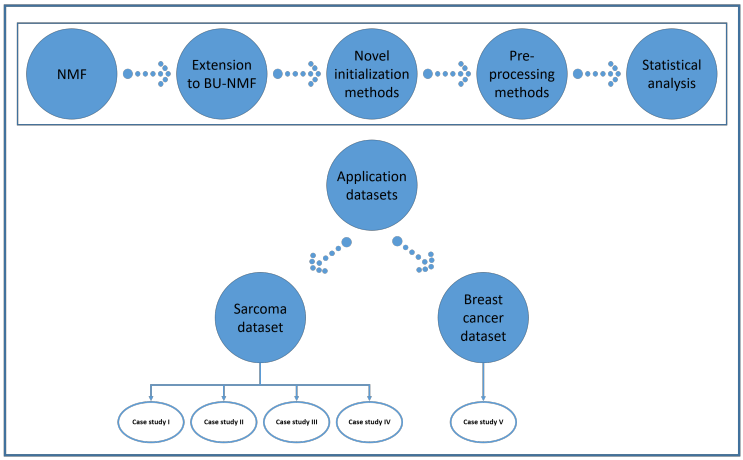

Figure 8: Methodology flowchart.

area in smaller clusters with potentially physiological interpretation. In this thesis, we have used an advanced NMF algorithm and to increase its robustness we extended it to be invariant of initialization, which is a common issue in solving the NMF problem. We introduced two innovative data-driven initialization techniques which both gave reproducible results, thus BU-NMF was rendered an efficient tool for solving the automatic TIC classification problem of DCE-MRI data.

In this chapter, we first discuss the basic principles of the NMF problem and in particular, we describe the BU-NMF algorithm and its initialization methods. Subsequently, the data pre-processing procedure is introduced. The chapter concludes with the description of the statistical methods used for the analysis of our results. The main steps of our methodology are depicted in Figure 8.

3.1 NMF methodology and initial results

In this section, we begin with a brief introduction to the NMF problem and we describe the most popular algorithms that have been used for the

solution of the NMF problem. Then, we describe the BU-NMF algorithm, which is the algorithm we have selected to employ for our experiments. In addition, we explore the main existing BU-NMF initialization approaches and we introduce two novel data-driven initialization methods. Finally, we present some initial results of the BU-NMF algorithm when applied on a synthetic dataset.

3.1.1 NMF mathematical background

The basic NMF problem consists in finding an approximate decomposition of a large dimension data matrix A of size $m \times n$ into two low-rank nonnegative matrices, $m \times k$ matrix W and $k \times n$ matrix H. The ultimate aim is to minimize the functional:

$$f(W, H) = \frac{1}{2}\|A - WH\|_F^2, \text{ subject to } W, H \geq 0 \tag{3.1}$$

The value of k is usually selected such that $k << min(m, n)$ which confirms the fact that the product $W * H$, named the NMF of matrix A, equivalents to a compressed form of A. In practice, it corresponds to the number of basic patterns that NMF is going to use in order to represent the data in A.

The minimization of Equation 3.1 involves some significant challenges. It implies the lack of convexity in both W and H, thus the existence of local minima. In addition, there is no unique solution of the minimization problem in Equation 3.1 since the solution matrices W and H could also be replaced by an infinite number of other solution pairs, such as WS and $S^{-1}H$ for any nonnegative invertible matrix S having a nonnegative inverse S^{-1}.

The NMF problem has been approached by several numerical methods resulting in different solutions (BBL$^+$07). Lee and Seung (LS01) established the first well-known NMF algorithm that is based on multiplicative update rules in order to minimize the Euclidean distance described in Equation 3.1. Particularly, it can be shown that the square Euclidean distance measure used in Equation 3.1 is nonincreasing under the iterative updated rules (BBL$^+$07) presented in Algorithm 1.

Algorithm 1 - Multiplicative update

$W = rand(m, k)$; % initialize W as random dense matrix

$H = rand(k, n)$; % initialize H as random dense matrix

for $i = 1 : maxiter$

$H = H.*(W^T A)./(W^T W H + 10^{-9}))$

$W = W.*(AH^T)./(WHH^T + 10^{-9}))$

end

Alternating least squares (ALS) algorithms (PT94) are significantly faster to converge with respect to the multiplicative update algorithms and are based on the fact that while the minimization problem in Equation 3.1 is not convex in both W and H, it is convex in either W or H. The update rules used are presented in Algorithm 2 (BBL$^+$07).

Algorithm 2 - Alternating least squares

$W = rand(m, k)$; % initialize W as random dense matrix

% or use another initialization

for $i = 1 : maxiter$

(LS) Solve for H in matrix equation $W^T W H = W^T A$

(NONNEG) Set all negative elements in H to 0

(LS) Solve for W in matrix equation $HH^T W^T = HA^T$

(NONNEG) Set all negative elements in W to 0

end

Sometimes additional constraints are applied to the standard NMF, such as smoothness and sparsity constraints. Smoothness constraints are typically used in order to compensate for the noise present in the data. On the other hand, sparseness is used in order to control the degree of sparseness of the NMF representation leading to parts-based representations with enhanced interpretability. To enforce sparsity on H, penalty

terms are used and the cost function in Equation 3.1 is extended as shown in Equation 3.2 (KP07):

$$f(W,H) = \frac{1}{2}\|A - WH\|_F^2 + \frac{\eta}{2}\|W\|_F^2 + \frac{\lambda}{2}\sum_{i=1}^{n}\|h_i\|_1^2, \quad \text{subject to } W, H \geq 0 \tag{3.2}$$

where h_i is the i^{th} column of H, $\eta > 0$ is a parameter to suppress $\|W\|_F^2$ and $\lambda > 0$ is a regularization parameter to balance the trade-off between the accuracy of the approximation and the sparseness of matrix H. This sparse NMF formulation is based on alternating non-negativity constrained least squares and further details of the algorithm can be found in (KP07).

In our work, we opted for an algorithm based on a gradient descent method, the BU-NMF algorithm, which is an efficient algorithm with simple update steps and offering global convergence under certain assumptions (XY13). It relies on regularized multi-convex optimization, which is a method used in problems characterized by non-convexity and non-smoothness.

A set of points is called block multiconvex if its projection to each block of variables is convex but can be generally nonconvex. We consider a variable x, which consists of s blocks $(x_1, \ldots, x_s)$, a set X that is a closed and block multiconvex subset of R^n, f is a differentiable and block multiconvex function, and $(r_1, \ldots, r_s)$ are extended value convex functions. The optimization problem is described by Equation 3.3 as initially described in (XY13):

$$\min_{x \in X} F(x_1, \ldots, x_s) = f(x_1, \ldots, x_s) + \sum_{i=1}^{s} r_i(x_i) \tag{3.3}$$

In Algorithm 3 it is presented the BU-NMF algorithm we used for our analysis by choosing one of the three proposed choices of update schemes in (XY13).

Algorithm 3 - Block-coordinate update method

Initialization: choose two initial points $(x_1^{-1}, \ldots, x_s^{-1}) = (x_1^0, \ldots, x_s^0)$

for $k = 1, 2, \ldots$ **do**

  for $i = 1, 2, \ldots, s$ **do**

    $x_i^k \leftarrow \arg\min_{x \in X} \langle \hat{g}_i^k, x_i - \hat{x}_i^{k-1} \rangle + \frac{L_i^{k-1}}{2} \left\| x_i - \hat{x}_i^{k-1} \right\|^2 + r_i(x_i)$ (update)[a]

  end for

  if stopping criteria are satisfied then

    return $(x_1^k, \ldots, x_s^k)$

  end if

end for

[a] In the update scheme formula used in Algorithm 3, x_i^k is the value of x_i after its k^{th} update, $\hat{x}_i^{k-1}$ denotes an extrapolated point, $\hat{g}_i^k$ is the block-partial gradient of f at $\hat{x}_i^{k-1}$ and L_i^{k-1} is the Lipschitz constant of $\bigtriangledown f_i^k$.

In (XY13) it was shown that the BU-NMF algorithm, when tested on synthetic, hyperspectral and real image datasets, it gave faster and more accurate results compared to other algorithms, such as multiplicative update, ALS, alternating direction method (ADM) and Blockpivot.

3.1.2 Evaluation of state of the art NMF implementations

In the following paragraphs, we give a short introduction to some state of the art Matlab toolboxes which contain algorithms for solving the NMF problem. We also present results from the implementation of all the NMF algorithms on a soft tissue sarcoma patient case and in particular on a lower limb malignant peripheral nerve sheath tumor (MPNST). In this way, we aim to figure out which of these algorithms can provide effective results on the TIC shape classification of a real patient cancer case. For all implementations, the NMF initialization was performed using the wash-in map, a method that is described in Section 3.1.3.

A brief description of these algorithms is given below:

- Matlab nnmf function

  We initially used the nnmf function provided by Matlab. This function solves the matrix factorization problem by using either the ALS algorithm or the multiplicative update algorithm. We first used the default ALS algorithm for our experiment since it tends to converge faster compared to the multiplicative algorithm and it is also less sensitive to initialization choices. Results from the implementation of the algorithm on sarcoma patient data are presented in Figure 9a.

  In order to optimize the results, we also tried a combination of the multiplicative algorithm and the ALS algorithm. We first calculated W and H using the multiplicative algorithm and then we used these two matrices as initialization for running the NMF with the ALS algorithm. Results are shown in Figure 9b. We notice that the curves obtained only by using the ALS algorithm are smoother and are a more reliable reconstruction of the initial data compared to using both the multiplicative and the ALS algorithm.

- NMF:DTU toolbox

  The NMF:DTU Toolbox (KSW$^+$02) contains 5 NMF optimization algorithms from which we tested the multiplicative update and the alternating least squares methods. Results from the two methods are presented in Figure 10a and Figure 10b respectively.

- NMF MATLAB Toolbox

  We have also tested the nmf algorithm with sparse constraints (Equation 3.3) provided by The NMF MATLAB Toolbox (LN13). The results of the algorithm's implementation on sarcoma patient data are presented in Figure 11. We see that the sparse NMF algorithm identified only two curves instead of the three expected ones.

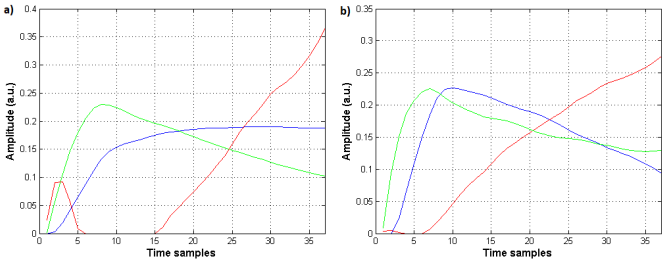

Figure 9: Matlab's nnmf algorithm results for a sarcoma patient: (a) plots of the three NMF component when the ALS method was used, and (b) plots of the three NMF component when a combination of the multiplicative update and the ALS methods was used.

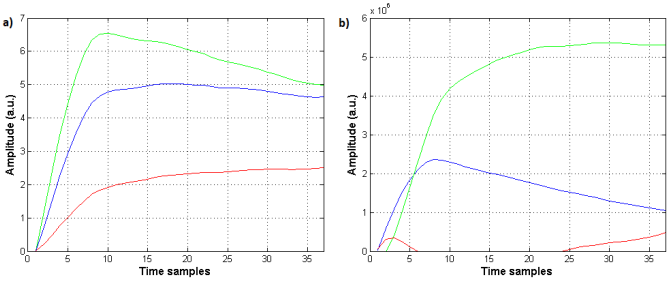

Figure 10: NMF algorithm from NMF:DTU toolbox results applied to a sarcoma patient: (a) plots of the three NMF component when the multiplicative update method was used, and (b) plots of the three NMF component when the ALS method was used.

- BU-NMF

  The code for the BU-NMF algorithm was obtained from (XY). The results of the BU-NMF algorithm when tested on sarcoma patient data are depicted in Figure 12.

From the above figures, we notice that the BU-NMF algorithm gave the best results when tested on real DCE-MRI data since the algorithm identified three distinct types of curves with shapes which correspond well to the shapes of three theoretically expected types of curves explained in Section 2.2.2. After extensive experimentation, this method

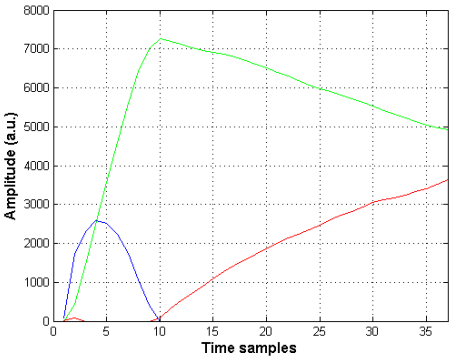

Figure 11: Sparse NMF algorithm from NMF MATLAB toolbox applied to a sarcoma patient. Plots of the two NMF components since the third component was represented by a zero plot.

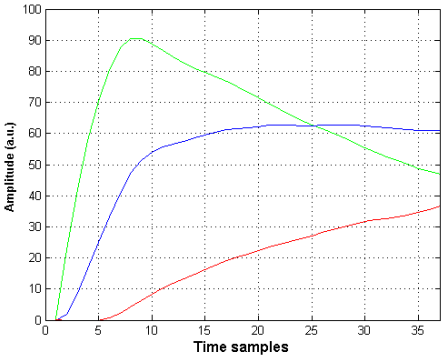

Figure 12: BU-NMF algorithm applied to a sarcoma patient. Plots of the three identified NMF components.

yielded the most robust and clinically significant results. For this reason, we have decided to employ this specific algorithm for our experiments. In the following section, we investigate the application of different initialization methods we have tried for the implementation of the BU-NMF algorithm.

3.1.3 Initialization of the BU-NMF algorithm

After having selected the BU-NMF algorithm as the most suitable PR method for our clinical experiments, we also need to decide upon some parameters which are required for its effective implementation. The main NMF problem, as stated before, is to reconstruct our input matrix A of size $m \times n$, using two lower-rank matrices, W of size $m \times k$ and H, of size $k \times n$. Therefore, in order to run the BU-NMF algorithm we need first to initialize these two matrices and also to select a value for the parameter k which principally corresponds to the number of basic patterns that NMF is going to use in order to represent the data in A. Robust initialization is of utmost importance since we need to guarantee the algorithm's reproducibility so that it can be used in the clinical setting. In the following paragraphs, we describe in detail the procedure followed for the selection of these parameters.

(I) **Low-rank matrices initialization**
Different initialization methodologies have been tested for the two low-rank matrices W and H used by the NMF algorithm however, effective initialization still remains an open problem. A brief description for some of the initialization approaches we have tested in our work is presented below with particular focus on two novel data-driven approaches introduced in our work. The following approaches concern the initialization of the basis matrix W. As for the initialization of the coefficient matrix H, after computing the initial weight matrix W_0, the H_0 matrix was initialized by the least squares solution of $A = W_0 * H_0$ where A is our given MR image data.

(i) **Random initialization**

The matrices W and H are typically initialized with random non-negative values in the standard NMF algorithm before the beginning of the iteration steps. In our case, the BU-NMF initialization relied on taking random values from the Gaussian distribution for the basis matrix W.

Random initialization of the BU-NMF algorithm was proven not to be repeatable in our experiments as it gave ambiguous results when running it for multiple times (VKN$^+$16). For a patient with lower limb MPNST, we ran the BU-NMF algorithm with two different random initializations and the results were completely different. We can see in Figure 13 that BU-NMF in one case converged to a non-interpretable solution and only nine iterations were required (Figures 13 a, b). However, when the algorithm was initialized with different random values, it converged to interpretable results (Figures 13 c, d) and 376 iterations were required for convergence.

The number of iterations required for convergence of the BU-NMF algorithm, when ran for 50 times, is shown in Figure 14 for three different sarcoma patients. Fifty consecutive runs have been carried out by using the same ROI in each run, and different random values per pixel were produced each time for the algorithm initialization. The sets of points with the three different colors depicted in Figure 14 correspond to each one of the three different patients.

For all three patients, the BU-NMF algorithm sometimes converged to interpretable solutions while others it did not. As explained before for the lower limb MPNST patient, when it converged to a non-interpretable solution, only a few iterations were required. On the other hand, when the algorithm converged to interpretable results, a greater number of iterations were required. Therefore, we concluded that the random initialization approach did not yield reproducible results and we opted for different initialization techniques, which are explained later in this section.

(ii) **NNDSVDQ initialization**

An alternate approach for initializing the NMF algorithm was proposed by Boutsidis and Gallopoulos in (BG08) and included an SVD-based initialization, which showed significant enhancement of the speed of the NMF algorithm in minimizing the cost function. Results of this initialization approach when tested on a sarcoma patient are presented in Figure 15.

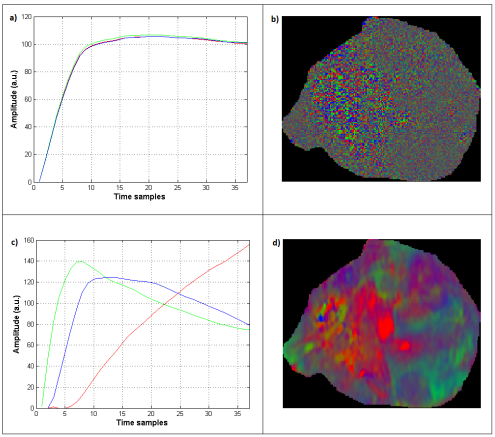

Figure 13: PR analysis results for a patient with lower limb MPNST: (a)-(b) plots of the three NMF components and the corresponding composite color map for one random initialization, and (c)-(d) plots of the three NMF components and the corresponding composite color map for a different random initialization. The composite color maps in (b) and (d) illustrate the percentage contribution of each component.

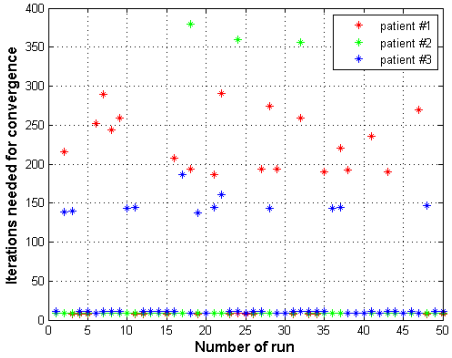

Figure 14: Number of iterations required for the BU-NMF algorithm convergence for each of 50 consecutive runs initialized randomly each time for three different sarcoma patients.

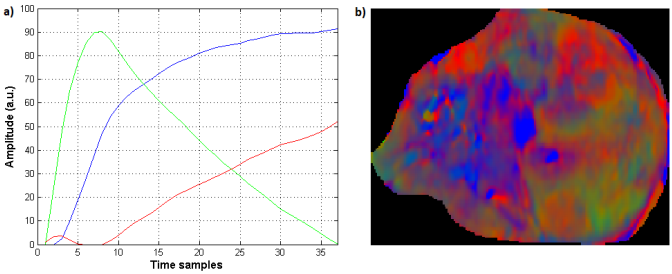

Figure 15: BU-NMF results initialized with the NNDSVDQ method for a patient with lower limb MPNST: (a) plots of the three NMF components, and (b) the corresponding composite color map.

(iii) **Proposed sophisticated initialization methods**

Two novel methods have also been tested, including a PK model as well as a simple gradient method, which were introduced in one of our published studies (VKN$^+$16) in order to address the repeatability issues of the random initialization. Results showed that when tested on the same patient data, similar results were obtained from both methods, which were also repeatable. These initialization methods relied on information extracted directly from the data allowing for a more realistic initialization of the BU-NMF algorithm. In particular, the wash-in and the k^{trans} maps were utilized for the initialization of the BU-NMF algorithm.

(iii.a) **Wash-in initialization**

For the wash-in initialization approach, the BU-NMF algorithm was initialized by classifying the tumor area in three subareas using the wash-in map extracted from the first part of the time-signal curve related to each individual pixel. A three-region classification map was derived from the wash-in map using the k-means algorithm. We tested this method on a patient with neck pleomorphic liposarcoma. Firstly, the wash-in map (Figure 16a) was used to classify the ROI into three regions as shown in Figure 16b, by using the k-means clustering algorithm.

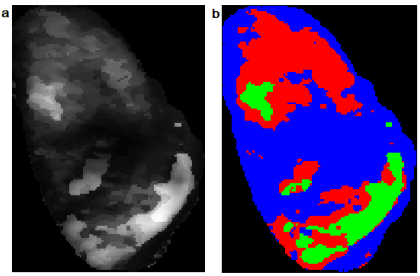

Figure 16: Initialization of the BU-NMF algorithm utilizing the wash-in part of the dynamic curves: (a) wash-in map, and (b) the corresponding three-area classification derived from k-means clustering, with green clusters representing the high wash-in areas, red representing the moderate wash-in areas and blue representing the low or no wash-in areas.

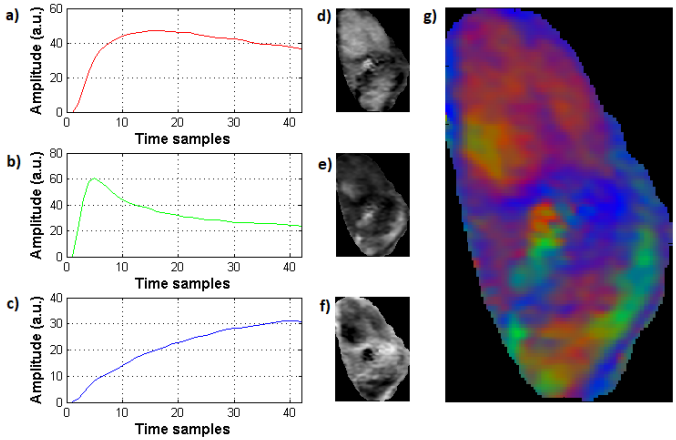

Figure 17: PR analysis results using the wash-in map initialization: (a)-(c) plots of the three NMF components, (d)-(f) the corresponding spatial maps of the NMF components, and (g) the composite color map depicting the percentage contribution of the hypoxic (red), well-perfused (green) and necrotic (blue) components.

Green clusters are related with the high wash-in areas, red with moderate wash-in and blue with low or no wash-in. This compos-

ite color map was used for the BU-NMF initialization by assigning every pixel to a single component.

The NMF components derived from the initialization of the wash-in map are shown in Figures 17a, b and c. Next to the plot of each component, the spatial map of the corresponding weight contribution is depicted in Figures 17d, e and f. Finally, in the last figure (Figure 17g) we can see the composite color map illustrating the hypoxic (red), well-perfused (green) and necrotic (blue) regions.

In the composite color map presented in Figure 17g, it is apparent that for every pixel there is a mixed contribution from all three patterns by different percentages as shown in Figures 17d, e and f. We can notice the consistency in the dynamics of the three curves with the three most common tumor enhancing curve types that were described in Section 2.2.2.

(iii.b) **PK initialization**

For the PK initialization approach, the PK model used in our analysis was the ETM, and more specifically we used the k^{trans} parameter. As explained in Section 2.2.1), ETM is more reliable for highly vascularized tissues. The contrast agent leaves the plasma space and enters the EES at a rate represented by k^{trans} and returns by $k_{ep} = k^{trans}/v_e$, which is the exchange rate from EES to the plasma space where v_e is the volume of EES. Both k^{trans} and k_{ep} are measured in $[min^{-1}]$. In our experiments, the AIF was calculated from a large vessel within the region of interest and for the signal to contrast conversion, the method of variable flip angles (VFA) was applied.

The reason for using the k^{trans} parameter is due to the fact that it is indicative of necrotic regions (SCW$^+$09) and necrosis is associated with no enhancement regions having zero or close to zero k^{trans} values. On the other hand, well-perfused areas are those associated with high wash-in and wash-out values corresponding to high k^{trans} and k_{ep} accordingly. Last, it is important to mention that hypoxic regions are expected to have intermediate perfusion

values, therefore it is hard to identify them in a straightforward way from the PK map. To overcome the difficulty of approximating the hypoxic regions, three-region clustering of the k^{trans} map was performed using the k-means algorithm, resulting in a better distinction between the areas having different perfusion values.

We tested this iniatialization approach on a patient with neck pleomorphic liposarcoma, the same one used for the wash-in initialization described previously. The parametric k^{trans} map for this patient is shown in Figure 18a. Similarly to the wash-in initialization approach, k-means clustering was applied to the k^{trans} map resulting in the three regions classification, displayed in Figure 18b. Green clusters are related with areas of high perfusion, red with areas of moderate perfusion and blue with areas of low or no perfusion.

The NMF components derived from the initialization of the k^{trans} map are shown in Figures 19a, b and c. In addition, the spatial distribution of the magnitudes of the corresponding patterns are depicted in Figures 19d, e and f. Figure 19g shows the composite color map of the three components, with the hypoxic area shown as red, the well-perfused area shown as green and the necrotic area shown as blue.

We notice that the theoretical assumptions for the three tumor microenvironments and the shape of their curve type coincide with the NMF region map and the associated NMF components. It is apparent that despite the fact that the initialization maps of the two approaches are not identical (Figure 16b, Figure 18b), the derived spatial distributions of the PR components, are almost identical (Figure 17g, Figure 19g).

The initialization maps of wash-in and PK approaches are depicted in Figure 16b and Figure 18b respectively. The two maps show significant correlation in the necrotic (blue) region whereas there is not exact correspondence for the hypoxic and well-perfused regions. After extensive experimentation, we concluded that these initialization approaches are robust in terms of repeatability. In

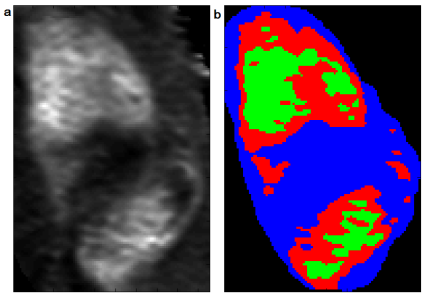

Figure 18: Initialization of the BU-NMF algorithm utilizing the k^{trans} parameter of ETM: (a) the k^{trans} map, and (b) the corresponding three-area classification derived from k-means clustering, with green clusters areas of high perfusion, red representing areas of moderate perfusion and blue representing areas of low or no perfusion.

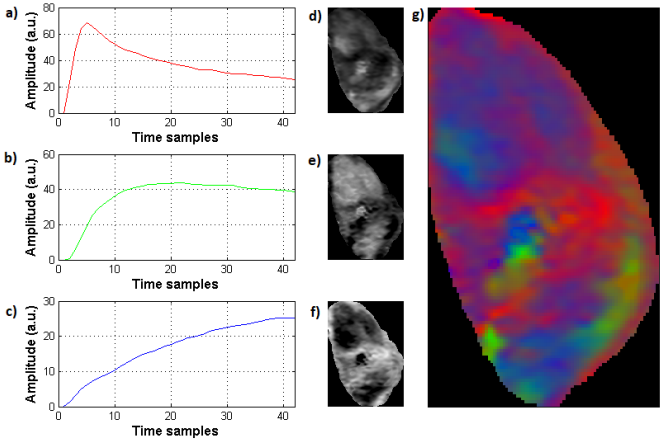

Figure 19: PR analysis results using the PK map initialization: (a)-(c) plots of the three NMF components, (d)-(f) the corresponding spatial maps of the NMF components, and (g) the composite color map depicting the percentage contribution of the hypoxic (red), well-perfused (green) and necrotic (blue) components.

particular, the wash-in approach always converged after 214 iterations while the PK one converged after 196 iterations and both

yielded the same regions. Therefore, results were reproducible when examining the same patient in contrast to the random initialization, which yielded random results after every run of the BU-NMF algorithm. In addition to this, the fact that in both initialization cases the three different NMF components have the shape of the theoretically expected DCE curves (Section 2.2.2), it further confirms the efficiency of the BU-NMF algorithm, in combination with these two initialization approaches, in automatically characterizing the enhancement profiles.

(II) **Selection of number of classes k**

(i) PCA for the selection of k

The choice of the k components in the NMF problem is usually problem dependent however, k is usually chosen such that $k > min(m, n)$ thus $W * H$ can be thought of as a compressed form of the data in A.

In order to decide about the number of components that the BU-NMF is going to seek, we performed PCA on our pre-processed data which gave us the number of principal components needed in order to retain the 99% of the data variance which is a common heuristic used when PCA is applied on images.

The temporal curves of the first four principal components are illustrated in Figure 20 together with their percentage contribution to the data variability. We can see that the first three principal components represent more than 99% of the total data variability while the fourth one is more related to noise. Based on this result, only three patterns are expected when using the NMF algorithm. Therefore, NMF is parametrized to decompose the MR signal by combining properly the three basic components.

(ii) Statistical method for the selection of k

A second method that we tested for the selection of k, is based on statistical tests and has been introduced in (CAT$^+$17). After the implementation of PCA two statistical tests are used on the identified

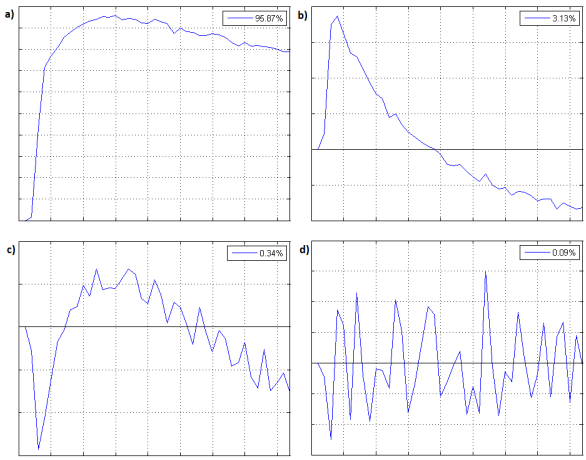

Figure 20: Four principal components found by PCA and their percentage contribution to the total data variability: (a)-(c) the first three components have the greatest contribution, and (d) the fourth one is mainly associated with noise.

principal components, namely the F-test and the Shapiro-Wilk test. The F-test is applied on the signal-related PCs and finds the number of consecutive PCs satisfying the test. The Shapiro-Wilk test on the other hand is applied on the noise-related Pcs and defines the number of consecutive PCs that failed the test. Then, k is defined as the minimum of these two numbers calculated from the two tests. However, the tests did not work on the sarcoma data which is also in line with (CAT$^+$17) since it worked only on a simulated dataset and not on clinical patient data.

3.1.4 Initial results of the BU-NMF algorithm on a synthetic dataset

We first tested the PR method on synthetic data in order to understand whether NMF is capable of producing an effective matrix reconstruction.

We create the input matrix X of size 10×50 using two other matrices: the basis matrix W is a 10×3 matrix and the coefficient matrix H is

a 3×50 matrix (Figure 21). The coefficient matrix is designed so that plots of the three patterns have the shape of the three common types 1, 2 and 3 as described previously (Figure 7). The basis matrix includes the percentage contributions of the three patterns. So, we have three combinations of 100% contribution from patterns 1, 2 and 3 respectively and 0% contribution from the other two. The remaining seven rows of W matrix include combinations of 50% contributions from 2 patterns and 0% from the third or 25% from 2 patterns and 50% from the third one and one row is for equal contribution from all 3 patterns.

For the NMF initialization, we first initialized the basis matrix. We created a 10×3 matrix W_0 where each row had a value=1 in only one of the three columns. The column was decided by computing the wash-out slope of each row of X according to the following rule:

- if slope is greater than 0, the third column of W_0 is assigned to 1 (Type 3 curve)
- if slope is equal to 0, the second column of W_0 is assigned to 1 (Type 2 curve)
- if slope is smaller than 0, the first column of W_0 is assigned to 1 (Type 1 curve)

Afterwards, the coefficient matrix H_0 was computed as the least squares solution of $X = W_0 \times W_0$. The initialization procedure is depicted in Figure 22.

In Figure 23, we present the results of the BU-NMF algorithm on the synthetic dataset using the aforementioned manual initialization. We see that the BU-NMF successfully reconstructed the three theoretically expected curves that were given as input. These results are encouraging towards the selection of the BU-NMF algorithm for the automatic TIC classification problem we want to solve on the real cancer data, which will be presented in the following chapter.

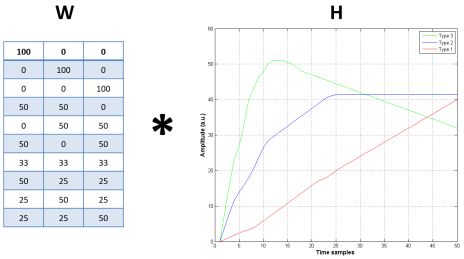

Figure 21: Synthetic data matrices used for the formation of the input matrix $A = W * H$. Left: 10×3 basis matrix W. Right: Plots of the three columns of the 3×50 coefficient matrix H.

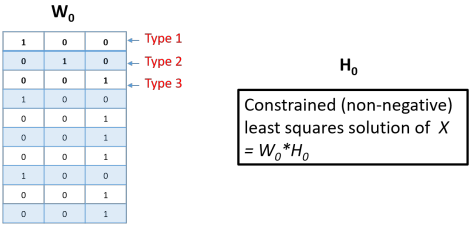

Figure 22: Initialization synthetic data matrices used for the implementation of the BU-NMF algorithm. Left: basis matrix W_0. Right: Coefficient matrix H_0.

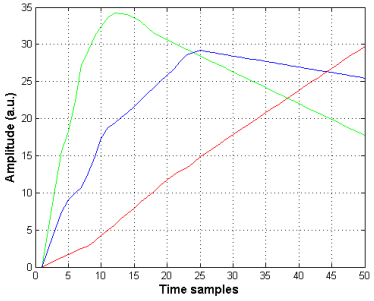

Figure 23: BU-NMF algorithm applied to synthetic data. Plots of the three identified NMF components.

3.2 Data pre-processing methods

The pre-contrast phase of the MR signal was first removed from the raw signal. A small number of pre-contrast acquisitions were obtained in order to observe the effect of the CA to MR signal intensity. Afterwards, the baseline was removed in order to extract the net effect of CA uptake on the signal intensity.

Finally, the smoothing spline method was implemented in order to remove the noise from the dynamic DCE-MRI data and obtain a smoother signal. In particular, a cubic smoothing spline algorithm was applied to the data for fitting a smooth curve to the noisy MR signal. In Figure 24, we can see the plots resulting from all the previously described pre-processing steps applied to the original intensity curve of a specific image pixel from the lower limb MPNST patient.

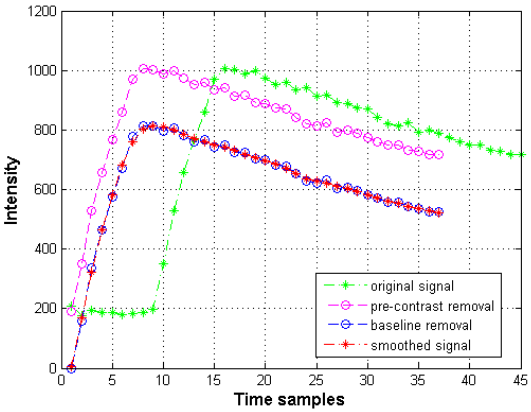

Figure 24: Pre-processing steps applied on the intensity curve of a pixel from a patient with lower limb MPNST. Pre-contrast phase was first removed, then the baseline, and finally smoothing was applied to the data.

3.3 Statistical analysis methods

For the statistical analysis of our datasets we used different methods for the two datasets. More specifically, for the soft-tissue sarcoma dataset we used the Pearson's linear correlation coefficient and shows the linear relationship between two sets of data (Pea96). The correlation coefficient equals to the covariance of two variables divided by the product of their standard deviations and takes values that range between -1 and +1. A perfect positive correlation is represented by the value +1, while the value 0 indicates no correlation and -1 indicates a perfect negative correlation. The closer the coefficient values are to +1 and -1, the stronger the relationship is between the variables.

For the breast cancer dataset, a more sophisticated statistical analysis was performed (KVM^{+}on). Statistical analysis was employed using R software (v.3.3) and results were displayed as mean $\pm$ standard deviation (mean $\pm$ s.d.). The complete workflow of the procedure is presented in Figure 25.

Firstly, a univariate analysis with the non-parametric Mann-Whitney test was applied to all calculated biomarkers to reveal any differences between the two populations (response vs non-response). For all tests, a $p - value$ of less than 5% was considered as statistical significant. A univariate predictive analysis framework was next conducted to further utilize all biomarkers that achieved a $p-value < 0.05$ using five different classifiers. The main scope of this study was twofold; a) to validate the discriminative power of the proposed by the statistical analysis biomarkers through a predictive analysis infrastructure using several classifiers, and b) assess their predictive accuracy in an unbiased way using subsets of the examined dataset that were not used for training. Initially, the examined cohort was randomly divided into stratified test and train sets comprising 20% and 80% of each examined biomarker respectively. A repeated k-fold cross validation was next performed at the training phase to prevent or reduce any overfitting issues. K-fold cross validation was repeated 10 times with k equal to 3 due to sparsity of the training set. At the testing phase, all statistically significant biomarkers and models

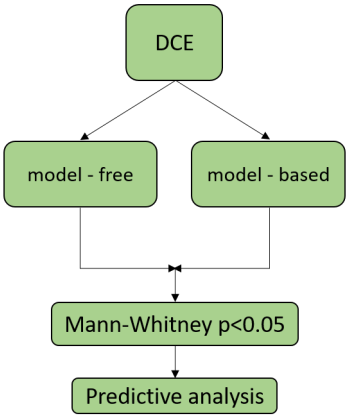

Figure 25: Analysis workflow of the proposed framework for analysis of the breast cancer dataset. DCE biomarkers are extracted from model-free and model-based methods and are used for statistical analysis. Afterwards, a univariate predictive analysis was applied to all the statistically significant biomarkers.

were validated using the "unseen" test sets. To better assess the generalization performance of the biomarkers, the aforementioned steps were repeated 50 times using exactly the same input data during each iteration and their performance was provided quantitatively using mean and standard deviation of the AUC, F1 score, accuracy, sensitivity and specificity.

To examine whether a combination of the statistically significant biomarkers would potentially increase the results in terms of the predictive accuracy, a wrapper feature selection using recursive feature elimination (RFE) and the five suggested classifiers was applied to the examined cohort. For the convenience of the reader, ensemble adaboost with decision trees of level one, extreme gradient boosting linear, support vector machine with linear kernel, random forest, and the k-nearest neighbor were presented using acronyms clf1, clf2, clf3, clf4 and clf5, respectively.

Chapter 4

Results

During the course of this thesis, we have used different datasets for our experiments such as glioblastoma, endometria, sarcoma and breast cancer data. However, we encountered difficulties with certain datasets, thus our research focused on sarcoma and breast cancer data. The sarcoma dataset included six patients, four with liposarcoma (Patients #2, #3, #5, and #6) and two with MPNST (Patients #1 and #4). All MRI scans for the sarcoma dataset were provided anonymously by the Department of Medical Imaging of the University General Hospital of Heraklion after getting approval by the local Ethical Committee. The fully anonymized data were obtained from patients who underwent both conventional and DCE-MRI examinations. After the diagnosis of soft tissue sarcoma was established by core needle biopsy, surgical resection of the lesion was performed in all cases. Histopathology figures and findings were provided anonymously by the Department of Pathology of the University General Hospital of Heraklion. The breast cancer dataset we used included 35 patients and was a publicly available dataset (LAA$^+$16).

In this chapter, we present five different case studies, four concerning the sarcoma dataset and one the breast cancer dataset. We first describe details of the MRI acquisition protocols used for the two datasets. Then, the MRI visualization and analysis tools used in this thesis are presented. Subsequently, the clinical questions and the results of our methods for

each case study are presented in Sections 4.2-4.6. The main results stem from the model-free PR approach using the BU-NMF algorithm. In addition, the PR results were compared in some cases with other methods, such as with model-based DCE and DW-MRI methods.

The results reported in Chapter 4 are based on the publications (VKN$^+$16; VSdB$^+$18; VKdB$^+$18; NMV$^+$18) and on (KVM$^+$on) that has been recently submitted for publication:

- M. Venianaki*, E. Kontopodis*, K. Nikiforaki, E. de Bree, T. Maris, A. Karantanas, O. Salvetti, K. Marias, "Improving hypoxia map estimation by using model-free classification techniques in DCE-MRI images," *2016 IEEE International Conference on Imaging Systems and Techniques (IST)*, pp. 183-188, 2016.

- M. Venianaki, O. Salvetti, E. de Bree, T. Maris, A. Karantanas, E. Kontopodis, K. Nikiforaki, K. Marias, "Pattern recognition and pharmacokinetic methods on DCE-MRI data for tumor hypoxia mapping in sarcoma," *Multimedia Tools and Applications*, vol. 77, no. 8, pp. 9417-9439, 2018.

- M. Venianaki, A. Karantanas, E. de Bree, T. Maris, E. Kontopodis, K. Nikiforaki, O. Salvetti, K. Marias, "Assessment of soft-tissue sarcomas perfusion using data-driven techniques," *2018 IEEE EMBS International Conference on Biomedical & Health Informatics (BHI)*, pp. 353-356, 2018.

- K. Nikiforaki, G. C. Manikis, M. Venianaki, E. Kontopodis, E. Lagoudaki, T. Maris, K. Marias, E. de Bree, A. Karantanas, "Perfusion and Oxygenation Changes after Isolated Limb Perfusion with TNF - α in Lower Limb Sarcoma: A Case Report," *Biomedical Research and Reviews*, vol. 1, no. 1, p. 101, 2018.

- E. Kontopodis*, M. Venianaki*, G. C. Manikis, K. Nikiforaki, O. Salvetti, E. Papadaki, G. Z. Papadakis, A. Karantanas, K. Marias, "Investigating the role of model-based and model-free IBs as early predictors of neoadjuvant breast cancer therapy outcome," *IEEE*

Journal of Biomedical and Health Informatics, submitted for publication.

4.1 Data acquisition

The MRI data used in this thesis were obtained using specific acquisition protocols. In this section, we give a brief description of the MRI protocols used for both the sarcoma and breast cancer datasets.

- **MRI protocol for sarcoma dataset**

  Patients were imaged in a $1.5T$ Siemens-Erlangen scanner. The CA gadopentetate dimeglumine (Gd-DTPA), $0.1\ mmol/kg$ body weight, was injected intravenously before the DCE-MRI. Six separate T1-weighted (w) MR sequences were obtained before the CA injection, with variable flip angles of $5°$, $10°$, $15°$, $20°$, $30°$ and $60°$. T1-w MR sequences were acquired with fast three-dimensional spoiled gradient echo (SPGR) ($TR = 7\ ms$, $TE = 3.23\ ms$, $FA = 15°$, temporal resolution $6.44\ s$, 14 slices and 45 time points for DCE-MRI protocol). The acquisition matrix was 192×121 for all sarcoma patients except for Patient #6 which was 320×288. Voxel size was $1.04 \times 1.65 \times 5\ mm$ for Patients #1, #3, #4, and #5. For Patient #2 voxel size was $1.15 \times 1.82 \times 5\ mm$ while for Patient #6 it was $1.25 \times 1.39 \times 4\ mm$. Datasets were co-registered to the DCE-MRI arterial phase (maximum signal-to-noise ratio).

- **MRI protocol for breast cancer dataset**

  DCE and multiple flip angles (mFAs) data were acquired on a $3.0T$ Philips Achieva MR scanner using a 16-channel bilateral breast coil. The acquisition of mFAs included flip angles from $2°$ to $20°$ by 2 degrees increment, whereas DCE flip angle was $20°$. Imaging parameters for both DCE and mFAs protocols were $TR = 7.9\ ms$, $TE = 4.6\ ms$, $192 \times 192 \times 20$ image resolution, $220 \times 220\ mm^2$ field of view (FOV) and slice thickness $5mm$, while in DCE temporal resolution was $16\ s$ and 25 dynamic acquisitions were acquired. The Gd-DTPA CA was administered via a power injector

using $0.1\ mmol/kg$. A detailed description of the DCE protocol is provided in (LAA+15).

4.1.1 MRI visualization and analysis tools

Osirix Dicom viewer was used in order to visualize and save appropriately the DCE-MRI images. We loaded the DICOM folder with the DCE images provided by the University General Hospital of Heraklion on a DVD-ROM drive. Osirix was used on an Apple MacBook Pro having 2.6GHz Intel Core i5 processor with 8 GB RAM. In order to import the desired data in the Osirix database we click on File→Import→DICOM file(s) and then select the Dicom folder we want to import. Afterwards, while being on the Documents DB window, we select the imported folder and we click on the arrow on the left of patient's name to expand the contents of the folder. We then find the perfusion folders we are interested in, we double click on each of them and then click on Export → DICOM file(s) and save them in a folder of our preference. In order to proceed to the next step of our data analysis, we had to create two folders, the 'perfusion' folder containing the DCE perfusion data and the 'angles' folder containing all the different angles that were considered under the MRI protocol.

A dedicated software tool was employed for the DCE-MRI data analysis (KKS+16). Design of ROIs was implemented in this tool as well as calculation of the pharmacokinetic parameters.

All the numerical results presented in this work have been obtained by Matlab 8.1.0.604 (R2013a) implemented on an Intel Core 2 i7-4770 processor, 3.4 GHz with 16 GB RAM.

4.2 Case study I: Three sarcoma patients

Soft-tissue sarcomas are malignant neoplasms usually arising from soft tissues, like muscle, fat, blood vessels but can also start from any part of the body. They exhibit high heterogeneity with more than 50 different subtypes identified, yet they are quite rare in humans compared

to other cancers. **In our first case study, our main aim was to characterize the heterogeneous environment of three sarcomas through automatic TIC shape classification and associate the enhancement patterns to necrotic, hypoxic and well-perfused areas. The robustness of two novel initialization methods used for the BU-NMF has also been investigated. Finally, we have also tried to associate some limited histopathological results with the algorithmic findings**.

In this section, we present results from three male patients, with median age 58 years, who were diagnosed with soft tissue sarcomas, and more specifically:
Patient #1: lower limb (calf) MPNST classified as poorly differentiated (Grade III) MPNST with large necrotic areas.
Patient #2: thigh pleomorphic liposarcoma with several necrotic regions.
Patient #3: neck pleomorphic liposarcoma with necrotic regions centrally in the tumor.

Results from both the wash-in and PK map initialization of the BU-NMF algorithm are illustrated in the following figures. In Figures 26, 27 and 28 the results from the BU-NMF implementation using wash-in initialization, are presented for Patients #1, #2 and #3 respectively. In Figures 26a, 27a and 28a the plots of the three NMF components are depicted and in Figures 26b, 27b and 28b the corresponding composite color maps are illustrated, showing the contribution of the three components to each individual voxel. Each image voxel is characterized by a mixture of well-perfused (green), hypoxic (blue) and necrotic (red) regions. The results of the PR analysis using the PK map initialization, containing the NMF plots are shown in Figures 26c, 27c and 28c while the composite color maps are depicted in Figures 26d, 27d and 28d for each of the three patients respectively. We notice that for all three patients, the three different NMF components have the shape of the theoretically expected DCE curves (Figure 7), confirming the efficiency of the BU-NMF algorithm in automatically characterizing the enhancement profiles. In addition, considering the apparent high variability in the initial conditions the method in all cases yields consistent results.

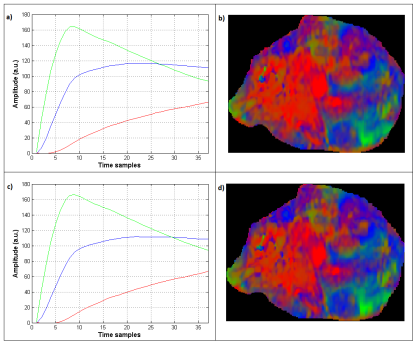

Figure 26: PR analysis results for Patient #1: (a)-(b) plots of the three NMF components and the corresponding composite color map using the wash-in map initialization, and (c)-(d) plots of the three NMF components and the corresponding composite color map using the PK map initialization. The composite color maps in (b) and (d) describe the percentage contribution of the well-perfused (green), hypoxic (blue), and necrotic (red) components.

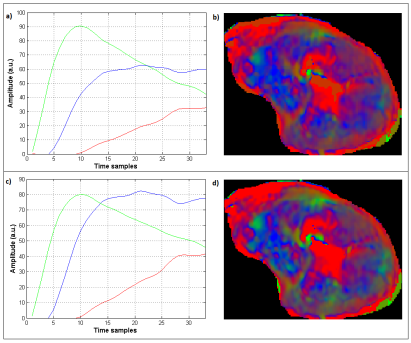

Figure 27: PR analysis results for Patient #2: (a)-(b) plots of the three NMF components and the corresponding composite color map using the wash-in map initialization, and (c)-(d) plots of the three NMF components and the corresponding composite color map using the PK map initialization. The composite color maps in (b) and (d) describe the percentage contribution of the well-perfused (green), hypoxic (blue), and necrotic (red) components.

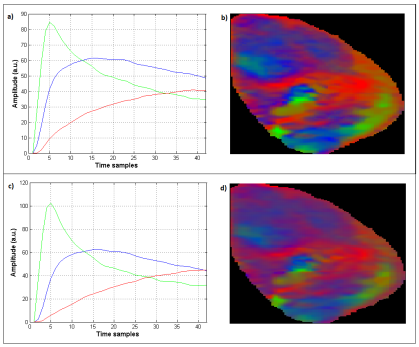

Figure 28: PR analysis results for Patient #3: (a)-(b) plots of the three NMF components and the corresponding composite color map using the wash-in map initialization, and (c)-(d) plots of the three NMF components and the corresponding composite color map using the PK map initialization. The composite color maps in (b) and (d) describe the percentage contribution of the well-perfused (green), hypoxic (blue), and necrotic (red) components.

4.2.1 Statistical analysis results

Statistical analysis of our results was performed using Pearson's linear correlation coefficient in order to investigate the correspondence between the hypoxic, well-perfused and necrotic components derived from the two BU-NMF initialization approaches. The correlation coefficient can range between -1 and +1, which we corresponded to percentages ranging between -100% and 100%. All image correlations described in the following paragraphs have been computed following image background removal, thus taking into account only the tumor ROI pixels. The results are presented in Table 1 for all three patients.

We notice that the highest correlation percentages (greater than 91%) appear when the same components from the two different BU-NMF implementations are compared e.g. hypoxic component from wash-in initialization with hypoxic component from PK initialization. As expected, all comparisons of different components exhibit either low or negative correlations.

The relationship between the BU-NMF classification and the k^{trans}

Table 1: Correlation (%) between the hypoxic, well-perfused and necrotic components using the two initialization schemes for the BU-NMF algorithm. Pt stands for Patient, HYP for Hypoxic, WP for Well-perfused, and NEC for Necrotic

	Wash-in								
	HYP			WP			NEC		
PK	Pt #1	Pt #2	Pt #3	Pt #1	Pt #2	Pt #3	Pt #1	Pt #2	Pt #3
HYP	**98.1**	**99.6**	**96.4**	-17.1	-12.4	-25.7	-74.6	-85.1	-76.4
WP	-4.3	5.7	-18.9	**99.8**	**91.1**	**98.8**	-51.3	-49.0	-46.4
NEC	-87.8	-82.1	-71.4	-43.4	-45.6	-44.7	**99.1**	**97.0**	**98.2**

map three-region classification using k-means clustering, was also investigated and the derived correlation percentages are presented in Table 2. The BU-NMF classification results were obtained from Patient #1 using the wash-in initialization method. Similar results were obtained when the PK initialization was chosen instead. Correlation is dominant when the same regions are compared even though percentages are not as high as in Table 1, ranging between 38.4% and 66.9%. The necrotic components show the highest correlation (66.9%) whereas well-perfused and hypoxic components show lower correlation, i.e. 46.0% and 38.4% respectively. This might be due to the fact that the k^{trans} parameter is indicative of necrotic regions, as explained in Section 3.1.3, but is not able to distinguish well between the well-perfused and hypoxic regions when a simple classification method as k-means is used. Negative or low correlation percentages were observed when different components from the two methods were described.

In order to get a further understanding of the extracted tumor hypoxic regions, we focused on comparing only the hypoxic map extracted from the BU-NMF algorithm with the entire k^{trans} map (Table 3). Correlation percentages varied between 23.7-43.2%, which does not give very much evidence of correlation between the two methods.

Subsequently, we applied a double thresholding technique on the k^{trans} image in order to approximate the location of the hypoxic region in the tumor. The rationale for this is that the hypoxic areas will exhibit

Table 2: Correlation (%) between the BU-NMF (wash-in initialized) and the k^{trans} (clustered by k-means) hypoxic, well-perfused and necrotic components for Patient #1. HYP stands for Hypoxic, WP for Well-perfused, and NEC for Necrotic

	k^{trans}		
BU-NMF	HYP	WP	NEC
HYP	**38.4**	6.9	-42.9
WP	23.8	46.0	**-54.9**
NEC	-0.5	-31.2	**66.9**

Table 3: Correlation (%) between the k^{trans} map and the hypoxic map extracted from BU-NMF with different initialization schemes. Pt stands for Patient, and HYP for Hypoxic

	k^{trans} versus BU-NMF HYP map / Wash-in	**k^{trans} versus BU-NMF HYP map / PK**
Pt #1	32.3	23.7
Pt #2	43.2	39.4
Pt #3	38.9	40.5
Mean	38.1	34.5

a k^{trans} profile greater than the necrotic ($k^{trans} = 0$) but less than the well-perfused areas ($k^{trans} \rightarrow 1$). We tested different threshold values and we identified the upper and lower bounds in the k^{trans} image that lead to the highest correlation between the image derived from k^{trans} thresholding and the hypoxic region derived from BU-NMF (Table 4). It is noticeable that for all three patients the mean of these bounds was lying in a range between 0.15 and 0.76 approximately, with k^{trans} taking on values in a range of 0-1, leading to a maximum mean correlation with BU-NMF results of around 52% (i.e. mean of 51.1% and 53.6% which are the mean maximum correlations for wash-in and PK initialization). From this, we could assume that the necrotic image regions according to our classification exhibit k^{trans} values lower than 0.15, well-perfused exhibit k^{trans} more than 0.76 and hypoxic regions lie in between these two thresholds. This assumption is reasonable since the hypoxic k^{trans}

Table 4: Correlation (%) between hypoxic maps extracted from the k^{trans} map and BU-NMF and corresponding k^{trans} bounds. Pt stands for Patient

	k^{trans} versus BU-NMF with Wash-in			k^{trans} versus BU-NMF with PK		
	Correlation (%)	**k^{trans} lower bound**	**k^{trans} upper bound**	**Correlation (%)**	**k^{trans} lower bound**	**k^{trans} upper bound**
Pt #1	53.0	0.14	0.52	48.6	0.12	0.70
Pt #2	57.7	0.06	0.77	55.8	0.05	0.77
Pt #3	50.2	0.28	0.76	49.0	0.29	0.81
Mean	53.6	0.16	0.68	51.1	0.15	0.76

range is in line with findings claiming that the bulk of the tumor consists mainly of hypoxia; hence, the periphery of the tumor, which typically relates to the normoxic/well-perfused area, occupies smaller space (SCW$^+$09; NTC$^+$13). Necrotic regions instead are those with k^{trans} close to zero, occupying a smaller space with respect to hypoxia. However, in our case the necrotic region seemed to be overestimated by a small percentage of 15%, which can be explained by the limitation of MR imaging resolution and partial volume effect. As a result, voxels with values close to zero that are adjacent to necrotic regions with $k^{trans} = 0$ may also be considered as necrotic. Similar assumptions for the k^{trans} range were used in a recent study (ROT$^+$15), which deals with the delineation of tumor physiological regions through the application of a cancer predictive model aiming to predict patients' glioblastoma progress.

Hence, we conclude that from the double thresholding technique we used on the k^{trans} image, the BU-NMF hypoxic regions best correlated to k^{trans} image with values between 0.15 and 0.76 approximately, well-perfused areas to k^{trans} above 0.76 and necrotic regions to k^{trans} below 0.15. These results are in agreement with published results and findings on tumor hypoxia as explained in the previous paragraph.

4.2.2 Qualitative findings from histopathological reports

After permission, tissue slides of the surgical specimens of three patients were retrieved from the archive of the Pathology Laboratory of the University General Hospital of Heraklion and were histopathologically re-evaluated by a certified pathologist. Furthermore, FFPE (formalin-fixed

paraffin-embedded) blocks of the areas of interest were also retrieved and $3\mu m$ thick tissue sections were cut and were mounted on charged glass to perform immunohistochemistry. Specifically, Ki67 (Clone MIB-1, mouse monoclonal antibody, DAKO) and CD34 (Clone QBEnd-10 mouse monoclonal antibody, DAKO) antibodies were applied at validated dilutions and incubation times. The findings indicated consistency in the morphological characterization of the three lesions regarding the existence of necrotic areas sporadically distributed within the tumors. In addition, all three tumors have been characterized by regionally high proliferation rates.

Specifically, for Patient #1 who was diagnosed with MPNST sarcoma, the immunohistochemical biopsy evaluation demonstrated: a) high cell proliferation index (Ki67), b) high cellularity, and c) positive values of CD34 endothelial marker indicating high microvessel density. We can assume that regions with high cellularity and vascularization might indicate either lack of adequate oxygenation of the tumor, hence hypoxic regions, or presence of well-perfused areas. This finding is also confirmed by the BU-NMF analysis results for Patient #1, which showed the presence of both well-perfused and hypoxic regions in the tumor (Figure 26).

To summarize, results of this first case study indicated that it is possible to characterize the heterogeneity of three different sarcomas using our model-free method. The three BU-NMF components identified for the three patients had the characteristic shapes of the three theoretical enhancement patterns, thus resulted in discrimination of well-perfused, hypoxic and necrotic areas within each of the three tumors. The existence of necrotic areas in the three tumors has also been confirmed by the histopathological reports of the three patients. From the double thresholding technique we used on the k^{trans} image, we identified k^{trans} ranges for each of the three regions, i.e. hypoxic regions best correlated to k^{trans} image with values between 0.15 and 0.76, well-perfused areas to k^{trans} above 0.76 and necrotic regions to k^{trans} below 0.15 which are in agreement with (SCW$^+$09; NTC$^+$13) as explained previously. In terms of the BU-NMF algorithm initialization, we have shown the robustness of both the k^{trans} and PK map initialization methods since they gave

consistent tumor classification results for all three patients.

4.3 Case study II: Two MPNST patients

Among the experiments carried out in this thesis, we have examined two patients having the same type of tumor, MPNST according to histopathological evaluation. However, the perfusion profiles were completely different in the two tumors, in the sense that one of them did not exhibit any necrosis at all. **To this end, in the specific case study we investigated the possibility to automatically assess differences in the same type of tumor based on PR. By comparing PR classification results between the two cases, it is possible to reveal early indication of tumor grading, something which is currently achieved only through histopathology.**

The first patient, mentioned as **Patient #1**, was affected by lower limb MPNST with large necrotic areas, as explained in Section 4.2, while the second patient, mentioned as **Patient #4**, was affected by upper limb (humerus) MPNST which was classified as well-moderately differentiated (Grade I-II) MPNST with no presence of necrotic areas. In Figures 29a, b and c the plots of the three NMF components for Patient #1 are illustrated and in Figure 29d the ROI pixels are colored as a mixture of the three components, the well-perfused(green), hypoxic (blue) and necrotic (red) component. The results of the PR analysis for Patient #4 are shown in Figure 30 and in contrast to the other patient, only two components are identified instead of three, the well-perfused and hypoxic one. We notice that the shape of the well-perfused curves in Figures 29a and 30a and of the hypoxic curves in Figures 29b and 30b are similar for both patients and are also in line with the theoretically expected DCE curves as explained in Section 2.2.2.

4.3.1 Examination of intensity plots of classified pixels

The robustness of the BU-NMF algorithm was further tested by examining the DCE intensity plots of the pixels classified by the algorithm as well-perfused (WP), necrotic (NEC) or hypoxic (HYP) in order to explore

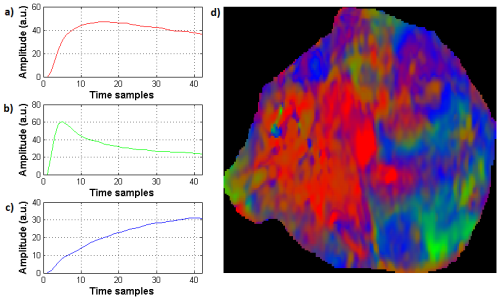

Figure 29: PR analysis results for Patient #1: (a)-(c) plots of the three components, i.e. well-perfused, hypoxic, and necrotic respectively, and (d) composite color map showing the percentage contribution to each pixel of the well-perfused (green), hypoxic (blue) and necrotic (red) components.

if they are consistent.

Following the BU-NMF classification, pixels were further classified in unique WP, HYP and NEC clusters. This included normalization of the NMF weight values between 0-1 and further classification of the pixels by assigning to them one of the three components according to the following criteria:

- Pixel x is HYP if and only if the NMF weight of the hypoxic component of the pixel $>$ threshold
- Pixel y is WP if and only if the NMF weight of the well-perfused component of the pixel $>$ threshold
- Pixel z is NEC if and only if the NMF weight of the necrotic component of the pixel $>$ threshold

where threshold = [0.5, 0.6, 0.7, 0.8]. This range of thresholds was chosen due to our working hypothesis that a pixel is characterized as HYP, WP or NEC when it is comprised at least 0.5 (50%) of one of the three components against the total value that is derived from all three components and equals to 1.

In Tables 5 and 6, the total percentages of the WP, HYP and NEC pixels are presented when different threshold criteria are applied for Pa-

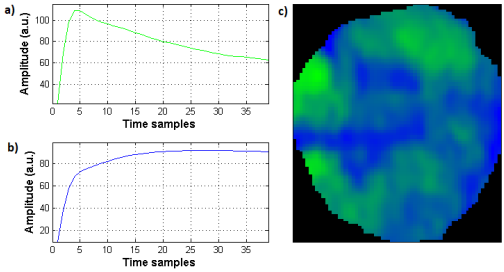

Figure 30: PR analysis results for Patient #4: (a)-(b) plots of the two components, i.e. well-perfused, and hypoxic respectively, and (c) composite color map showing the percentage contribution to each pixel of the well-perfused (green) and hypoxic (blue) components.

tients #1 and #4 respectively. We can see that as the threshold becomes stricter i.e. the higher value it has, a smaller percentage of pixels are clustered as HYP, WP or NEC. This is something expected since the cancer environment is heterogeneously perfused so each pixel does not have a completely distinct perfusion profile due to the inherent limited resolution.

In Figures 31, 32 and 33 the intensity plots of a number of clustered WP, HYP and NEC pixels from Patient #1 are depicted for different classification thresholds at 50%, 70% and 80% respectively. We randomly selected around twenty pixels from each category (WP, HYP and NEC) and depicted their intensity curves for each classification threshold. Similarly, in Figures 34, 35 and 36 the intensity plots of a number of clustered WP, HYP and NEC pixels from Patient #4 are depicted for the different thresholds, i.e. 50%, 70% and 80% respectively.

From the intensity curves shown in Figures 31-36 it can be seen that as the threshold increases, the image pixels are clustered into more homogeneous areas (especially the WP pixels) with respect to their enhancement profiles. The HYP curves show also a little delay in reaching the maximum with respect to WP curves, which agrees with the theoretical DCE curves of Type 2 which show delayed enhancement compared to the Type 3 curves (KMK$^+$99). Furthermore, the delayed enhancement of

Table 5: Percentage of pixels (%) clustered as purely WP, HYP or NEC when a classification threshold between 50-80% is applied on the BU-NMF classification results for Patient #1. HYP stands for Hypoxic, WP for Well-perfused, and NEC for Necrotic

Threshold for classification	HYP	WP	NEC
50%	31.7	5.1	42.1
60%	19.6	2.5	30.7
70%	9.9	1.0	21.1
80%	3.5	0.4	10.8

Table 6: Percentage of pixels (%) clustered as purely WP, HYP or NEC when a classification threshold between 50-80% is applied on the BU-NMF classification results for Patient #2. HYP stands for Hypoxic, WP for Well-perfused, and NEC for Necrotic

Threshold for classification	HYP	WP	NEC
50%	65.7	34.3	0
60%	45.4	17.1	0
70%	21.8	6.3	0
80%	9.7	2.9	0

the HYP curves is in agreement with 18F-Fmiso PET studies reporting that HYP regions show enhancement at later times after CA injection, with lower initial activity than WP areas but more persistent enhancement through time (CAC$^+$09). Finally, the shapes of the WP, HYP and NEC intensity curves look similar to the corresponding WP (Figures 29a and 30a), HYP (Figures 29b and 30b) and NEC (Figure 29c) pattern curves found by the BU-NMF. This finding strengthens the effectiveness of our method in finding the correct enhancement pattern of each image pixel.

To summarize, in Case study II the BU-NMF algorithm was applied on two MPNST sarcomas and identified three different patterns in Patient #1 and two in Patient #4, with the NEC pattern missing in the latter. This was in accordance with the histopathological report of Patient #4, which indicated lack of NEC regions. These findings could assist in

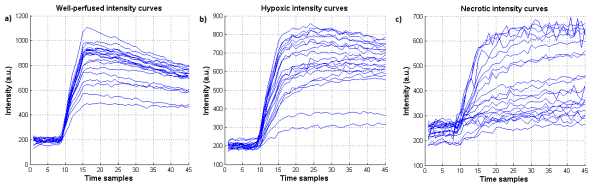

Figure 31: Intensity plots of image pixels clustered as well-perfused, hypoxic and necrotic at threshold 0.5 for Patient #1.

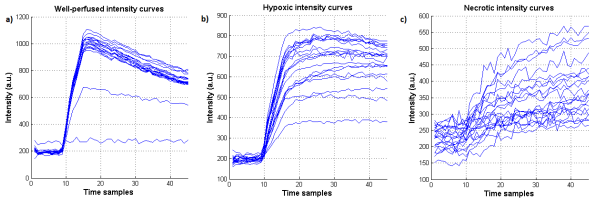

Figure 32: Intensity plots of image pixels clustered as well-perfused, hypoxic and necrotic at threshold 0.7 for Patient #1.

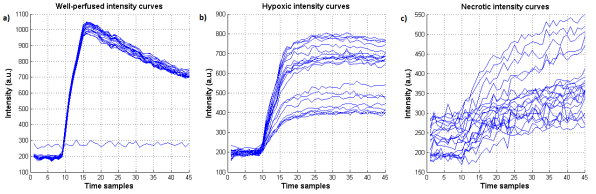

Figure 33: Intensity plots of image pixels clustered as well-perfused, hypoxic and necrotic at threshold 0.8 for Patient #1.

classification of the malignancy grade by identifying different number of patterns in tumors of the same type. A second classification step was implemented after the BU-NMF, by applying four different thresholds in order to assign to each pixel a single component and not a mixture of all the identified BU-NMF components. The percentages of WP, HYP and NEC pixels were calculated for each threshold and for each patient separately showing that the higher the threshold, the fewer were the pixels that were classified as purely WP, NEC or HYP.

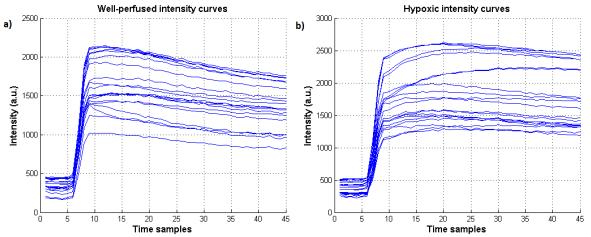

Figure 34: Intensity plots of image pixels clustered as well-perfused and hypoxic at threshold 0.5 for Patient #4.

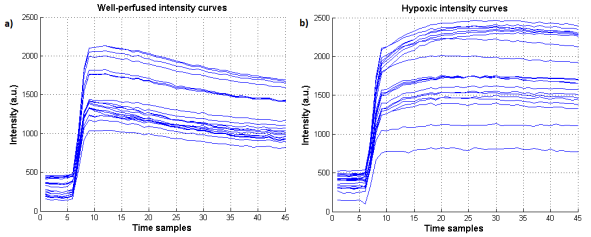

Figure 35: Intensity plots of image pixels clustered as well-perfused and hypoxic at threshold 0.7 for Patient #4.

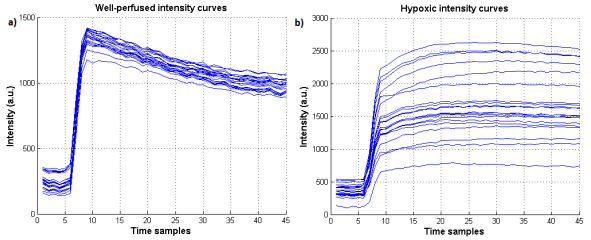

Figure 36: Intensity plots of image pixels clustered as well-perfused and hypoxic at threshold 0.8 for Patient #4.

4.4 Case study III: Liposarcoma patient follow-up after ILP

In this case study, we have examined a particular case of a young patient with a high-grade myxoid liposarcoma on the left foot, mentioned as **Patient #5**, who underwent isolated limb perfusion (ILP) with tumor necrosis factor alpha (TNF-α) and melphalan, which is a quite novel technique. MRI scans, provided anonymously by the Department of Medical Imaging of the University General Hospital of Heraklion, were analyzed before and after the therapy after getting approval by the local Ethical Committee. Histopathological figures and findings were provided anonymously by the Department of Pathology of the University General Hospital of Heraklion. Three different techniques have been used for the evaluation of tumor response to therapy, DCE-MRI, DW-MRI and T2* relaxometry (T2*r). **To our knowledge, MRI analysis of TNF induced perfusion has only been studied in animals (PWTH$^+$04) and has shown changes in endothelial permeability after therapy as measured by perfusion biomarkers. This case study assesses the vascularity changes in a lower limb sarcoma after ILP with TNF-α, based on non-invasive MRI methods.** To this end, clinically relevant perfusion biomarkers extracted from DCE-MRI, DW-MRI and T2*r have been used for the evaluation of tumor response to therapy for the patient with high grade myxoid liposarcoma.

ILP has been used for locally advanced soft tissue sarcoma of the extremities in order to avoid amputative surgery when wide excision is not feasible (JH16). This therapy helps in reducing tumor size so that a marginal excision of the tumor can be performed after a few weeks of therapy administration. ILP is usually combined with TNF-α and melphalan. The reason behind this is that TNF-α is linked with increased uptake of chemotherapeutic drugs, such as melphalan, into the tumor as well as with selective destruction of tumor neovascularization (LKL01). In addition, increased vessel permeability and reduced interstitial pressure have been reported among the early effects of TNF-α administration (JG96) which can induce a huge increase (up to six-fold) of melphalan up-

take into the tumor (dWtHdB$^+$00). Conversely, late antivascular effects including endothelial apoptosis and tumor vessel disintegration, which may eventually lead to tumor necrosis, are best elucidated using imaging methods before and after ILP with TNF-α (RYB$^+$98) and this is also the main subject of our work in this case study.

In this case study, a myxoid-fleshy structure in the tissue was observed at histological examination of the lesion of Patient #5. The lesion presented a subtle multinodular conformation, exhibited areas of variable cellular density with enhancement of cellularity at the periphery, and was composed of bland fusiform or round cells suspended individually in a myxoid matrix with a prominent network of arborizing thin-walled capillary vessels, often in a 'chicken-footprint' configuration (Figure 37).

With regards to the DCE-MRI data, the BU-NMF algorithm was applied in order to identify the main enhancement patterns which characterize the tumor before and after therapy. In addition, the pharmacokinetic k^{trans} metrics was measured using the ETM model.

In addition to the DCE-MRI method, the DW-MRI method can also provide metrics indicative of vascularity. Intravoxel incoherent motion (IVIM) model of DW-MRI may separate microcirculatory from thermal diffusion effects and can be used to study microcirculatory blood flow properties by estimating the microperfusion fraction f (Fed17), i.e. the fraction of DW-MRI signal arising from incoherent blood flow motion.

A third MRI method related to blood supply, is BOLD-MRI, which indirectly measures the total amount of deoxyhemoglobin (dHb) levels in a voxel. Conceptually, the paramagnetic nature of deoxyhemoglobin as opposed to oxyhemoglobin, accelerates T2* relaxation, shortening thus T2* constants of tissue around the blood vessels. Importantly, dHb levels depend on a number of concurrent phenomena such as blood flow, blood oxygenation, vasculature, hemoglobin levels etc. (HRM$^+$01). Because of the complex interplay between blood supply and oxygen extraction, changes in oxygen delivery (blood flow) are not directly related to changes of oxygen consumption and dHb changes do not always match the expected action of the vascular stimulus. T2*r can provide infor-

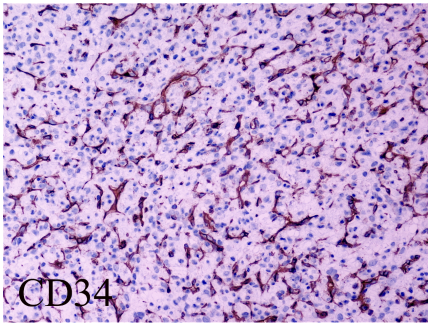

Figure 37: CD34 stain highlights the thin-walled mostly arborizing vasculature (Original magnification $\times 200$).

mation regarding tumor microenvironment as it reflects tissue oxygen bioavailability. Larger T2* tissue constants as a result of lower dHb concentration, may indicate lower blood flow, lower tissue oxygenation, deficient vascular network etc., and is consistent with tumor response to therapy (RLH$^+$17).

The BU-NMF results showed that before therapy there is prevalence of the hypoxic enhancement pattern, i.e. 68.59% (Figure 38). In addition, baseline perfusion study showed strong enhancement and further post processing with specific DCE and DW-MRI software (KKS$^+$16; MNPM16) evaluated high k^{trans} (mean 0.424 mL/g/min) (Figure 39a) and f values (mean 33.5%), indicating functional vessel network to the neoplasm. T2*r showed a mean value for the 3D tumor ROI of 72 ms.

In addition to the MRI measures, some quantitative immunohistochemistry results (CD34) were also computed regarding intratumoral microvessel density (iMVD) before therapy. The CD34-stained neoplastic vasculature, consisted mostly in fine arborizing vessels with diameter greater than 0.6 mm and newly formed vessels of one to three endothelial cells. Vessel rich hot spots areas were located in the tumor periphery and interestingly correlated closely with the areas having the highest tumor cell proliferation activity (Figure 37). Two methods were used to assess iMVD: a) microvessel counting (WSWF91), and b) the relative microvessel area estimate ('Chalkley count') (Cha43). The absolute num-

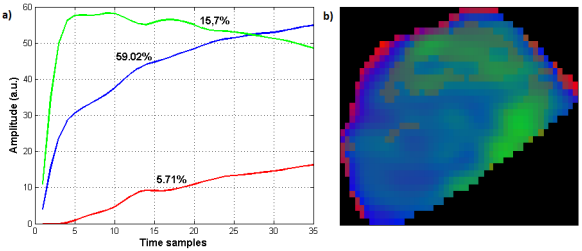

Figure 38: PR analysis results for Patient #5 before TNF therapy: (a) plots of the three NMF components, and (b) the corresponding composite color map describing the percentage contribution of the well-perfused (green), hypoxic (blue), and necrotic (red) components. The hypoxic pattern (blue) is the principal pattern before TNF therapy.

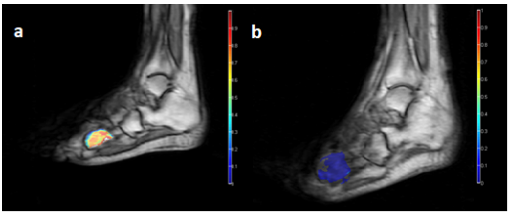

Figure 39: Screenshot from in-house built software platform for DCE longitudinal analysis (LAA^{+}15). Pixel-based parametric (k^{trans}) maps from a single tumor slice: (a) before, and (b) after TNF therapy.

ber of the vessel count obtained in the three fields ($\times$200) was 290, 282 and 264, respectively, resulting in a mean of 280.3 vessels. Chalkley grid score of each hot spot was 14, 18 and 16, respectively, resulting in a mean Chalkley count of 16. In light of the above, we can assume that regions with positive iMVD thus with high vascularization, might indicate either lack of adequate oxygenation of the tumor, hence hypoxic regions, or presence of well-perfused areas. This is in accordance with the aforementioned MRI findings, i.e. high k^{trans} and f values, prevalence of the hypoxic component and small T2* constant.

Since follow-up MRI was performed two months after therapy, our work focused on the late vascularity changes, such as tumor vessel dis-

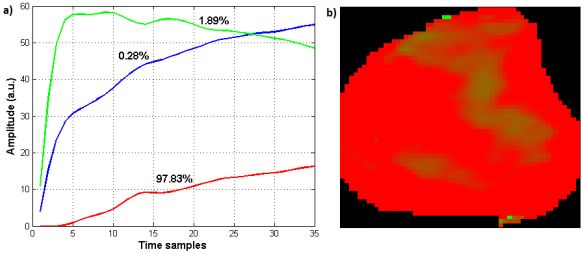

Figure 40: PR analysis results for Patient #5 after TNF therapy: (a) plots of the three NMF components, and (b) the corresponding composite color map describing the percentage contribution of the well-perfused (green), hypoxic (blue), and necrotic (red) components. The necrotic pattern (red) is the dominant pattern after TNF therapy.

integration and endothelial apoptosis. Identical protocol showed minimal foci of enhancement and reduced number of pixels (873 before vs 618 pixels assigned as tumor after therapy, counted in 128×128 DW-MRI images) in the ROI volume. In addition to the shrinkage of the tumor enhancement area, response to therapy was also confirmed by our PR approach, which showed that after therapy the necrotic enhancement pattern is dominant, representing a percentage of 97.83% of image pixels (Figure 40). The transition of the tumor from the hypoxic to the necrotic state is in line with the expected outcome of the ILP with TNF-α therapy as explained in the beginning of this section. The k^{trans} and f metrics showed also remarkably reduced perfusion (Figure 39b) and blood flow respectively in the whole tumor volume (mean k^{trans} was reduced from 0.424 to 0.099 mL/g/min and mean f was reduced from 33.5 to 7.3%), strongly indicating severe impairment of the vessel network. In addition, T2* relaxation became slower after therapy (mean T2* was increased from 72 to 82 ms), implying decreased levels of deoxyhemoglobin thus deprived oxygen supply. All the aforementioned MRI findings suggest that the tumor positively responded to therapy. More importantly, our PR method results compare favorably to results from widely accepted MRI biomarkers, such as k^{trans} and f biomarkers, which is encouraging in prediction of response to therapy using model-free biomarkers.

To summarize, in Case study III the BU-NMF method has detected a shift from hypoxic to necrotic state of the tumor after ILP with TNF-α therapy confirming response to therapy. Three additional MRI methods gave results that were consistent with response to therapy, further confirming the efficiency of our model-free method. Although there is no absolute threshold to characterize tumor proliferation, hypoxia or necrosis, relative changes of perfusion characteristics such as the BU-NMF extracted principal enhancement patterns before and after therapy could be used to effectively assess response after therapy.

4.5 Case study IV: Preliminary histopathological results for a liposarcoma patient

In the following, we present results from a patient who was diagnosed with retroperitoneal dedifferentiated liposarcoma, mentioned as **Patient #6**. **The clinical question we want to explore in this case study is whether we can correlate DCE-MRI findings with results from histopathology and more specifically with H&E and HIF-1α findings.**

We have first performed our PR method for the specific liposarcoma, using the BU-NMF algorithm resulting in two components with the necrotic component being the dominant one (91.83%) in contrast to the well-perfused one (8.17%) represented by the red and green plots respectively in Figure 41a. It is noticeable that the two curves have comparable shapes to the theoretical ones (Figure 7). The BU-NMF composite color map (Figure 41b) also seems to correspond well with the k^{trans} map (Figure 41c) obtained from the ETM model when examined for a specific tumor slice and ROI. Necrotic areas depicted as red in the BU-NMF map corresponded well to the low k^{trans} areas, shown as blue in Figure 41c. Well-perfused, i.e. green areas in the BU-NMF map also corresponded well to medium (green) k^{trans} areas with the exception of some well-perfused areas in the upper left of the ROI (Figure 41b) in the BU-NMF map, which were mismatched with low k^{trans} areas in the k^{trans} map.

As a next step to our analysis, we tried to associate the DCE-MRI findings with the histopathological findings. In particular, the existence

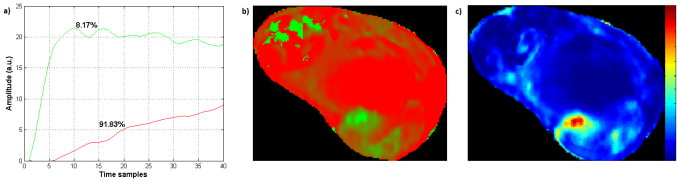

Figure 41: DCE-MRI model-free and model-based results for Patient #6: (a) plots of the two identified BU-NMF components, i.e. the well-perfused (green) and the necrotic (red) components, (b) BU-NMF composite color map showing percentage contribution of each component to image pixels, and (c) ktrans map extracted from the ETM pharmacokinetic model.

of necrotic areas was firstly assessed on H&E stained tumor sections (Figure 42) sampled at positions corresponding to the middle slice of the MRI images. The bright pink color in the major part of the H&E image suggests large necrotic areas in the specific tumor.

Apart from the necrotic pattern, which seems to dominate the specific tumor, there is also a small area evident in the upper part of the tissue section in Figure 42, which shows a different structure and corresponds to the structure of a well-differentiated tumor area. The extracted BU-NMF map as well as the H&E images taken from two locations of the two heterogeneous tumor areas are shown in Figure 43. The corresponding biopsy sections of these two areas are also depicted in the right part of Figure 43.

Besides the H&E findings, we have also examined histopathological images obtained after the immunohistochemical staining of tumor sections with the HIF-1α antibody (mouse monoclonal clone ESSE122, Abcam) and compared them with DCE-MR images as shown in Figure 44. In the right part of Figure 44 we see the photo of a specific area of the tumor section after immunohistochemical staining with HIF-1α. The area was chosen with special care so that it corresponded to the DCE-MRI ROI which exhibited heterogeneous perfusion. HIF-1α staining also demonstrated heterogeneous performance and the areas of expression (well-differentiated areas) are depicted as dense areas at the rims of the necrosis in the figure, in contrast to the null expression in the necrotic area

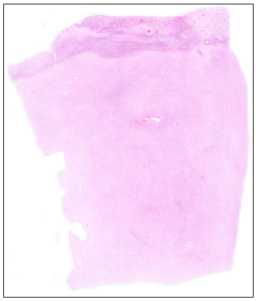

Figure 42: Image obtained from H&E stained tumor sections depicting the necrotic behavior of a dedifferentiated liposarcoma (Original magnification $\times 20$).

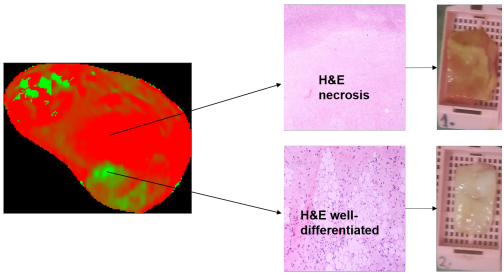

Figure 43: BU-NMF results compared with H&E images of Patient #6. Left: BU-NMF composite color map extracted for a selected ROI. Center: Images from H&E stained tumor sections from necrotic and well-differentiated areas of the excised tumor (Original magnification $\times 200$). Right: Biopsy images of corresponding parts of the excised tumor right after surgery.

sparse and necrotic areas where it was not expressed and were associated to necrotic areas in the BU-NMF map.

To summarize, in Case study IV we have examined the BU-NMF method on a dedifferentiated liposarcoma and compared results with histopathological H&E and HIF-1α images. BU-NMF identified the presence of necrotic and well-perfused areas, which were also present in the histopathological images. However, correlation of DCE-MRI and histopathology needs to be further investigated by assessing more histopatho-

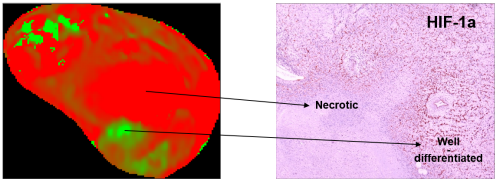

Figure 44: BU-NMF results compared with HIF-1α image for Patient #6. Left: BU-NMF composite color map, extracted for a selected ROI, consisting of well-perfused (green) and necrotic (red) areas. Right: HIF-1α (Original magnification $\times$200). The HIF-1α image shows areas of expression (dense pink) corresponded to BU-NMF well-differentiated areas, and areas of no expression (bright pink) corresponded to BU-NMF necrotic areas.

logical parameters and extract quantitative information from them.

4.6 Case study V: Breast cancer dataset

Breast cancer is the most frequent cancer diagnosed in women worldwide (FSD$^+$15) and is the leading cause of cancer deaths among women. NAC is considered the gold standard for locally advanced breast cancer treatment as it can lead to a more successful breast surgery by reducing the tumor size that needs to be excised and by possibly curing micrometastases earlier than adjuvant treatment (LMY$^+$10).

In this particular case study, the clinical motivation was to understand whether DCE model-free biomarkers can predict treatment response early in the course of NAC therapy. To the best of our knowledge, this is a novel study employing imaging-based tumor environment classification PR techniques for predicting NAC response. In addition, compartmental model-based biomarkers were also used in order to align our analysis with previous ones based on DCE-MRI and also identify possible correlations of model-based, PR biomarkers with respect to NAC prediction.

In this case study, a public available dataset was analyzed (LAA$^+$15; LAA$^+$16; CVS$^+$13) which included DCE-MRI, DW-MRI and PET/CT data from breast cancer patients acquired before, during and at the end

of NAC. The complete breast cancer dataset includes 59 patients with histologically-proven breast cancer of stage II/III. The details of the specific therapeutic regimens followed for each patient are available in (LAA$^+$15). Moreover, each patient was classified as pathological complete response (pCR) or non-pCR according to a biopsy specimen acquired at the end of all NAC sessions. Complete response was associated to the lack of tumor residual in both breast and lymph nodes which is in accordance with Sataloff (SMP$^+$95).

From the 59 patients included in the complete dataset, 20 patients had only PET/CT exams so these were excluded. From the remaining 39 patients four patients were excluded since they had only one DCE exam, so the dataset that was analysed in this study included 35 patients with two or three DCE longitudinal imaging studies. The analysed patient cohort included 12 pCR and 23 non-pCR patients, having a baseline and a follow-up exam whereas few of them (4 pCR and 8 non-pCR) had also a second follow-up exam.

In the following paragraphs, we describe the results of the PR and the model-based methods applied to the breast cancer dataset. For the statistical analysis of the dataset, the prognostic value of four model-based ($k^{trans}, k_{ep}, v_e, v_p$) and three model-free (well-perfused, hypoxic, necrotic) biomarkers, measured at each imaging time point, as well as their percentage changes from baseline to first follow-up (Δk^{trans}, Δk_{ep}, Δv_e, Δv_p, Δwell-perfused, Δhypoxic and Δnecrotic) were investigated.

The slope and time to peak of the curves assigned to hypoxic and well-perfused PR components were first calculated and then the mean percentage differences between the two components were computed for all exams. Results confirmed our initial hypothesis about the shapes of Type 2 and Type 3 enhancement curves (Figure 7). Specifically, the mean percentage differences showed 72% increased slope and 189% decreased time to peak of the well-perfused component compared to the hypoxic one. This is illustrated in Figure 45 where the three BU-NMF components from a pCR patient are depicted. This initial test was a quality control assessment of our proposed method in order to ensure consistency across all patient data.

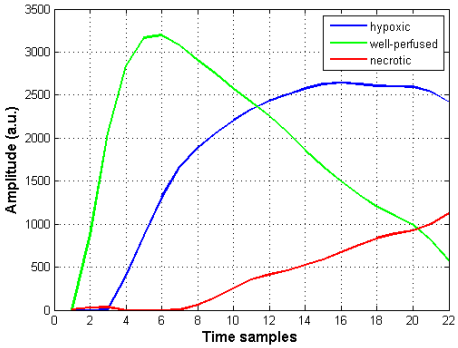

Figure 45: The three resulted BU-NMF components for a pCR patient. Green curve is the well-perfused component, blue is the hypoxic and red is the necrotic one complying with the theoretical type 3, 2 and 1 curves respectively.

For the statistical analysis of the DCE model-free derived features, the data fed to the statistical algorithm were organized as follows: the tumor ROI of each exam was clustered by the BU-NMF algorithm in three areas based on the three derived BU-NMF components. Afterwards, three different threshold criteria were used in order to assign a unique cluster to each pixel. In particular, a pixel was characterized as well-perfused, hypoxic or necrotic depending on a) the BU-NMF component (well-perfused, hypoxic or necrotic) with the greatest percentage contribution in the pixel (threshold 1), or b) the BU-NMF component (well-perfused, hypoxic or necrotic) with the highest percentage contribution in the pixel provided that this contribution is greater than 0.4, otherwise this pixel is omitted from clustering (threshold 2) or c) the BU-NMF component (well-perfused, hypoxic or necrotic) with the greatest percentage contribution in the pixel provided that this contribution is greater than 0.5, otherwise this pixel is omitted from clustering (threshold 3). In the rest of the thesis, the three aforementioned thresholds will be mentioned as thr1, thr2 and thr3. Afterwards, the percentage number of well-perfused, hypoxic and necrotic pixels against the total number of ROI pixels from each exam were computed for every threshold.

Therefore, for each exam 18 different percentages were calculated including the well-perfused, hypoxic, necrotic, Δwell-perfused, Δhypoxic and Δnecrotic percentages for each of the three thresholds, thr1, thr2 and thr3.

In Figure 46a, the results of the BU-NMF algorithm for a non-pCR breast cancer patient are presented, where the percentage contribution of the three PR components is depicted for all the ROI pixels. After application of maximum threshold, i.e. the pixel is characterized according to the BU-NMF component with the greatest percentage contribution (Figure 46b), each pixel is assigned to a single component. For stricter thresholds of 0.4 and 0.5 (Figures 46c and d) some pixels which do not have high enough contribution of any of the three components are not included at all in the BU-NMF clustering and are depicted as black in Figures 46c and d. The hypothesis in adding these thresholds is that we effectively increase classification accuracy by only considering pixels with stronger percentage contributions in one of the three tumor environment image classes.

For the model-based analysis, the DCE exams were processed using a specific software platform for DCE longitudinal analysis written in Matlab (KKS$^+$16). For SI to contrast agent concentration conversion, mFAs data were used. Considering the absence of an artery or vein in the FOV of the majority of DCE exams, a theoretical arterial input function (AIF) from Weinmann (WLM84) was used for all analyses. It should be considered that assuming the same theoretical AIF for all patients may influence the accuracy of the extracted biomarkers. That said, image-based AIF computation is also prone to errors since large vessels may be out of the FOV or may suffer from partial volume effect, or may have an inaccurate flow profile especially for image acquisition in sagittal plane.

The PK analysis was based on the Extended Tofts Model (Tof97), that estimates the volume transfer constant k^{trans} $[min^{-1}]$, the interstitium to plasma rate constant k_{ep} $[min^{-1}]$, the interstitial volume v_e (dimensionless) and the plasma volume v_p (dimensionless). Extracted biomarkers were then limited in ranges with biological significance i.e. $k^{trans} < 5$ $[min^{-1}]$, $v_e < 1$ and $v_p < 1$, whereas pixels with values out of these

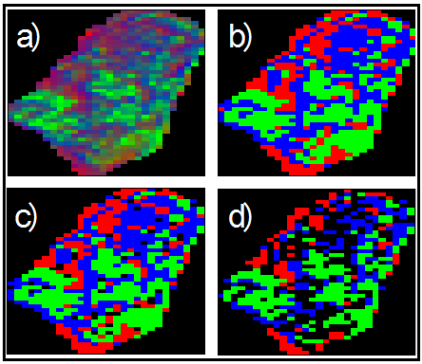

Figure 46: BU-NMF composite color map showing percentage contribution of the well-perfused (green), hypoxic (blue) and necrotic (red) components: (a) without thresholding, and with application of (b) maximum threshold, (c) threshold of 0.4, and (d) threshold of 0.5.

ranges were excluded from the statistical analyses. Finally, for every model-based resulted biomarker (k^{trans}, k_{ep}, v_e, v_p) the mean, median and 5^{th}, 15^{th}, 80^{th} and 90^{th} percentiles were computed respectively for the statistical analysis.

From the statistical analysis, three measures of the model-free hypoxic percentage biomarker were revealed to have statistical significance (p-value$<$0.05) at the first follow-up, namely hypoxic thr1, hypoxic thr2, Δhypoxic thr2. In Figure 47 the extracted map of the hypoxic biomarker is depicted for both a non-pCR (first 2 columns) and a pCR patient (last 2 columns) for the baseline and the first follow-up exam. Regarding the model-based biomarkers, five measures from two model-based biomarkers were revealed to have statistical significance at the first follow-up, namely k_{ep} median, v_e median, v_e mean, v_e 80^{th} percentile and v_e 90^{th} percentile.

As a second step, five classifiers were utilized in order to test the predictive ability of the model-free biomarkers. The model-free and model-based biomarkers that showed non-random predictive value (sensitivity or specificity $>$50%) as well as their percentages of AUC, F1 score, sensitivity and specificity are presented in Table 7. Median values of k_{ep}

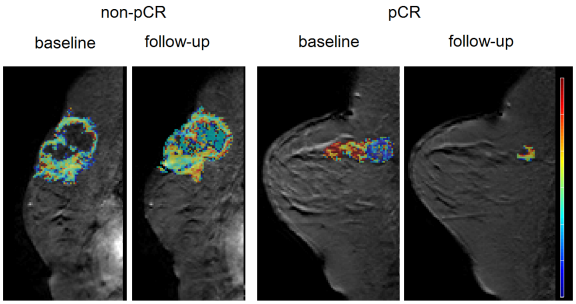

Figure 47: The maps of the hypoxic percentage contribution, a model-free prediction significant biomarker, from a non-pCR patient and a pCR patient for the baseline (first and third column) and follow-up (second and fourth column) studies.

and v_e PK biomarkers showed good predictive performance on the first follow-up using ensemble adaboost with decision trees of level one and extreme gradient boosting linear classifiers respectively. **It is worth mentioning that the hypoxic component (threshold 2) was found to be the best pCR predictor in three different classifiers at the first follow-up study showing consistent accuracy results.** The extreme gradient boosting linear classifier gave the best results of hypoxic threshold 2 component, with AUC 90.4%, F1 88.5%, sensitivity 74.0% and specificity 90.5%. Hypoxic component showed also high predictive ability on threshold 1, which further confirms the robustness of this biomarker in predicting treatment outcome without being biased from the thresholding procedure. What is more, the only statistical significant percentage change measure was the Δhypoxic thr2 with AUC 76.8% when using the ensemble adaboost with decision trees of level one classifier. The other two classifiers used in the statistical analysis, i.e. support vector machine with linear kernel and k-nearest neighbor classifiers represented by the two last rows in Table 7 gave results with sensitivity lower than 50% so they were not considered as giving significant predictive results.

As a last step of the statistical analysis, multivariate analysis was performed yet no combination of the model-free and model-based biomark-

Table 7: Model-free and model-based statistical analysis results for breast cancer dataset. Classifiers' acronyms: clf1 stands for ensemble adaboost with decision trees of level one, clf2 for extreme gradient boosting linear, clf3 for support vector machine with linear kernel, clf4 for random forest, and clf5 for k-nearest neighbor.

Classifier	Biomarker	AUC % (mean±s.d.)	F1 % (mean±s.d.)	Sensitivity % (mean±s.d.)	Specificity % (mean±s.d.)
clf2	hypoxic thr2	90.4±15.1	88.5±14.9	74.0±41.9	90.5±15.1
clf4	hypoxic thr2	88.6±14.7	81.5±15.4	82.0±33.1	82.5±20.4
clf1	hypoxic thr2	86.8±16.2	74.4±16.2	63.0±37.5	86.0±21.5
clf1	hypoxic thr1	73.4±17.3	60.3±16.2	67.0±35.9	62.5±22.2
clf1	Δhypoxic thr2	76.8±17.0	65.3±17.3	75.0±29.0	67.5±26.8
clf1	k_{ep} median	73.4±18.0	64.5±17.1	68.0±36.1	68.5±23.6
clf2	k_{ep} median	67.3±17.3	61.3±18.0	50.0±39.1	73.5±21.7
clf2	v_e median	72.6±20.2	71.0±19.4	67.0±31.3	84.0±18.7
clf1	v_e mean	69.9±19.6	62.1±16.3	63.0±28.2	73.0±25.7
clf2	v_e mean	69.6±20.0	65.4±17.6	61.0±27.3	83.0±19.8
clf1	v_e 80^{th} %ile	69.4±17.8	65.0±16.5	56.0±34.5	79.5±20.0
clf1	v_e median	68.4±20.3	68.5±19.5	68.0±29.9	80.0±21.4
clf1	v_e 90^{th} %ile	67.8±16.5	57.5±19.1	58.0±32.5	66.0±24.6
clf3	v_e 80^{th} %ile	85.0±15.6	62.3±16.6	11.0±23.2	96.0±10.5
clf5	hypoxic thr2	80.0±16.6	73.5±19.3	48.0±39.1	89.5±19.6

ers resulted in better prediction outcome at follow-up with respect to the univariate analysis. The best result from multivariate analysis, was obtained by combining recursively all statistically significant classifiers except mean and 80^{th} percentile of v_e at first follow-up, using extreme gradient boosting linear classifier (AUC 77.8).

To summarize, results of our predictive analysis revealed the ability of two model-free (hypoxic and Δhypoxic) and two model-based (k_{ep} and v_e) biomarkers to predict therapy response and discriminate successfully responders from non-responders with the DCE-MRI image-derived hypoxic component of the model-free approach outperforming all other IBs exhibiting an AUC 90.4% in predicting pCR patients in the first follow-up examination.

Chapter 5

Conclusions and Future Work

In this thesis, we investigated the potential of a model-free approach to describe the heterogeneous perfusion components of the cancer environment by applying PR techniques directly on DCE-MRI data. Describing the perfusion heterogeneity of a tumor in a non-invasive way is of utmost importance since it can play a key role in tumor characterization and lead to more effective treatment planning. Our main research goal was to build a reliable and efficient algorithmic tool for extracting pathophysiological parameters that is neither protocol nor tumor dependent. The objective of the proposed algorithm was to be able to provide clinically meaningful physiological properties of tumor for clinical decision support. More specifically, the identification of chemo/radio-resistant hypoxic areas in the tumor was the ultimate goal of this thesis since it is among the hallmarks of cancer and can affect significantly drug delivery leading to ineffective therapeutic regimens.

In order to approach the problem of tumor segmentation, we used an extension of the NMF algorithm and more specifically the BU-NMF, a fast matrix factorization algorithm suitable for non-negative data. Adjacent pixels in images often contain similar information thus dimensionality reduction algorithms, such as the BU-NMF, are used in order to

speed up image processing by using part and not the whole information contained in the image. The algorithm was applied directly on DCE-MRI data obtained from patients affected by sarcoma and breast cancer. Two novel initialization methods were introduced, the wash-in and PK initialization, in order to increase robustness and reproducibility of the algorithm.

Regarding the sarcoma dataset, six sarcoma cases have been studied in total including four liposarcomas (two pleomorphic, one dedifferentiated and one myxoid), and two MPNST cases. In Case studies I, III and IV additional results were obtained by implementation of the quantitative pharmacokinetic ETM model as well as by histopathological qualitative information provided by experienced histopathologists. In the third case study, DW-MRI and T2*r data were also used in order to provide complementary information to DCE-MRI. The main aim for the sarcoma dataset was to characterize the heterogeneous environment of the sarcomas using model-free methods while for each sarcoma case study, there was also a more specific clinical question, and these are explained in the following paragraphs. In all four case studies, the three most common theoretically expected types of DCE tissue curve shapes, i.e. Types 1, 2 and 3, were present in the results of the BU-NMF algorithm as being the dominant patterns that represent the signal and were associated with necrotic, hypoxic and well-perfused areas in the tumor respectively. In two of the patients though (Patient #4 and Patient #6) only two of the three aforementioned patterns were identified which was in accordance with the histopathological findings for these patients.

In Case study I, in addition to the automatic characterization of the tumor environment in the three sarcomas, the robustness of the two novel methods used for the initialization of the BU-NMF algorithm was also examined. It was shown that the well-perfused, hypoxic and necrotic components extracted from the two BU-NMF implementations (wash-in and PK initialized), correlated well between them while there was also a positive correlation with the same components extracted from the k^{trans} map with a simple k-means clustering. Small positive correlations were observed when comparing the k^{trans} image with the hypoxic component

of BU-NMF. The correlations were significantly improved, i.e. improvement of 41% for wash-in and 48% for PK initialization, when only a constrained (via double thresholding) part of the k^{trans} map was compared against the hypoxic BU-NMF image. What is more, from the double thresholding technique we used on the k^{trans} image, the BU-NMF hypoxic regions best correlated to k^{trans} image with values between 0.15 and 0.76 approximately, well-perfused areas to k^{trans} above 0.76 and necrotic regions to k^{trans} below 0.15. These results are in agreement with published results and findings on tumor hypoxia (SCW^{+}09; NTC^{+}13) as explained in Section 4.2.1. The histopathological findings indicated the presence of necrotic and well-perfused areas in all three lesions, however the detection of hypoxic regions would need further analysis since we only obtained immunohistochemistry results for one of the three patients.

In Case study II, the main goal was to assess perfusion differences in the same type of tumor (MPNST) based on PR. The BU-NMF algorithm was initialized by the k^{trans} map and resulted in identifying three different patterns in Patient #1 and two in Patient #4, which was due to the lack of necrotic regions in Patient #4. A second step of classification was implemented after the BU-NMF in order to assign to each pixel a single component since the BU-NMF assigns a mixture of all the identified components to each image pixel. Experiments with different classification thresholds were made and the percentages of well-perfused, hypoxic and necrotic pixels were computed for each threshold showing that the higher the threshold, the fewer were the pixels that were identified as purely well-perfused, necrotic or hypoxic.

In Case study III, we aimed to assess the follow-up of a liposarcoma patient by examining perfusion changes after therapy though different MRI modalities. It was shown that mean value shifts in all biomarkers (k^{trans}, f, T2*) stemming from different methods (DCE-MRI, DW-MRI, T2*r respectively) are in accordance with the change of the characteristic dominant perfusion curve of the tumor volume supporting the hypothesis of response to therapy. All metrics composed a complete multifaceted analysis that is in line with the radiological interpretation. BU-

NMF has successfully identified the three expected theoretical curves with the dominant pattern being hypoxia before therapy while after therapy necrosis prevailed.

Concerning Case study IV, we compared some preliminary histopathological results with DCE-MRI findings. In particular, images from H&E staining as well as from the HIF-1α factor have shown the presence two different perfusion profiles, the well-differentiated and the necrotic one. The BU-NMF algorithm has also produced similar results since it identified two different patterns, the necrotic pattern that was dominant and the well-perfused pattern that had smaller contribution.

For the breast cancer dataset, DCE-MRI data from a public available dataset, consisting of 35 breast cancer patients undergoing NAC, were analysed in order to investigate the role of model-free IBs in predicting the treatment outcome as early as possible. BU-NMF was utilized for the extraction of model-free biomarkers, which were the hypoxic, well-perfused and necrotic percentages of pixels that were identified as having the respective curve pattern. What is more, the three dominant patterns of the DCE time intensity signal curves were identified in the examined patients. Quantitative parameters were also calculated from ETM pharmacokinetic analysis. Statistical results indicated that DCE model-free biomarkers can discriminate responders from non-responders after the first cycle of NAC with a high percentage of accuracy (AUC 90.4%, F1 score 88.5%, Sensitivity 74%, Specificity 90.5%). In addition, three more DCE biomarkers were found to predict therapy outcome after the first cycle of NAC, i.e. Δhypoxic (AUC 76.8%), k_{ep} (AUC 73.4%) and v_e (AUC 72.6%).

The PR method used in our experiments has a number of advantages. First of all, it gave fast (around 25s execution time on an Intel Core 2 i7-4770 processor, 3.4 GHz with 16 GB RAM) when ran on a Matlab compiler (version 8.1.0.604 R2013a). The two novel BU-NMF initialization schemes were proven to have repeatable results, always converging after a precise number of iterations for each patient. In addition, the results obtained did not depend on complex fitting or initialization procedures in contrast to computationally expensive PK models, which require non-

linear fitting schemes that may lead to local extrema problems. In our method, the user is in charge only of the tumor ROI selection, whereas for PK models there is need to select certain parameters in advance such as the AIF (ED09) which is subjective and prone to error. Last but not least, in contrast to model-based approaches, our method does not make any assumptions on the underlying biology since it is purely data-driven.

Regarding the sarcoma dataset, in all six sarcoma patients the BU-NMF algorithm identified the dominant perfusion patterns characterizing the tumor environment and these were in line with the theoretical enhancement patterns. Furthermore, the robustness of the two presented initialization methods was demonstrated in Case study I, giving very similar results for both initialization schemes (see Section 4.2). In Case study II, different number of patterns were identified in two patients with MPNST which is encouraging for possible determination of the grade of tumor malignancy using model-free, non-invasive techniques in patients with the same tumor type. In Case study III, results from three non-invasive MRI methods on a liposarcoma after ILP with TNF-α identified similar perfusion changes confirming response to therapy. These results are promising since MRI analysis of TNF induced perfusion has only been studied in animals (PWTH$^+$04). The limited histopathological results that were available in Case studies I, III and IV were very positive in the sense that they gave comparable results to the BU-NMF method. More specifically, necrotic areas that showed no signal enhancement in DCE-MRI and were characterized with the BU-NMF necrotic pattern were also confirmed through H&E staining of tissue sections. In addition, in Case study IV the hypoxia factor HIF-1α confirmed the presence of both well-differentiated and necrotic areas, which were in accordance with the BU-NMF and the pharmacokinetic DCE-MRI results. NMF has also been applied for the segmentation of rat prostate cancer DCE data (SHS$^+$12) and results have been compared to histopathology findings. However, in our study we used an improved BU-NMF algorithm using two novel, data-driven initialization methods. Moreover, herein the algorithm was used on human patient data whereas previous works (HAS$^+$13; SHS$^+$12) were performed on pre-clinical studies with

limited number of data.

Concerning the breast cancer dataset, this paper presents a novel approach proposing the use of PR defined tumor environment (hypoxic, well-perfused and necrotic) image clusters for predicting NAC response. The presented BU-NMF framework systematically classified tumor DCE-MRI image pixels into regions with enhancement profiles matching those of the actual tumor environment. Previous studies exploited the concept of segmenting part of the tumor to increase predictive power. In (KKM$^+$15), the segmentation of the tumor regions of interest based on a vascular heterogeneity measure further enhanced the predictive power of model-based IBs in a glioblastoma multiforme study whereas in (WGCL16), an image clustering method followed by texture analysis increased pCR prediction in a breast cancer patient cohort. However, both approaches failed to demonstrate the physiological meaning of the more predictive image cluster on the basis of theoretically expected DCE-MRI enhancement profiles.

To strengthen the value of our results in the breast cancer study, we also considered well-known compartmental-based IBs but the PR derived hypoxic component outperformed all others within the thorough statistical analysis methodology presented. Although it is very hard to validate any DCE-MRI image-driven measure of hypoxia, the results support the hypothesis that the NMF-based hypoxic image component is related to the actual hypoxic part of the tumor. The strong predictive power of this component is an indicator in favor of this assumption for two reasons: first, hypoxia has been reported as predictor of response in NAC (GBB$^+$06; URC$^+$12) and secondly, the morphology of the delayed enhancement curve of the hypoxic component as depicted in Figure 45, is in agreement with 18F-Fmiso PET studies reporting that hypoxic regions enhance at later times after injection demonstrating lower initial activity than well-perfused areas but are more persistent through time (CAC$^+$09).

Our results also compare favorably to previous DCE-MRI studies with promising results (WGCL16; ALH$^+$13; LAA$^+$14) in the same dataset regarding prediction of breast cancer treatment outcome using quantitative

and semi-quantitative DCE measures. However, the obtained results of the aforementioned studies were obtained only from a subset of the original dataset. In particular, in (ALH$^+$13) 21 breast cancer patients were examined using solely semi-quantitative measures whereas in (LAA$^+$14) 28 breast patients were analysed using both semi-quantitative and quantitative DCE measures. In both these studies, certain thresholds also were applied in order to exclude non-enhancing and slow enhancing pixels, which could lead to erroneous results, as the slow-enhancing pixels (necrotic) can provide valuable information. Another strength of our study compared to previous ones, is the fact that the predictive ability of the biomarkers was computed using more robust statistical univariate and multivariate techniques. In (WGCL16), PCA and k-means clustering methods have been used in combination with texture analysis to predict pCR in 35 patients of the breast cancer dataset. However, PCA lacks in physical interpretation compared to NMF, which was demonstrated to be more pertinent to parts-based representations (LS99) due to its non-negativity constraints. Because of this, their results were not directly associated with description of the tumor environment and with the theoretically defined DCE-MRI enhancement profiles.

An obvious limitation of the current work is further validation against a larger patient cohort as well correlation to histopathology and immunohistochemistry results, which was only available for a limited number of sarcoma patients. It is important to stress that the current work focused mainly on the PR method and more specifically on demonstrating the increased stability and invariance to initial conditions and on correlating the automatically extracted regions to the theoretically expected curves and to the well-known k^{trans} variable. Interestingly, our results show that by constraining the k^{trans} parametrized image within a double threshold (lower to exclude necrosis and upper to exclude well-perfused areas), the correlation to our extracted hypoxic components increases significantly. This is an encouraging indication that our data-based approach is able to produce clinically significant results related to tumor hypoxia, a hypothesis that needs further investigation in order to be confirmed.

The work on the breast cancer dataset has also a few limitations, which are mainly linked to the publicly available dataset. Firstly, there wass diversity in the specific therapeutic regimens followed for each patient. In addition, the cohort was of relatively small size (35) with 23 non-pCR and only 12 pCR patients, which calls for similar follow-up studies with larger patient cohorts in the future. Finally, the DCE dataset was characterized by low temporal resolution (16 s) which can affect the measurement of the dynamic enhancement at the early enhancement time. That said, all these are limitations inherent to the dataset and have been pointed out in the previous studies (LAA$^+$15; LAA$^+$14).

5.1 Future work

Future research activities will aim at implementing the BU-NMF algorithm on more case studies and different types of cancer. Another possible research direction is to apply different PR techniques and compare the results with those stemming from the BU-NMF algorithm. An ultimate goal would be to establish model-free biomarkers, such as the hypoxic one, as reliable prognostic cancer indicators or as predictors of response to therapy as it was shown in Case study V.

More specifically for the sarcoma dataset, we are already in the process of collecting new data from sarcoma patients who have been subject to surgery and their excised histologic tissue sections have been elaborated by histopathologists in order to extract quantitative biomarkers. The main plan for future work is to compare our computational results from the model-free and model-based approach with quantitative histopathological parameters. All the tissue sections analyzed computationally, will be histopathologically examined for morphological features, while additional immunohistochemistry will identify biomarkers such as HIF-1α, which will be afterwards translated to hypoxia and other related cancer hallmarks.

What is more, further work and analysis on a large series of tumor image data and of different tumor types will be performed in order to confirm our results and investigate the correlations between model-based,

model-free methods and histopathology in the same or different tumor malignancies. Benign soft tissue tumors will also be studied in order to compare their perfusion characteristics against those of the malignant tumors.

As for the breast cancer dataset, since tumor hypoxia is indeed a predictor of NAC response the next step is also to propose further validation regarding the correlation of the DCE-MRI image-derived hypoxic component to the underlying molecular/genetic characteristics of hypoxia such as the HIFs transcription factors that respond to decreases in available oxygen in the cellular environment.

To summarize, results from the five examined case studies indicate that it is possible to assess tumor hypoxia noninvasively using only DCE-MRI data together with some post-processing computational methods. The overall results suggest that PR image segmentation methods can be a more robust (model-free) and purely data-driven (independent from imaging parameters) alternative to model-based IBs, which also require subjective interaction steps (e.g. AIF calculation). Although, more sophisticated techniques such as PET imaging with hypoxia tracers can provide more quantitative/specific hypoxia information, extracting tumor hypoxia information directly from DCE-MRI has the potential to offer significant clinical benefits since it is a widely-used, cost-effective technique in cancer diagnosis and management. In this sense, the work presented in this thesis may also contribute to the growing field of radiogenomics in cancer aiming to maximize the tumor information derived from medical images and provide early markers of hypoxia or other cancer hallmarks. This in turn will allow more precise clinical management decisions for patients at earlier stages, while being non-invasive and associated with minimal patient discomfort. Achieving hypoxic image area delineation as well as characterization of the diverse perfusion areas present in heterogeneous tumors, will be also useful in guiding core needle biopsy so that it targets the most representative areas of the tumor. In addition, this method could help in tumor differentiation based on the extracted MRI perfusion maps improving in this way the surgical decision making. Finally, the comparison of the PR classification results

for tumors of the same type could be an indicator of the tumor grading at the MRI stage and before surgery. Tumor grading is decided based on the morphology of tumor cells when examined under the microscope. In Case study II, we saw that two MPNST patients diagnosed with different morphology characteristics, they also had a different number of patterns identified by the BU-NMF method. To this end, by testing more cases of the same cancer type, we could classify the tumors in low, average or high grade based on the perfusion classification patterns extracted by the BU-NMF.

References

[ALH+13] R. G. Abramson, X. Li, T. L. Hoyt, P. F. Su, L. R. Arlinghaus, K. J. Wilson, V. G. Abramson, A. B. Chakravarthy, and T. E. Yankeelov. Early assessment of breast cancer response to neoadjuvant chemotherapy by semi-quantitative analysis of high-temporal resolution DCE-MRI: preliminary results. *Magn Reson Imaging*, 31(9):1457–64, 2013. 89, 90

[Atl09] S. W. Atlas. *Magnetic resonance imaging of the brain and spine*, volume 1. Lippincott Williams & Wilkins, 2009. 14

[BBL+07] M. W. Berry, M. Browne, A. N. Langville, V. P. Pauca, and R. J. Plemmons. Algorithms and applications for approximate nonnegative matrix factorization. *Computational Statistics & Data Analysis*, 52(1):155–173, 2007. 30, 31

[BEJ+99] J. O. Barentsz, M. Engelbrecht, G. J. Jager, J. A. Witjes, J. de LaRosette, B. P. van Der Sanden, H. J. Huisman, and A. Heerschap. Fast dynamic gadolinium-enhanced MR imaging of urinary bladder and prostate cancer. *J Magn Reson Imaging*, 10(3):295–304, 1999. 7

[BG08] C. Boutsidis and E. Gallopoulos. SVD based initialization: A head start for nonnegative matrix factorization. *Pattern Recognition*, 41(4):1350–1362, 2008. 38

[BNS+10] Y. Baba, K. Nosho, K. Shima, N. Irahara, A. T. Chan, J. A. Meyerhardt, D. C. Chung, E. L. Giovannucci, C. S. Fuchs, and S. Ogino. HIF1A overexpression is associated with poor prognosis in a cohort of 731 colorectal cancers. *Am J Pathol*, 176(5):2292–301, 2010. 3

[BOM+09] C. Balleyguier, P. Opolon, M. C. Mathieu, A. Athanasiou, J. R. Garbay, S. Delaloge, and C. Dromain. New potential and appli-

cations of contrast-enhanced ultrasound of the breast: Own investigations and review of the literature. *Eur J Radiol*, 69(1):14–23, 2009. 6

[BSO+00] P. Birner, M. Schindl, A. Obermair, C. Plank, G. Breitenecker, and G. Oberhuber. Overexpression of hypoxia-inducible factor 1alpha is a marker for an unfavorable prognosis in early-stage invasive cervical cancer. *Cancer Res*, 60(17):4693–6, 2000. 3

[BSP+91] G. Brix, W. Semmler, R. Port, L. R. Schad, G. Layer, and W. J. Lorenz. Pharmacokinetic parameters in CNS Gd-DTPA enhanced MR imaging. *J Comput Assist Tomogr*, 15(4):621–8, 1991. 19

[BSRZ+12] G. Brix, M. Salehi Ravesh, S. Zwick, J. Griebel, and S. Delorme. On impulse response functions computed from dynamic contrast-enhanced image data by algebraic deconvolution and compartmental modeling. *Phys Med*, 28(2):119–28, 2012. 19

[CAC+09] H. Cho, E. Ackerstaff, S. Carlin, M. E. Lupu, Y. Wang, A. Rizwan, J. O'Donoghue, C. C. Ling, J. L. Humm, P. B. Zanzonico, and J. A. Koutcher. Noninvasive multimodality imaging of the tumor microenvironment: registered dynamic magnetic resonance imaging and positron emission tomography studies of a preclinical tumor model of tumor hypoxia. *Neoplasia*, 11(3):247–59, 2p following 259, 2009. 6, 26, 66, 89

[CAT+17] Y. C. Chang, E. Ackerstaff, Y. Tschudi, B. Jimenez, W. Foltz, C. Fisher, L. Lilge, H. Cho, S. Carlin, R. J. Gillies, Y. Balagurunathan, R. L. Yechieli, T. Subhawong, B. Turkbey, A. Pollack, and R. Stoyanova. Delineation of Tumor Habitats based on Dynamic Contrast Enhanced MRI. *Sci Rep*, 7(1):9746, 2017. 7, 23, 26, 45, 46

[CCL+00] R. A. Cooper, B. M. Carrington, J. A. Loncaster, S. M. Todd, S. E. Davidson, J. P. Logue, A. D. Luthra, A. P. Jones, I. Stratford, R. D. Hunter, and C. M. West. Tumour oxygenation levels correlate with dynamic contrast-enhanced magnetic resonance imaging parameters in carcinoma of the cervix. *Radiother Oncol*, 57(1):53–9, 2000. 7

[Cha43] H. W. Chalkley. Method for the quantitative morphologic analysis of tissues. *Journal of the National Cancer Institute*, 4(1):47–53, 1943. 71

[CJ00] P. Carmeliet and R. K. Jain. Angiogenesis in cancer and other diseases. *Nature*, 407(6801):249–57, 2000. 2

[CVS+13] K. Clark, B. Vendt, K. Smith, J. Freymann, J. Kirby, P. Koppel, S. Moore, S. Phillips, D. Maffitt, M. Pringle, L. Tarbox, and F. Prior. The Cancer Imaging Archive (tcia): maintaining and operating a public information repository. *J Digit Imaging*, 26(6):1045–57, 2013. 77

[DFHM15] N. Dhani, A. Fyles, D. Hedley, and M. Milosevic. The clinical significance of hypoxia in human cancers. *Semin Nucl Med*, 45(2):110–21, 2015. 4

[dWtHdB+00] J. H. de Wilt, T. L. ten Hagen, G. de Boeck, S. T. van Tiel, E. A. de Bruijn, and A. M. Eggermont. Tumour necrosis factor alpha increases melphalan concentration in tumour tissue after isolated limb perfusion. *Br J Cancer*, 82(5):1000–3, 2000. 70

[EBR+10] E. Eyal, B. N. Bloch, N. M. Rofsky, E. Furman-Haran, E. M. Genega, R. E. Lenkinski, and H. Degani. Principal component analysis of dynamic contrast enhanced MRI in human prostate cancer. *Invest Radiol*, 45(4):174–81, 2010. 23

[ED09] E. Eyal and H. Degani. Model-based and model-free parametric analysis of breast dynamic-contrast-enhanced MRI. *NMR Biomed*, 22(1):40–53, 2009. 24, 88

[EHL+03] M. R. Engelbrecht, H. J. Huisman, R. J. Laheij, G. J. Jager, G. J. van Leenders, C. A. Hulsbergen-Van De Kaa, J. J. de la Rosette, J. G. Blickman, and J. O. Barentsz. Discrimination of prostate cancer from normal peripheral zone and central gland tissue by using dynamic contrast-enhanced MR imaging. *Radiology*, 229(1):248–54, 2003. 20

[FASW93] F. W. Flickinger, J. D. Allison, R. M. Sherry, and J. C. Wright. Differentiation of benign from malignant breast masses by time-intensity evaluation of contrast enhanced MRI. *Magn Reson Imaging*, 11(5):617–20, 1993. 21

[Fed17] C. Federau. Intravoxel incoherent motion MRI as a means to measure in vivo perfusion: A review of the evidence. *NMR Biomed*, 30(11), 2017. 70

[FHGKD01] E. Furman-Haran, D. Grobgeld, F. Kelcz, and H. Degani. Critical role of spatial resolution in dynamic contrast-enhanced breast MRI. *J Magn Reson Imaging*, 13(6):862–7, 2001. 20

[FJ07] D. Fukumura and R. K. Jain. Tumor microenvironment abnormalities: causes, consequences, and strategies to normalize. *J Cell Biochem*, 101(4):937–49, 2007. 3

[FJM+16] S. M. Fisher, R. Joodi, A. J. Madhuranthakam, O. K. Öz, R. Sharma, and A. Chhabra. Current utilities of imaging in grading musculoskeletal soft tissue sarcomas. *Eur J Radiol*, 85(7):1336–44, 2016. 7

[FSD+15] J. Ferlay, I. Soerjomataram, R. Dikshit, S. Eser, C. Mathers, M. Rebelo, D. M. Parkin, D. Forman, and F. Bray. Cancer incidence and mortality worldwide: sources, methods and major patterns in GLOBOCAN 2012. *Int J Cancer*, 136(5):E359–86, 2015. 77

[GBB+06] D. Generali, A. Berruti, M. P. Brizzi, L. Campo, S. Bonardi, S. Wigfield, A. Bersiga, G. Allevi, M. Milani, S. Aguggini, V. Gandolfi, L. Dogliotti, A. Bottini, A. L. Harris, and S. B. Fox. Hypoxia-inducible factor-1alpha expression predicts a poor response to primary chemoendocrine therapy and disease-free survival in primary human breast cancer. *Clin Cancer Res*, 12(15):4562–8, 2006. 89

[GLL+04] P. Gibbs, G. P. Liney, M. Lowry, P. J. Kneeshaw, and L. W. Turnbull. Differentiation of benign and malignant sub-1 cm breast lesions using dynamic contrast enhanced MRI. *Breast*, 13(2):115–21, 2004. 21

[HAS+13] S. H. Han, E. Ackerstaff, R. Stoyanova, S. Carlin, W. Huang, J. A. Koutcher, J. K. Kim, G. Cho, G. Jang, and H. Cho. Gaussian mixture model-based classification of dynamic contrast enhanced MRI data for identifying diverse tumor microenvironments: preliminary results. *NMR Biomed*, 26(5):519–32, 2013. 8, 9, 26, 27, 88

[HBK+95] U. Hoffmann, G. Brix, M. V. Knopp, T. Hess, and W. J. Lorenz. Pharmacokinetic mapping of the breast: a new method for dynamic MR mammography. *Magn Reson Med*, 33(4):506–14, 1995. 19, 26

[HKJ+15] N. F. Haq, P. Kozlowski, E. C. Jones, S. D. Chang, S. L. Goldenberg, and M. Moradi. A data-driven approach to prostate cancer detection from dynamic contrast enhanced MRI. *Comput Med Imaging Graph*, 41:37–45, 2015. 25

[HM04] M. A. Horsfield and B. Morgan. Algorithms for calculation of kinetic parameters from T1-weighted dynamic contrast-enhanced magnetic resonance imaging. *J Magn Reson Imaging*, 20(4):723–9, 2004. 20

[HRL98] E. Henderson, B. K. Rutt, and T. Y. Lee. Temporal sampling requirements for the tracer kinetics modeling of breast disease. *Magn Reson Imaging*, 16(9):1057–73, 1998. 20

[HRM+01] F. A. Howe, S. P. Robinson, D. J. McIntyre, M. Stubbs, and J. R. Griffiths. Issues in flow and oxygenation dependent contrast (FLOOD) imaging of tumours. *NMR Biomed*, 14(7-8):497–506, 2001. 70

[HSM+96] M. Höckel, K. Schlenger, M. Mitze, U. Schäffer, and P. Vaupel. Hypoxia and Radiation Response in Human Tumors. *Semin Radiat Oncol*, 6(1):3–9, 1996. 4

[HTG+94] B. Hamm, R. F. Thoeni, R. G. Gould, M. E. Bernardino, M. L¨ning, S. Saini, A. E. Mahfouz, M. Taupitz, and K. J. Wolf. Focal liver lesions: characterization with nonenhanced and dynamic contrast material-enhanced MR imaging. *Radiology*, 190(2):417–23, 1994. 7

[Jac04] A. Jackson. Analysis of dynamic contrast enhanced MRI. *Br J Radiol*, 77 Spec No 2:S154–66, 2004. 14

[JG96] J. Jahr and P. O. Grände. In vivo effects of tumor necrosis factor-alpha on capillary permeability and vascular tone in a skeletal muscle. *Acta Anaesthesiol Scand*, 40(2):256–61, 1996. 69

[JH16] J. Jakob and P. Hohenberger. Role of isolated limb perfusion with recombinant human tumor necrosis factor α and melphalan in locally advanced extremity soft tissue sarcoma. *Cancer*, 122(17):2624–32, 2016. 69

[JMG+14] R. L. Jensen, M. L. Mumert, D. L. Gillespie, A. Y. Kinney, M. C. Schabel, and K. L. Salzman. Preoperative dynamic contrast-enhanced MRI correlates with molecular markers of hypoxia and vascularity in specific areas of intratumoral microenvironment and is predictive of patient outcome. *Neuro Oncol*, 16(2):280–91, 2014. 3

[JPM+05] G. C. Jayson, G. J. Parker, S. Mullamitha, J. W. Valle, M. Saunders, L. Broughton, J. Lawrance, B. Carrington, C. Roberts, B. Issa, D. L. Buckley, S. Cheung, K. Davies, Y. Watson, K. Zinkewich-Péotti, L. Rolfe, and A. Jackson. Blockade of platelet-derived growth factor receptor-beta by CDP860, a humanized, PEGylated di-Fab', leads to fluid accumulation and is associated with increased tumor vascularized volume. *J Clin Oncol*, 23(5):973–81, 2005. 14

[KBB+07] O. Kubassova, M. Boesen, R. D. Boyle, M. A. Cimmino, K. E. Jensen, H. Bliddal, and A. Radjenovic. Fast and robust analysis of dynamic contrast enhanced MRI datasets. *Med Image Comput Comput Assist Interv*, 10(Pt 2):261–9, 2007. 22

[KBCB10] O. Kubassova, M. Boesen, M. A. Cimmino, and H. Bliddal. A computer-aided detection system for rheumatoid arthritis MRI data interpretation and quantification of synovial activity. *Eur J Radiol*, 74(3):e67–72, 2010. 22

[KCG+07] G. Korpanty, J. G. Carbon, P. A. Grayburn, J. B. Fleming, and R. A. Brekken. Monitoring response to anticancer therapy by targeting microbubbles to tumor vasculature. *Clin Cancer Res*, 13(1):323–30, 2007. 6

[KCK+08] M. C. Kale, B. D. Clymer, R. M. Koch, J. T. Heverhagen, S. Sammet, R. Stevens, and M. V. Knopp. Multispectral co-occurrence with three random variables in dynamic contrast enhanced magnetic resonance imaging of breast cancer. *IEEE Trans Med Imaging*, 27(10):1425–31, 2008. 24

[Ket51] S. S. Kety. The theory and applications of the exchange of inert gas at the lungs and tissues. *Pharmacol Rev*, 3(1):1–41, 1951. 16

[KGS+02] M. I. Koukourakis, A. Giatromanolaki, E. Sivridis, C. Simopoulos, H. Turley, K. Talks, K. C. Gatter, and A. L. Harris. Hypoxia-inducible factor (HIF1A and HIF2A), angiogenesis, and chemoradiotherapy outcome of squamous cell head-and-neck cancer. *Int J Radiat Oncol Biol Phys*, 53(5):1192–202, 2002. 3

[KHC+05] J. K. Kim, S. S. Hong, Y. J. Choi, S. H. Park, H. Ahn, C. S. Kim, and K. S. Cho. Wash-in rate on the basis of dynamic contrast-enhanced MRI: usefulness for prostate cancer detection and localization. *J Magn Reson Imaging*, 22(5):639–46, 2005. 20

[KKM+15] E. Kontopodis, G. Kanli, G. C. Manikis, S. Van Cauter, and K. Marias. Assessing Treatment Response Through Generalized Pharmacokinetic Modeling of DCE-MRI Data. *Cancer Inform*, 14(Suppl 4):41–51, 2015. 7, 25, 89

[KKS+16] E. Kontopodis, I. Karatzanis, V. Sakkalis, F. Buffa, and K. Marias. A DCE analysis workflow. In *CGI'16 - 33rd Computer Graphics International,*, pages 101–104. ACM New York, 2016. 55, 71, 80

[KMK+99] C. K. Kuhl, P. Mielcareck, S. Klaschik, C. Leutner, E. Wardelmann, J. Gieseke, and H. H. Schild. Dynamic breast MR imaging: are

signal intensity time course data useful for differential diagnosis of enhancing lesions? *Radiology*, 211(1):101–10, 1999. 6, 65

[KP07] H. Kim and H. Park. Sparse non-negative matrix factorizations via alternating non-negativity-constrained least squares for microarray data analysis. *Bioinformatics*, 23(12):1495–502, 2007. 32

[KRE+92] W. J. Koh, J. S. Rasey, M. L. Evans, J. R. Grierson, T. K. Lewellen, M. M. Graham, K. A. Krohn, and T. W. Griffin. Imaging of hypoxia in human tumors with [F-18]fluoromisonidazole. *Int J Radiat Oncol Biol Phys*, 22(1):199–212, 1992. 5

[KSW+02] T. Kolenda, S. Sigurdsson, O. Winther, L. K. Hansen, and J. Larsen. DTU:Toolbox, 2002. Available at `http://isp.imm.dtu.dk/toolbox/`. 34

[KVM+on] E. Kontopodis, M. Venianaki, G. Manikis, K. Nikiforaki, O. Salvetti, E. Papadaki, G. Papadakis, A. Karantanas, and K. Marias. Investigating the role of model-based and model-free imaging biomarkers as early predictors of neoadjuvant breast cancer therapy outcome. *IEEE Journal of Biomedical and Health Informatics*, submitted for publication. xix, 50, 53

[KWS+99] M. V. Knopp, E. Weiss, H. P. Sinn, J. Mattern, H. Junkermann, J. Radeleff, A. Magener, G. Brix, S. Delorme, I. Zuna, and G. van Kaick. Pathophysiologic basis of contrast enhancement in breast tumors. *J Magn Reson Imaging*, 10(3):260–6, 1999. 7

[LAA+14] X. Li, L. R. Arlinghaus, G. D. Ayers, A. B. Chakravarthy, R. G. Abramson, V. G. Abramson, N. Atuegwu, J. Farley, I. A. Mayer, M. C. Kelley, I. M. Meszoely, J. Means-Powell, A. M. Grau, M. Sanders, S. R. Bhave, and T. E. Yankeelov. DCE-MRI analysis methods for predicting the response of breast cancer to neoadjuvant chemotherapy: pilot study findings. *Magn Reson Med*, 71(4):1592–602, 2014. 89, 90, 91

[LAA+15] X. Li, R. G. Abramson, L. R. Arlinghaus, H. Kang, A. B. Chakravarthy, V. G. Abramson, J. Farley, I. A. Mayer, M. C. Kelley, I. M. Meszoely, J. Means-Powell, A. M. Grau, M. Sanders, and T. E. Yankeelov. Multiparametric magnetic resonance imaging for predicting pathological response after the first cycle of neoadjuvant chemotherapy in breast cancer. *Invest Radiol*, 50(4):195–204, 2015. xiii, 55, 72, 77, 78, 91

[LAA+16] X. Li, R. G. Abramson, L. R. Arlinghaus, A. B. Chakravarthy, V. G. Abramson, M. Sanders, and T. E. Yankeelov. Data from QIN-Breast [Data set]. *The Cancer Imaging Archive*, 2016. Available at `http://doi.org/10.7937/K9/TCIA.2016.21JUebH0`. 52, 77

[LdJvdS+07] C. Lavini, M. C. de Jonge, M. G. van de Sande, P. P. Tak, A. J. Nederveen, and M. Maas. Pixel-by-pixel analysis of DCE MRI curve patterns and an illustration of its application to the imaging of the musculoskeletal system. *Magn Reson Imaging*, 25(5):604–12, 2007. 22

[LKB01] R. E. Lucht, M. V. Knopp, and G. Brix. Classification of signal-time curves from dynamic MR mammography by neural networks. *Magn Reson Imaging*, 19(1):51–7, 2001. 24

[LKL01] R. M. Locksley, N. Killeen, and M. J. Lenardo. The tnf and tnf receptor superfamilies: integrating mammalian biology. *Cell*, 104(4):487–501, 2001. 69

[LLC+08] J. Levman, T. Leung, P. Causer, D. Plewes, and A. L. Martel. Classification of dynamic contrast-enhanced magnetic resonance breast lesions by support vector machines. *IEEE Trans Med Imaging*, 27(5):688–96, 2008. 25

[LM08] C. Lavini and M. Maas. DCE-MRI analysis package comprising pixel-by-pixel classification of Time Intensity Curves shapes, permeability maps and Gd concentration calculation. *Magnetic Resonance Materials in Physics, Biology and Medicine*, 21:486, 2008. 22

[LMS+05] Z. P. Li, Q. F. Meng, C. H. Sun, D. S. Xu, M. Fan, X. F. Yang, and D. Y. Chen. Tumor angiogenesis and dynamic CT in colorectal carcinoma: radiologic-pathologic correlation. *World J Gastroenterol*, 11(9):1287–91, 2005. 5

[LMY+10] S. V. Liu, L. Melstrom, K. Yao, C. A. Russell, and S. F. Sener. Neoadjuvant therapy for breast cancer. *J Surg Oncol*, 101(4):283–91, 2010. 77

[LN13] Y. Li and A. Ngom. The non-negative matrix factorization toolbox for biological data mining. *Source Code Biol Med*, 8(1):10, 2013. 34

[LS99] D. D. Lee and H. S. Seung. Learning the parts of objects by non-negative matrix factorization. *Nature*, 401(6755):788–91, 1999. 27, 28, 90

[LS01] D. D. Lee and H. S. Seung. Algorithms for non-negative matrix factorization. In *Advances in neural information processing systems*, pages 556–562, 2001. 30

[LS07] S. T. Lee and A. M. Scott. Hypoxia positron emission tomography imaging with 18f-fluoromisonidazole. *Semin Nucl Med*, 37(6):451–61, 2007. 5

[LWS+15] L. Li, K. Wang, X. Sun, Y. Sun, G. Zhang, and B. Shen. Parameters of dynamic contrast-enhanced MRI as imaging markers for angiogenesis and proliferation in human breast cancer. *Med Sci Monit*, 21:376–82, 2015. 8

[MdAGB+15] J. R. Maltez de Almeida, A. B. Gomes, T. P. Barros, P. E. Fahel, and M. de Seixas Rocha. Subcategorization of Suspicious Breast Lesions (BI-RADS Category 4) According to MRI Criteria: Role of Dynamic Contrast-Enhanced and Diffusion-Weighted Imaging. *AJR Am J Roentgenol*, 205(1):222–31, 2015. 7

[MF05] C. Menon and D. L. Fraker. Tumor oxygenation status as a prognostic marker. *Cancer Lett*, 221(2):225–35, 2005. 4

[MLJ+08] S. H. Ma, H. B. Le, B. H. Jia, Z. X. Wang, Z. W. Xiao, X. L. Cheng, W. Mei, M. Wu, Z. G. Hu, and Y. G. Li. Peripheral pulmonary nodules: relationship between multi-slice spiral CT perfusion imaging and tumor angiogenesis and VEGF expression. *BMC Cancer*, 8:186, 2008. 5

[MNPM16] G. C. Manikis, K. Nikiforaki, N. Papanikolaou, and K. Marias. Diffusion Modelling Tool (DMT) for the analysis of Diffusion Weighted Imaging (DWI) Magnetic Resonance Imaging (MRI) data. In *CGI'16 - 33rd Computer Graphics International*, pages 97–100, 2949060, 2016. ACM. 71

[MSB+07] L. A. Meinel, A. H. Stolpen, K. S. Berbaum, L. L. Fajardo, and J. M. Reinhardt. Breast MRI lesion classification: improved performance of human readers with a backpropagation neural network computer-aided diagnosis (CAD) system. *J Magn Reson Imaging*, 25(1):89–95, 2007. 25

[MSB+11] C. A. Maftei, K. Shi, C. Bayer, S. T. Astner, and P. Vaupel. Comparison of (immuno-)fluorescence data with serial [18F]Fmiso PET/CT imaging for assessment of chronic and acute hypoxia in head and neck cancers. *Radiother Oncol*, 99(3):412–7, 2011. 6

[MTD+03] B. Morgan, A. L. Thomas, J. Drevs, J. Hennig, M. Buchert, A. Jivan, M. A. Horsfield, K. Mross, H. A. Ball, L. Lee, W. Mietlowski, S. Fuxuis, C. Unger, K. O'Byrne, A. Henry, G. R. Cherryman, D. Laurent, M. Dugan, D. Marmé, and W. P. Steward. Dynamic contrast-enhanced magnetic resonance imaging as a biomarker for the pharmacological response of PTK787/ZK 222584, an inhibitor of the vascular endothelial growth factor receptor tyrosine kinases, in patients with advanced colorectal cancer and liver metastases: results from two phase I studies. *J Clin Oncol*, 21(21):3955–64, 2003. 14

[NBR+05] M. Nordsmark, S. M. Bentzen, V. Rudat, D. Brizel, E. Lartigau, P. Stadler, A. Becker, M. Adam, M. Molls, J. Dunst, D. J. Terris, and J. Overgaard. Prognostic value of tumor oxygenation in 397 head and neck tumors after primary radiation therapy. An international multi-center study. *Radiother Oncol*, 77(1):18–24, 2005. 4

[NCCE+09] K. Newbold, I. Castellano, E. Charles-Edwards, D. Mears, A. Sohaib, M. Leach, P. Rhys-Evans, P. Clarke, C. Fisher, K. Harrington, and C. Nutting. An exploratory study into the role of dynamic contrast-enhanced magnetic resonance imaging or perfusion computed tomography for detection of intratumoral hypoxia in head-and-neck cancer. *Int J Radiat Oncol Biol Phys*, 74(1):29–37, 2009. 7

[NMV+18] K. Nikiforaki, G. C. Manikis, M. Venianaki, E. Kontopodis, E. Lagoudaki, T. G. Maris, K. Marias, E. de Bree, and A. Karantanas. Perfusion and oxygenation changes after Isolated Limb Perfusion with TNF - α in Lower Limb Sarcoma: A Case Report. *Biomedical Research and Reviews*, 1(1):101, 2018. xix, 53

[NTC+13] M. L. Neal, A. D. Trister, T. Cloke, R. Sodt, S. Ahn, A. L. Baldock, C. A. Bridge, A. Lai, T. F. Cloughesy, M. M. Mrugala, J. K. Rockhill, R. C. Rockne, and K. R. Swanson. Discriminating survival outcomes in patients with glioblastoma using a simulation-based, patient-specific response metric. *PLoS One*, 8(1):e51951, 2013. 61, 62, 86

[OAA+17] J. P. O'Connor, E. O. Aboagye, J. E. Adams, H. J. Aerts, S. F. Barrington, A. J. Beer, R. Boellaard, S. E. Bohndiek, M. Brady, G. Brown, D. L. Buckley, T. L. Chenevert, L. P. Clarke, S. Collette, G. J. Cook, N. M. deSouza, J. C. Dickson, C. Dive, J. L. Evelhoch, C. Faivre-Finn, F. A. Gallagher, F. J. Gilbert, R. J. Gillies, V. Goh, J. R. Griffiths, A. M. Groves, S. Halligan, A. L. Harris, D. J. Hawkes, O. S. Hoekstra, E. P. Huang, B. F. Hutton, E. F.

Jackson, G. C. Jayson, A. Jones, D. M. Koh, D. Lacombe, P. Lambin, N. Lassau, M. O. Leach, T. Y. Lee, E. L. Leen, J. S. Lewis, Y. Liu, M. F. Lythgoe, P. Manoharan, R. J. Maxwell, K. A. Miles, B. Morgan, S. Morris, T. Ng, A. R. Padhani, G. J. Parker, M. Partridge, A. P. Pathak, A. C. Peet, S. Punwani, A. R. Reynolds, S. P. Robinson, L. K. Shankar, R. A. Sharma, D. Soloviev, S. Stroobants, D. C. Sullivan, S. A. Taylor, P. S. Tofts, G. M. Tozer, M. van Herk, S. Walker-Samuel, J. Wason, K. J. Williams, P. Workman, T. E. Yankeelov, K. M. Brindle, L. M. McShane, A. Jackson, and J. C. Waterton. Imaging biomarker roadmap for cancer studies. *Nat Rev Clin Oncol*, 14(3):169–186, 2017. 2

[OJP+12] J. P. O'Connor, A. Jackson, G. J. Parker, C. Roberts, and G. C. Jayson. Dynamic contrast-enhanced MRI in clinical trials of antivascular therapies. *Nat Rev Clin Oncol*, 9(3):167–77, 2012. 7, 16

[OLKT90] S. Ogawa, T. M. Lee, A. R. Kay, and D. W. Tank. Brain magnetic resonance imaging with contrast dependent on blood oxygenation. *Proc Natl Acad Sci U S A*, 87(24):9868–72, 1990. 6

[OS01] S. G. Orel and M. D. Schnall. MR imaging of the breast for the detection, diagnosis, and staging of breast cancer. *Radiology*, 220(1):13–30, 2001. 7

[PB85] C. S. Patlak and R. G. Blasberg. Graphical evaluation of blood-to-brain transfer constants from multiple-time uptake data. Generalizations. *J Cereb Blood Flow Metab*, 5(4):584–90, 1985. 16

[PCB+07] D. Procissi, F. Claus, P. Burgman, J. Koziorowski, J. D. Chapman, S. B. Thakur, C. Matei, C. C. Ling, and J. A. Koutcher. In vivo 19F magnetic resonance spectroscopy and chemical shift imaging of tri-fluoro-nitroimidazole as a potential hypoxia reporter in solid tumors. *Clin Cancer Res*, 13(12):3738–47, 2007. 6

[Pea96] K. Pearson. VII. Mathematical contributions to the theory of evolution.iii. Regression, heredity, and panmixia. *Philosophical Transactions of the Royal Society of London A*, 187:253–318, 1896. 50

[PGM+00] A. R. Padhani, C. J. Gapinski, D. A. Macvicar, G. J. Parker, J. Suckling, P. B. Revell, M. O. Leach, D. P. Dearnaley, and J. E. Husband. Dynamic contrast enhanced MRI of prostate cancer: correlation with morphology and tumour stage, histological grade and PSA. *Clin Radiol*, 55(2):99–109, 2000. 7, 20, 21

[PKH+99] R. E. Port, M. V. Knopp, U. Hoffmann, S. Milker-Zabel, and G. Brix. Multicompartment analysis of gadolinium chelate kinetics: blood-tissue exchange in mammary tumors as monitored by dynamic MR imaging. *J Magn Reson Imaging*, 10(3):233–41, 1999. 17

[PMG+01] A. R. Padhani, A. D. MacVicar, C. J. Gapinski, D. P. Dearnaley, G. J. Parker, J. Suckling, M. O. Leach, and J. E. Husband. Effects of androgen deprivation on prostatic morphology and vascular permeability evaluated with mr imaging. *Radiology*, 218(2):365–74, 2001. 21

[PODG+03] P. Preziosi, A. Orlacchio, G. Di Giambattista, P. Di Renzi, L. Bortolotti, A. Fabiano, E. Cruciani, and P. Pasqualetti. Enhancement patterns of prostate cancer in dynamic MRI. *Eur Radiol*, 13(5):925–30, 2003. 20

[PST+98] G. J. Parker, J. Suckling, S. F. Tanner, A. R. Padhani, J. E. Husband, and M. O. Leach. MRIW: parametric analysis software for contrast-enhanced dynamic MR imaging in cancer. *Radiographics*, 18(2):497–506, 1998. 21

[PT94] P. Paatero and U. Tapper. Positive matrix factorization: A non-negative factor model with optimal utilization of error estimates of data values. *Environmetrics*, 5(2):111–126, 1994. 31

[PWTH+04] A. Preda, P. A. Wielopolski, T. L. Ten Hagen, M. van Vliet, J. F. Veenland, G. Ambagtsheer, S. T. van Tiel, M. W. Vogel, A. M. Eggermont, G. P. Krestin, and C. F. van Dijke. Dynamic contrast-enhanced MRI using macromolecular contrast media for monitoring the response to isolated limb perfusion in experimental soft-tissue sarcomas. *MAGMA*, 17(3-6):296–302, 2004. 69, 88

[RIS+06] C. Roberts, B. Issa, A. Stone, A. Jackson, J. C. Waterton, and G. J. Parker. Comparative study into the robustness of compartmental modeling and model-free analysis in DCE-MRI studies. *J Magn Reson Imaging*, 23(4):554–63, 2006. 20

[RLH+17] C. N. Rumley, M. T. Lee, L. Holloway, R. Rai, M. Min, D. Forstner, A. Fowler, and G. Liney. Multiparametric magnetic resonance imaging in mucosal primary head and neck cancer: a prospective imaging biomarker study. *BMC Cancer*, 17(1):475, 2017. 71

[ROT+15] A. Roniotis, M. E. Oraiopoulou, E. Tzamali, E. Kontopodis, S. Van Cauter, V. Sakkalis, and K. Marias. A Proposed Paradigm Shift in Initializing Cancer Predictive Models with DCE-MRI

Based PK Parameters: A Feasibility Study. *Cancer Inform*, 14(Suppl 4):7–18, 2015. 61

[RRE+03] O. Rouvière, A. Raudrant, R. Ecochard, C. Colin-Pangaud, C. Pasquiou, R. Bouvier, J. M. Maréchal, and D. Lyonnet. Characterization of time-enhancement curves of benign and malignant prostate tissue at dynamic MR imaging. *Eur Radiol*, 13(5):931–42, 2003. 20

[RYB+98] C. Rüegg, A. Yilmaz, G. Bieler, J. Bamat, P. Chaubert, and F. J. Lejeune. Evidence for the involvement of endothelial cell integrin alpha$v$beta3 in the disruption of the tumor vasculature induced by tnf and ifn-gamma. *Nat Med*, 4(4):408–14, 1998. 70

[SAM+16] T. Soldatos, S. Ahlawat, E. Montgomery, M. Chalian, M. A. Jacobs, and L. M. Fayad. Multiparametric Assessment of Treatment Response in High-Grade Soft-Tissue Sarcomas with Anatomic and Functional MR Imaging Sequences. *Radiology*, 278(3):831–40, 2016. 7

[SB11] S. P. Sourbron and D. L. Buckley. On the scope and interpretation of the tofts models for DCE-MRI. *Magn Reson Med*, 66(3):735–45, 2011. 18

[SB12] S. P. Sourbron and D. L. Buckley. Tracer kinetic modelling in MRI: estimating perfusion and capillary permeability. *Phys Med Biol*, 57(2):R1–33, 2012. 18

[Sch12] M. C. Schabel. A unified impulse response model for DCE-MRI. *Magn Reson Med*, 68(5):1632–46, 2012. 19

[SCW+09] K. R. Swanson, G. Chakraborty, C. H. Wang, R. Rockne, H. L. Harpold, M. Muzi, T. C. Adamsen, K. A. Krohn, and A. M. Spence. Complementary but distinct roles for MRI and 18F-fluoromisonidazole PET in the assessment of human glioblastomas. *J Nucl Med*, 50(1):36–44, 2009. 42, 61, 62, 86

[SDB+04] P. Sajda, S. Du, T. R. Brown, R. Stoyanova, D. C. Shungu, X. Mao, and L. C. Parra. Nonnegative matrix factorization for rapid recovery of constituent spectra in magnetic resonance chemical shift imaging of the brain. *IEEE Trans Med Imaging*, 23(12):1453–65, 2004. 26

[SHS+12] R. Stoyanova, K. Huang, K. Sandler, H. Cho, S. Carlin, P. B. Zanzonico, J. A. Koutcher, and E. Ackerstaff. Mapping Tumor Hypoxia In Vivo Using Pattern Recognition of Dynamic Contrast-

enhanced MRI Data. *Transl Oncol*, 5(6):437–47, 2012. 8, 9, 26, 27, 88

[SMG+17] A. Surov, H. J. Meyer, M. Gawlitza, A. K. Höhn, A. Boehm, T. Kahn, and P. Stumpp. Correlations Between DCE MRI and Histopathological Parameters in Head and Neck Squamous Cell Carcinoma. *Transl Oncol*, 10(1):17–21, 2017. 7

[SMP+95] D. M. Sataloff, B. A. Mason, A. J. Prestipino, U. L. Seinige, C. P. Lieber, and Z. Baloch. Pathologic response to induction chemotherapy in locally advanced carcinoma of the breast: a determinant of outcome. *J Am Coll Surg*, 180(3):297–306, 1995. 78

[SSS+02] M. Schindl, S. F. Schoppmann, H. Samonigg, H. Hausmaninger, W. Kwasny, M. Gnant, R. Jakesz, E. Kubista, P. Birner, G. Oberhuber, Austrian Breast Group, and Colorectal Cancer Study. Overexpression of hypoxia-inducible factor 1alpha is associated with an unfavorable prognosis in lymph node-positive breast cancer. *Clin Cancer Res*, 8(6):1831–7, 2002. 3

[SWBA04] B. K. Szabò, M. K. Wiberg, B. Boné, and P. Aspelin. Application of artificial neural networks to the analysis of dynamic MR imaging features of the breast. *Eur Radiol*, 14(7):1217–25, 2004. 25

[TBS95] P. S. Tofts, B. Berkowitz, and M. D. Schnall. Quantitative analysis of dynamic Gd-DTPA enhancement in breast tumors using a permeability model. *Magn Reson Med*, 33(4):564–8, 1995. 18

[TG55] R. H. Thomlinson and L. H. Gray. The histological structure of some human lung cancers and the possible implications for radiotherapy. *Br J Cancer*, 9(4):539–49, 1955. 3

[TGL+99] P. S. Tofts, Brix G., Buckley D L., J.L. Evelhoch, E. Henderson, M.V. Knopp, H.B. Larsson, T.Y. Lee, N.A. Mayr, G.J. Parker, R.E. Port, J. Taylor, and R. M. Weisskoff. Estimating kinetic parameters from dynamic contrastenhanced t1weighted MRI of a diffusable tracer: Standardized quantities and symbols. *Journal of Magnetic Resonance Imaging*, 10(3):223–232, 1999. 16

[TK91] P. S. Tofts and A. G. Kermode. Measurement of the blood-brain barrier permeability and leakage space using dynamic MR imaging. 1. Fundamental concepts. *Magn Reson Med*, 17(2):357–67, 1991. 18

[TLN05] T. Twellmann, O. Lichte, and T. W. Nattkemper. An adaptive tissue characterization network for model-free visualization of dynamic contrast-enhanced magnetic resonance image data. *IEEE Trans Med Imaging*, 24(10):1256–66, 2005. 24

[Tof97] P. S. Tofts. Modeling tracer kinetics in dynamic Gd-DTPA MR imaging. *Journal of Magnetic Resonance Imaging*, 7(1):91–101, 1997. 6, 17, 18, 80

[Tof10] P. S. Tofts. T1-weighted DCE Imaging Concepts: Modelling, Acquisition and Analysis. *Signal*, 500(450):400, 2010. 14

[TSG+04] T. Twellmann, A. Saalbach, O. Gerstung, M. O. Leach, and T. W. Nattkemper. Image fusion for dynamic contrast enhanced magnetic resonance imaging. *Biomed Eng Online*, 3(1):35, 2004. 24

[URC+12] S. Ueda, D. Roblyer, A. Cerussi, A. Durkin, A. Leproux, Y. Santoro, S. Xu, T. D. O'Sullivan, D. Hsiang, R. Mehta, J. Butler, and B. J. Tromberg. Baseline tumor oxygen saturation correlates with a pathologic complete response in breast cancer patients undergoing neoadjuvant chemotherapy. *Cancer Res*, 72(17):4318–28, 2012. 89

[vdWVH+98] H. J. van der Woude, K. L. Verstraete, P. C. Hogendoorn, A. H. Taminiau, J. Hermans, and J. L. Bloem. Musculoskeletal tumors: does fast dynamic contrast-enhanced subtraction MR imaging contribute to the characterization? *Radiology*, 208(3):821–8, 1998. 22

[VHM07] P. Vaupel, M. Höckel, and A. Mayer. Detection and characterization of tumor hypoxia using pO2 histography. *Antioxid Redox Signal*, 9(8):1221–35, 2007. 4

[VKdB+18] M. Venianaki, A. Karantanas, E. de Bree, T. Maris, E. Kontopodis, K. Nikiforaki, O. Salvetti, and K. Marias. Assessment of soft-tissue sarcomas perfusion using data-driven techniques. In *2018 IEEE EMBS International Conference on Biomedical & Health Informatics (BHI)*, pages 353–356, 2018. xix, 53

[VKN+16] M. Venianaki, E. Kontopodis, K. Nikiforaki, E. de Bree, T. Maris, A. Karantanas, O. Salvetti, and K. Marias. Improving hypoxia map estimation by using model-free classification techniques in DCE-MRI images. In *2016 IEEE International Conference on Imaging Systems and Techniques (IST)*, pages 183–188, 2016. xix, 38, 40, 53

[VL00] K. L. Verstraete and P. Lang. Bone and soft tissue tumors: the role of contrast agents for MR imaging. *Eur J Radiol*, 34(3):229–46, 2000. 22

[vRHTB01] C. S. van Rijswijk, P. C. Hogendoorn, A. H. Taminiau, and J. L. Bloem. Synovial sarcoma: dynamic contrast-enhanced MR imaging features. *Skeletal Radiol*, 30(1):25–30, 2001. 22

[VSdB+18] M. Venianaki, O. Salvetti, E. de Bree, T. Maris, A. Karantanas, E. Kontopodis, K. Nikiforaki, and K. Marias. Pattern recognition and pharmacokinetic methods on DCE-MRI data for tumor hypoxia mapping in sarcoma. *Multimedia Tools and Applications*, 77(8):9417–9439, 2018. xix, 53

[WGCL16] J. Wu, G. Gong, Y. Cui, and R. Li. Intratumor partitioning and texture analysis of dynamic contrast-enhanced (DCE)-MRI identifies relevant tumor subregions to predict pathological response of breast cancer to neoadjuvant chemotherapy. *J Magn Reson Imaging*, 44(5):1107–1115, 2016. 25, 89, 90

[WLA+14] J. C. Walsh, A. Lebedev, E. Aten, K. Madsen, L. Marciano, and H. C. Kolb. The clinical importance of assessing tumor hypoxia: relationship of tumor hypoxia to prognosis and therapeutic opportunities. *Antioxid Redox Signal*, 21(10):1516–54, 2014. 5

[WLM84] H. J. Weinmann, M. Laniado, and W. Mützel. Pharmacokinetics of GdDTPA/dimeglumine after intravenous injection into healthy volunteers. *Physiol Chem Phys Med NMR*, 16(2):167–72, 1984. 80

[WSWF91] N. Weidner, J. P. Semple, W. R. Welch, and J. Folkman. Tumor angiogenesis and metastasis–correlation in invasive breast carcinoma. *N Engl J Med*, 324(1):1–8, 1991. 71

[XY] Y. Xu and W. Yin. The block-coordinate update method. Available at `http://www.math.ucla.edu/~wotaoyin/papers/bcu/`. 35

[XY13] Y. Xu and W. Yin. A block coordinate descent method for regularized multiconvex optimization with applications to nonnegative tensor factorization and completion. *SIAM Journal on imaging sciences*, 6(3):1758–1789, 2013. 32, 33

[YCYK12] J. Yuan, S. K. Chow, D. K. Yeung, and A. D. King. A five-colour colour-coded mapping method for DCE-MRI analysis of head and neck tumours. *Clin Radiol*, 67(3):216–23, 2012. 22

[YG09] T. E. Yankeelov and J. C. Gore. Dynamic Contrast Enhanced Magnetic Resonance Imaging in Oncology: Theory, Data Acquisition, Analysis, and Examples. *Curr Med Imaging Rev*, 3(2):91–107, 2009. 15

[YGCHHK02] S. S. Yoo, B. Gil Choi, J. Y. Han, and H. Hee Kim. Independent component analysis for the examination of dynamic contrast-enhanced breast magnetic resonance imaging data: preliminary study. *Invest Radiol*, 37(12):647–54, 2002. 24

[ZEB+09] Y. Zheng, S. Englander, S. Baloch, E. I. Zacharaki, Y. Fan, M. D. Schnall, and D. Shen. STEP: spatiotemporal enhancement pattern for MR-based breast tumor diagnosis. *Med Phys*, 36(7):3192–204, 2009. 25

[ZLG+15] L. Zheng, Y. Li, F. Geng, S. Zheng, R. Yan, Y. Han, Q. Wang, Z. Zhang, and G. Zhang. Using semi-quantitative dynamic contrast-enhanced magnetic resonance imaging parameters to evaluate tumor hypoxia: a preclinical feasibility study in a maxillofacial VX2 rabbit model. *Am J Transl Res*, 7(3):535–47, 2015. 7

[ZZS+00] D. Zagzag, H. Zhong, J. M. Scalzitti, E. Laughner, J. W. Simons, and G. L. Semenza. Expression of hypoxia-inducible factor 1alpha in brain tumors: association with angiogenesis, invasion, and progression. *Cancer*, 88(11):2606–18, 2000. 3